Nonlinear optical spectroscopy at the Liquid- / Solid- interface

Ahmed Abdelmonem

2008

INAUGURAL – DISSERTATION

zur

Erlangung der Doktorwürde

der

Naturwissenschaftlich – Mathematischen Gesamtfakultät

der

Ruprecht – Karls – Universität

Heidelberg

Vorgelegt von

Ahmed Abdelmonem[*] B.Sc., M.Sc.

aus: Ägypten

Tag der mündlichen Prüfung:

[*] Optical spectroscopy
Institute of Nuclear wastes Disposal (INE) - Karlsruhe research Center- Germany (FZK)
@ : ahmed.abdelmonem@ine.fzk.de , www: amamonem.de

Thema

Nichtlinear optische Spektroskopie an der Flüssig- /Fest- Grenzfläche

Ahmed Abdelmonem

2008

Gutachter:

Priv. Doz. Dr. rer. nat. Michael Himmelhaus

Priv. Doz. Dr. rer. nat. Hans-Robert Volpp

بِسْمِ اللّهِ الرَّحْمَنِ الرَّحِيم

In the name of Allah, Most Gracious, Most Merciful

Im Namen Gottes, des Gnädigen, des Barmherzigen

قال تعالى.

اقْرَأْ باسْمِ رَبِّكَ الَّذِي خَلَقَ (١) خَلَقَ الإِنْسَانَ مِنْ عَلَقٍ (٢) اقْرَأْ وَرَبُّكَ الأَكْرَمُ (٣) الَّذِي عَلَّمَ بِالْقَلَمِ (٤) عَلَّمَ الإِنْسَانَ مَا لَمْ يَعْلَمْ (٥)

God said:

Proclaim! (or read!) in the name of thy Lord and Cherisher, Who created- (1) Created man, out of a (mere) clot of congealed blood: (2) Proclaim! And thy Lord is Most Bountiful,- (3) He Who taught (the use of) the pen,- (4) Taught man that which he knew not (5)

Gott hat gesagt:

Lies im Namen deines Herrn, Der alles erschaffen hat! (1) Er erschuf den Menschen aus einem Embryo, (2) Lies! Dein Herr ist der Erhabenste,(3) Der das Schreiben mit dem Schreibrohr lehrte, (4) Er lehrte den Menschen, was er nicht wüsste (5)

صدق الله العظيم

ABSTRACT

Sorption-desorption of fatty organic compounds on clay minerals influence the migration process of these compounds in their soil environment, particularly in aquatic medium. In order to understand part of the interaction between such organic compounds and clay minerals, a simple system was considered. Crystalline sapphire was taken as a model for natural clay minerals, and methanol, ethanol, 1-Propanol, 1-butanol, chloroform and propionic acid were chosen as simple but representative model molecules for the more complex organic compounds found in soil. Linear and nonlinear techniques were combined to study the mechanisms of interaction. Sum Frequency Generation (SFG) as a nonlinear interface selective technique was used to probe the adsorption-desorption mechanism at the interfaces for the different systems under study by tracking changes in their average orientation and density at and in vicinity of the surface. Reflectivity in total internal reflection geometry (TIR) was conducted to determine the optical constants of the interface with such high precision that the analysis of the SFG data became feasible, in particular with respect to the determination of molecular orientations. Contact angle and XPS technique were used as inspection tools for the cleanness of the crystal surface. Particular accuracy was required in this work to allow tracking of even subtle changes in the interactions. To achieve such high accuracy, the commercial SFG system applied was further developed and improved to a level of high stability and data reproducibility.

The study was carried out by observing the molecules under study through their nonlinear optical vibrational fingerprints in the spectral range from 2500 to 4000 cm^{-1}, which covers the CH and OH vibrations of the selected media. It was found that the results are highly dependent on the nature of the sapphire surface. In the literature, it has been speculated that a strongly bound water layer exists on the sapphire surface prepared and cleaned with a given procedure. All the reactions found and observed in the present study could be explained in terms of hydrogen bonding competition.

Meanwhile and marginal off the presented study, two novel spectroscopic techniques were developed. It is assumed that these techniques will be useful in future work on the adsorption kinetics of organic molecules and compounds of different kind. The first technique was the development of a real time spatially and temporally resolved sum frequency

generation system based on a broadband femtosecond laser source. The second technique was a combination of in-situ Second Harmonic Generation (SHG) and Ellipsometry to probe surface coverage and thickness of adsorbed layers of the Self-assembled organic Monolayers (SAMs) simultaneously and in real time.

ABSTRACT

Sorptions- und Desorptionsprozesse von Kleinen organischen Säuren und anderen Abbauprodukten aus der Zerfallskette biologischer Substanzen im Erdreich („Huminstoffe“) auf Bodenmineralien spielen eine besondere Rolle in Bezug auf die Migration dieser Substanzen, insbesondere in aquatischer Phase. Um derartige Prozesse besser verstehen zu können, wurde in der vorliegenden Arbeit ein einfaches Modellsystem untersucht. Kristalliner Saphir diente dabei als Modelloberfläche zur Simulation der Mineraloberfläche, während einfache organische Alkohole, Lösungsmittel und Säuren, wie Methanol, Ethanol, 1-Propanol, 1-Butanol, Chloroform, und Propionsäure, als Modellsubstanzen für Huminstoffkomponenten gewählt wurden.

Dieses Modellsystem wurde mit Hilfe linearer und nichtlinearer optischer Vibrationsspektroskopien untersucht. IR-vis Summenfrequenzerzeugung als nichtlinear optische grenzflächenspezifische Methode wurde dazu benutzt, die Adsorptions- und Desorptionsprozesse der verschiedenen Modellsubstanzen auf der Saphiroberfläche im Hinblick auf die mittlere Orientierung und Ordnung der Moleküle in unmittelbarer Nähe der Oberfläche zu untersuchen. Linear optische Reflektionsmessungen wurden in Totalreflexionsgeometrie (TIR, von engl. „Total Internal Reflection“) durchgeführt, um die optischen Konstanten der verschiedenen Substanzen im relevanten spektralen Bereich und unter der bei den nichtlinear optischen Messungen benutzten Meßanordnung zu bestimmen. Kontaktwinkelmessungen und Röntgenphotoelektronenspektroskopie (XPS, von engl. „X-ray photoelectron spectroscopy“) wurden zur Charakterisierung der Kristalloberflächen eingesetzt, insbesondere im Hinblick auf ihre Reinheit. Besondere Sorgfalt beim Betrieb des Lasersystems war nötig, um selbst feine Unterschiede und Änderungen im Linienprofil der SFG-Spektren zu verfolgen. Um die dazu erforderliche Stabilität des Lasersystems sicherzustellen, wurde das System technisch weiterentwickelt und bezüglich Betriebszuverlässigkeit und Reproduzierbarkeit seiner Leistungsparameter verbessert.

Die Untersuchung der Flüssig/Saphirgrenzfläche erfolgte über das Studium der nichtlinear-optischen Charakteristik der verschiedenen Systeme in einem spektralen Bereich von 2500 bis 4000 cm^{-1}, welcher die Regionen der CH und OH Streckschwingungen abdeckt. Bei den Messungen stellte sich heraus, daß die Ergebnisse stark von der Natur der

eingesetzten Saphiroberfläche abhängen, und zwar nicht nur bezüglich ihres Schnittes (001 und 110 in der vorliegenden Arbeit), sondern insbesondere auch in Bezug auf ihre Oberflächenbehandlung. In der Literatur wurde bereits darüber spekuliert, ob sich auf der Saphiroberfläche in Abhängigkeit von ihrer Präparation eine festgebundene Wasserschicht ausbilden könnte, die nicht einfach entfernt werden kann. Alle in der vorliegenden Arbeit durchgeführten Untersuchungen sind in Einklang mit dieser Sichtweise und lassen sich durch einen Wettbewerb zwischen Wasseradsorption und der Adsorption der jeweiligen organischen Substanz erklären.

Neben dieser Hauptthematik wurden in der vorliegenden Arbeit auch zwei neuartige spektroskopische Techniken zur Untersuchung dünner oberflächenadsorbierter organischer Filme entwickelt, die möglicherweise für zukünftige Arbeiten auf dem Gebiet der Huminstoffmigration oder verwandter Themen von Bedeutung sein könnten. Bei diesen beiden Techniken, die am Ende der Arbeit kurz vorgestellt werden, handelt es sich zum einen um eine Form der zeitaufgelösten Breitbandsummenfrequenzerzeugung unter Zuhilfenahme eines Femtosekundenlasersystems sowie um eine Kombination aus spektraler Ellipsometrie und optischer Frequenzverdopplung, die in situ und in Echtzeit die simultane Messung von Oberflächenbedeckung und adsorbierter Schichtdicke erlaubt.

Contents

CHAPTER 1

THEORY

1. Theoretical Background

1. Theoretical Background

1.1 Introduction to Sum Frequency Generation

Sum Frequency Generation (SFG), as well as Second Harmonic Generation (SHG), is a highly sensitive optical probe of surfaces and interfaces where light is generated at a frequency which is the sum of the frequencies of two incident optical fields (of the incident beams). The signal is generated when the incident beams are spatially and temporally overlapped at a point of broken inversion-symmetry. Geometrically, in the most common cases, the point of broken inversion-symmetry is at an interface between two different isotropic media. The direction of the generated beam is determined by the conservation of the photons' momentum ("momentum equation"), which will be discussed later in this chapter. The SFG signal can be measured in normal reflection and/or transmission, total internal reflection, counterpropagating and surface-plasmon-enhanced-SFG geometries [1] depending on the conditions of the experiment. Figure 1-1 shows reflection geometry where the incident and generated beams are travelling in the same medium. Some times the reflection geometry is taken in the configuration of Total Internal Reflection (TIR) where the incident beams reach the interface from the medium of the higher refractive index and at incident angles which are higher than the critical angle (This is the geometry used in this work). Usually, the SFG experiments are carried out with definite polarization combinations of incident and generated beams. Such experiments are rich of information, particularly about concentrations and orientations of the species which contribute to the SFG signal (section 1.5.3). The terminology of the polarization combinations are given in the order of decreasing photon energy (e.g. if the SFG light is generated from visible and IR lights, then SSP means S-polarized SFG, S-polarized visible and P-polarized IR respectively.

Nonlinear optics was born with the discovery of the ruby laser. Franken et al. [2] demonstrated the first optical SHG and SFG in quartz crystals. This second order nonlinear optical process occurs at a position where the inversion symmetry is broken, at interfaces between isotropic media or within a non-centrosymmetric medium. Surface SFG is particularly interesting, because surface-sensitive vibrational spectroscopic methods are so rare. The SFG signal is strongly enhanced when one of the incident frequencies and/or the sum frequency is in resonance with real quantum levels. For example, if the incident infrared photon resonantly excites a vibrational transition following by an up-conversion to a virtual electronic state by an incident visible light, then a light at the sum frequency is generated.

This process is called “IR-visible SFG”. Since the first experimental demonstration of surface SFG by Shen et al. [3] (1986), it is believed that the vibrational modes must be both infrared and Raman active to allow SFG generation. So far, these selection rules [4] are consistent with numerous experimental results. In more advanced sight, if the IR and the sum-frequency are resonant with vibrational and electronic transitions respectively then this is a slightly different case. Obviously, the selection rule for the IR activity is still valid while one should think about the validity of Raman activity. Instead, in this case, the two –photon absorption (TPA) polarizability tensor is the important parameter, see Figure 1-2.

Symmetry arguments rule that SFG is forbidden in a medium with an inversion centre but allowed at a surface or interface where the inversion symmetry is necessarily broken. Therefore, SFG (as well as SHG) at the interface between to isotropic media is a highly interface-specific technique, and in recent years, has been developed into a powerful and versatile surface probe. SHG and SFG have been used to probe the aqueous/air, aqueous/solid and solid/air interfaces [5-18]. The theoretical basis for these techniques has been set out by Bloembergen and Pershan in the 1960s [19]. SHG results from the combination of two visible or near-infrared photons and accesses the electronic states of the surface molecules. Shen et al. [9] are considered pioneers in applying SHG to study a liquid interface.

The first SFG experiments which demonstrated the applicability of the technique were reported in 1987-88. Optimization of the surface concentration and limitation of subsurface penetration by examining organic molecules on solid substrates such as quartz [14,15] and semiconductors [16] have been performed. Later, Shen and co-workers [17] studied the neat methanol liquid interface and in 1993 they reported the first SFG spectrum of the pure water/air interface [18]. Spectroscopic studies of the structure of the water surface as it is affected by salts, acids, and ammonia have been presented by Allen et al. [20].

The overall SFG intensity depends on many parameters; 1) the incident beams (intensity, spatial overlap, temporal overlap and polarization combinations), 2) the optical properties of the media at the interface manifested in the Fresnel factors and 3) the concentrations and orientations of the molecules and the response of the existing dipoles, at the interface. Each of these parameters has its characteristic effect on the SFG efficiency as will be explained in detail in the following sections.

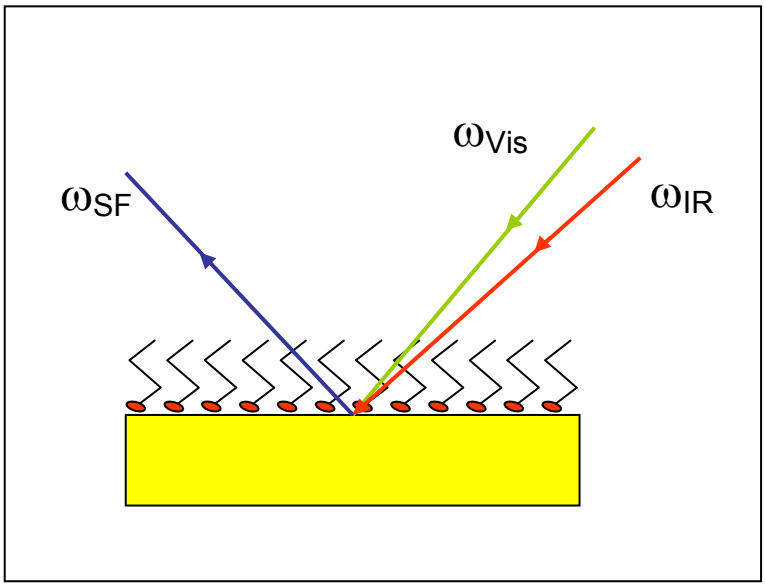

Figure 1-1 Simple scheme of SFG generation in co-propagating geometry

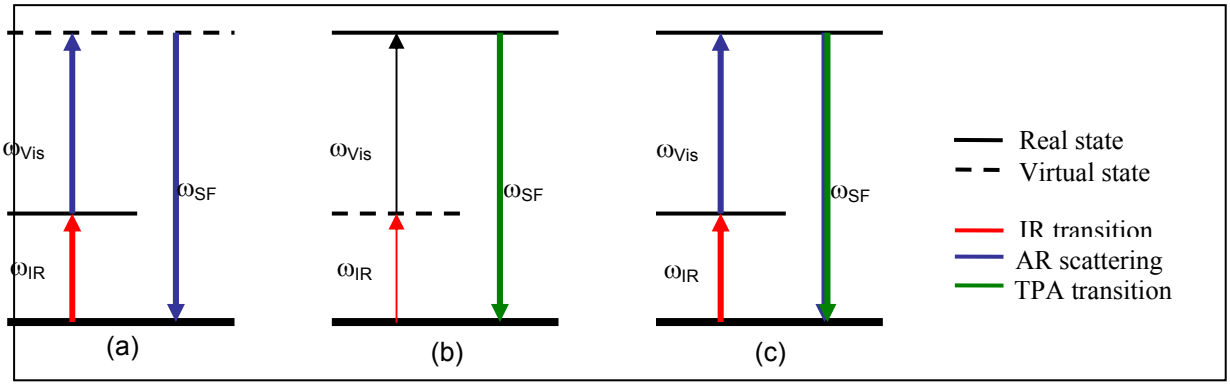

Figure 1-2 Three cases of SFG in resonance; (a) resonance with the incident IR excites the system to a real vibrational state followed by an anti-Stokes Raman (AR) process (excitation to a virtual state followed by Raman transition to the ground state), (b) resonance at the SFG between the ground state and a real electronic state which correspond to a two-photon absorption (TPA) process, (c) double resonance at both IR and SFG which is a combination of (a) & (b)

1.2 Basis for SFG and Nonlinear Optical Activity

When a light beam hits a surface, a polarization is induced by the exerted force on the valence electrons. Primarily, the medium responds linearly to the incident field by absorption, Rayleigh or Raman scattering. If the incident field is sufficiently intense, the medium responds nonlinearly and this response is described by the hyperpolarizability of the medium [21]. In this case, the incident electric fields produce induced electric fields *E1* and *E2* inside the medium, which in turn create a total, i.e. linear and nonlinear, polarization, *P*;

$$P = \varepsilon_0 \left[\chi(\omega_1, \omega_2).E(\omega_1, \omega_2) + \chi^s(\omega_1, \omega_2) : E(\omega_1, \omega_2)E(\omega_1, \omega_2) \right] \tag{1.1}$$

where, χ is the linear polarizability and χ^s is the second order nonlinear hyperpolarizability. The term χ^s is a tensor and describes the generation of SHG, SFG, and Difference Frequency Generation (DFG).

If the generating electric fields inside of the medium can be described by plane waves, then:

$$E(\omega, t) = \left(A(\omega_1)e^{i\omega_1 t} + A^*(\omega_1)e^{-i\omega_1 t} \right) + \left(A(\omega_2)e^{i\omega_2 t} + A^*(\omega_2)e^{-i\omega_2 t} \right) \tag{1.2}$$

where A and A^* are the real and complex amplitudes of the incident waves respectively. In this case, the induced second order nonlinear polarization P^s will have the following terms:

$$P^s(\omega, t) = \varepsilon_0 \chi^s(\omega_1, \omega_2) \begin{bmatrix} 2\left(A^2(\omega_1) + A^2(\omega_2)\right) \\ + A^2(\omega_1)e^{i2\omega 1t} + cc_1 \\ + A^2(\omega_2)e^{i2\omega_2 t} + cc_2 \\ + 2A(\omega_1)A^*(\omega_2)e^{i(\omega_1+\omega_2)t} + cc_{1+2} \\ + 2A(\omega_1)A^*(\omega_2)e^{i(\omega_1-\omega_2)t} + cc_{1-2} \end{bmatrix} \tag{1.3}$$

which are respectively assigned to:

- Optical rectification due to static polarization ($\omega = 0$)

- Second harmonic generation of frequency ω_1

- Second harmonic generation of frequency ω_2

- Sum frequency generation of frequency $\omega_1 + \omega_2$

- Difference frequency generation frequency $\omega_1 - \omega_2$

In this study we are interested only in the sum frequency process, which can be measured selectively. In addition, Kleinman Symmetry [22] will be assumed where the spectral dispersion of the tensor elements of χ^s is ignored. Under this condition, the indices of the susceptibility tensors χ_{ijk} can be permuted freely regardless of permuting the frequencies. Using the matrix notation, one can write the amplitude of the induced polarization at the sum frequency as follows:

$$\left(P^s(\omega_1+\omega_2)\right) = 2\varepsilon_0\left(\chi^s\right):\left(A(\omega_1)A^*(\omega_2)+cc_{1+2}\right), \tag{1.4}$$

where

$$\left(\chi^s\right) = \begin{pmatrix} \sum_{jk}\chi_{xjk} \\ \sum_{ik}\chi_{yik} \\ \sum_{ij}\chi_{zij} \end{pmatrix} \tag{1.5}$$

Equations (1.1)-(1.5) show that the second order response relies on:

1. The relation between the incident electric fields and those induced inside of the medium, hence the induced polarization and the electric field of the generated signal.
2. The macroscopic hyperpolarizability $\chi_{IJK}{}^s$ tensor and thus the molecular hyperpolarizability $\beta_{\alpha\beta\gamma}{}^s$

1.3 Electric Fields Inside the Medium

In order to extract microscopic information from experimental data and recognize the surface nonlinear susceptibility, a suitable model is required. The first approach was made by *Bloembergen and Pershan* [19], when they considered a slab of material, in the limit of zero thickness, as a model for the surface and derived on this basis the nonlinear optical parameters of the interface. Recently, two other phenomenological models for treating SHG at surface have been presented. The first model was presented by *Mizrahi and Sipe* [23,24]. They used a dipole sheet at the interface as a model of surface second harmonic source and a Green function approach for s and p components of the electromagnetic field. The electric field of the incident light was taken within the substrate at the interface. The nonlinear signal is generated in the nonlinear layer at the interface and then diffracted/refracted by the interface. The second model was presented by *Shen* [5]. He assumed also a sheet of dipole moments but this time it is a third layer which lies between the substrate and the second medium and has an unknown dielectric constant ε' (unknown refractive index n'). The electric field of the incident light is calculated within the nonlinear layer, (multiple reflections within the layer are neglected), and the nonlinear signal is considered to be generated in the nonlinear layer and then emitted to the substrate and the second medium.

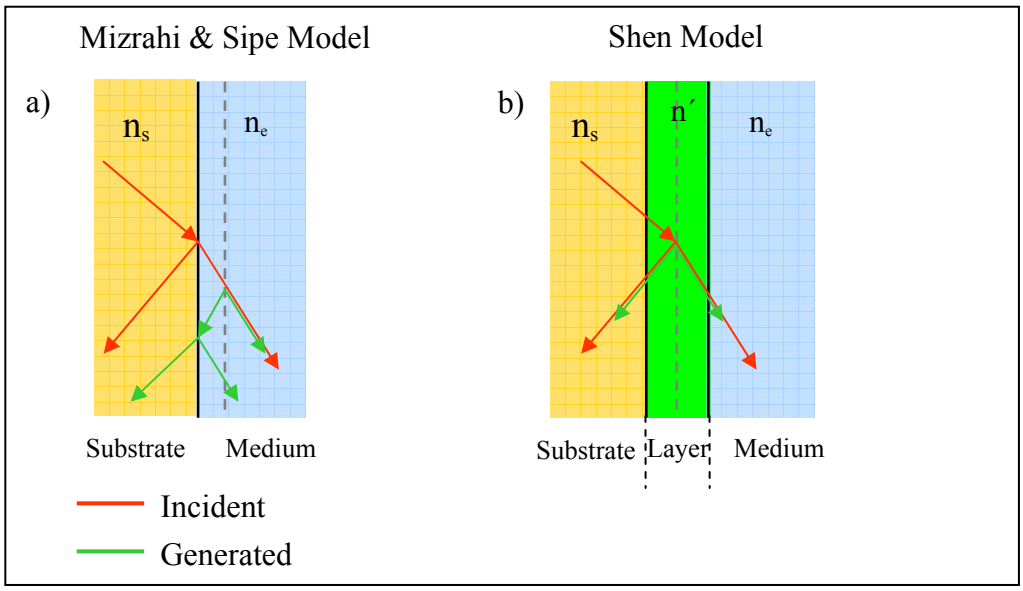

Figure 1-3 An illustration of the difference between the a) Mizrahi & Sipe model: incident electric field is calculated at the substrate side from the interface and the nonlinear signal is generated at the nonlinear layer and the diffracted/refracted by the interface, and b) the Shen model: incident electric field is calculated within the nonlinear layer and the nonlinear signal is generated at the nonlinear layer and then emitted to the substrate and second medium. The dashed line corresponds to the zero thickness polarization sheet

1. Theoretical Background

In the presented work, the model from Mizrahi and Sipe is considered after making some modifications to account for SFG instead of SHG and to fit the used experimental geometry. Also the SI-unit system is used instead of the CGS-unit system [See Appendix-1]. Therefore we start with the same hypothesis and end with a new model. The nonlinear surface layer is considered as a polarization sheet which lies in the x-y-plane given by;

$$P(r,t) = \mathcal{P}\,\delta(z)e^{ik.R}e^{-i\omega t} + c.c.$$

(1.6)

where R=(x,y), $\delta(z)$ is the Dirac-delta-function representing a polarization sheet in the limit of zero thickness .

We are interested in the electromagnetic field reemitted by the oscillating polarization sheet as given in equation (1.6). The solution of Maxwell equations, with a source polarization given by equation (1.6) at $z \neq 0$, for the generated fields was found [24] to be:

$$\begin{aligned} E(r,t) &= E(r)e^{-i\omega t} + c.c. \\ E(r,t) &= \left[E_{+}(r)\theta(z) + E_{-}(r)\theta(-z)\right]e^{-i\omega t} + c.c. \\ E(r,t) &= \left[\left(E_{s+}\hat{s} + E_{p+}\hat{p}_{+}\right)e^{ik_{+}.r}\theta(z) + \left(E_{s-}\hat{s} + E_{p-}\hat{p}_{-}\right)e^{ik_{-}.r}\theta(-z)\right]e^{-i\omega t} + c.c. \end{aligned}$$

(1.7)

where,

$$E_{\pm}(r) = \left(E_{s\pm}\hat{s} + E_{p\pm}\hat{p}_{\pm}\right)e^{ik_{\pm}.r}$$

(1.8)

and

$$\begin{aligned} E_{s\pm} &= \frac{i\omega^2}{2k_z c^2}\hat{s}.\mathcal{P} \\ E_{p\pm} &= \frac{i\omega^2}{2k_z c^2}\hat{p}_{\pm}.\mathcal{P} \end{aligned}$$

(1.9)

The fields $E_{+}(r)$ and $E_{-}(r)$ correspond to the upward and downward propagating (evanescent) waves respectively, Figure 1-4. The E_s and E_p denote the s-polarization and the p-polarization components of the fields. $k_{\pm}$ are the wave vectors of the upward (+) and the downward (-) waves. $\theta(z)$ is a condition function which has a value of unity only for $z > 0$

and zero elsewhere. $\hat{s}$ and $\hat{p}_{\pm}$ are the s- and p- polarization unit vectors respectively. The (+) and (-) signs denote always the upward and downward propagation.

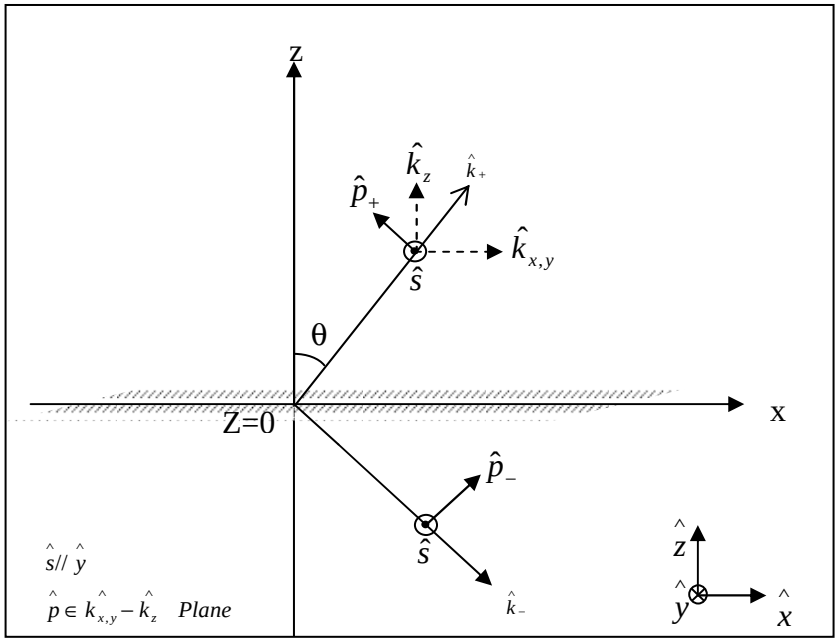

Figure 1-4 Upward and downward propagating (evanescent) waves at the interface.

From the geometry in Figure 1-4, the following relations can be written down:

$$k_{\pm} = k_{x,y} \pm k_z \hat{z} \Rightarrow$$
$$|k_{\pm}| = \left|\frac{n\omega}{c}\right| = \sqrt{k_{x,y}^2 + k_z^2} \tag{1.10}$$

$$\hat{s} = \hat{k}_{x,y} \times \hat{z}$$
$$\hat{P}_{\pm} = \frac{(k_{x,y}\hat{z} \mp k_z \hat{k}_{x,y})}{n\omega} c \text{ ,} \tag{1.11}$$

where $k_{x,y}$ is the component of the wave vector in the x-y-plane and k_z is the z-component of the wave vector.

In this model, the induced nonlinear polarization sheet is assumed at the position $z = 0^-$ from the substrate surface, see Figure 1-4 and Figure 1-5, and the generated nonlinear signal is emitted from this point. The induced polarization is given by:

$$P^{\omega_{SF}}(r,t) = P^{\omega_{SF}}(R)\delta(z-0^{-})e^{-i\omega_{SF}t} + c.c.$$

(1.12)

where,

$$P^{\omega_{SF}}(R) = \varepsilon_o \chi^s : E^{\omega_{Vis}}(R, z=0^{+})E^{\omega_{IR}}(R, z=0^{+})$$

(1.13)

$$E^{\omega_i}(r,t) = E^{\omega_i}(r)e^{-i\omega_i t} + c.c.$$
$$E^{\omega_i}(r) = E^{\omega_i}(z)e^{-ik_{x,y}.R}$$

(1.14)

The linear optical properties of the polarization sheet are neglected here since the response is mainly nonlinear; further, a plane wave was assumed (Gaussian beam will be considered later). $E^{\omega_i}(R, z=0^{+})$ is the fundamental electric field of frequency ω_i at the point $z=0^{+}$. To obtain the generating fields inside of the medium, we consider the geometry shown in Figure 1-5. Using the x-z-plane as an incident plane for simplicity, the fundamental fields (crossing the point $z=0^{+}$) on substrate side can be written as follows, from equation(1.8);

$$E_{n_s}^{\omega_i}\left(x, z=0^{+}\right) = \begin{pmatrix}\text{Light passes through the}\\ \text{air/substrate interface}\\ \text{directly to z = } 0^{+}\end{pmatrix} + \begin{pmatrix}\text{Light passed through the air/substrate}\\ \text{interface to substrate/medium (z = 0)}\\ \text{and then reflected to z = } 0^{+}\end{pmatrix}$$

$$= \left(E_{-}^{s}\hat{s} + E_{-}^{p}\hat{p}_{-}^{n_s}\right)e^{i(k_x x - k_z z)} + \left(E_{+}^{s}\hat{s} + E_{+}^{p}\hat{p}_{+}^{n_s}\right)e^{i(k_x x - k_z z)}$$
$$= \left[\left(E_{in}^{s}t_{a\to s}^{s}\hat{s} + E_{in}^{p}t_{a\to s}^{p}\hat{p}_{-}^{n_s}\right) + \left(E_{in}^{s}t_{a\to s}^{s}r_{s\to m}^{s}\hat{s} + E_{in}^{p}t_{a\to s}^{p}r_{s\to m}^{p}\hat{p}_{+}^{n_s}\right)\right]e^{ik_x x}$$

(1.15)

Multiplying equation (1.15) by $\frac{|E_{in}|}{|E_{in}|}$, where $|E_{in}|^2 = |E_{in}^{s}|^2 + |E_{in}^{p}|^2$, this gives;

$$
\begin{aligned}
E_{n_s}^{\omega_i}(x, z=0^+) &= \left[\left(\frac{E_{in}^s}{|E_{in}|} t_{a\to s}^s \hat{s} + \frac{E_{in}^p}{|E_{in}|} t_{a\to s}^p \hat{p}_-^{n_s}\right) + \left(\frac{E_{in}^s}{|E_{in}|} t_{a\to s}^s r_{s\to m}^s \hat{s} + \frac{E_{in}^p}{|E_{in}|} t_{a\to s}^p r_{s\to m}^p \hat{p}_+^{n_s}\right)\right] |E_{in}| e^{ik_x x} \\
&= \left[\left(\hat{s} t_{a\to s}^s \hat{s} + \hat{p}_-^{n_a} t_{a\to s}^p \hat{p}_-^{n_s}\right) \bullet \left(\frac{E_{in}^s}{|E_{in}|} \hat{s} + \frac{E_{in}^p}{|E_{in}|} \hat{p}_-^{n_a}\right) + \left(\hat{s} t_{a\to s}^s r_{s\to m}^s \hat{s} + \hat{p}_-^{n_a} t_{a\to s}^p r_{s\to m}^p \hat{p}_+^{n_s}\right) \bullet \left(\frac{E_{in}^s}{|E_{in}|} \hat{s} + \frac{E_{in}^p}{|E_{in}|} \hat{p}_-^{n_a}\right)\right] |E_{in}| e^{ik_x x} \\
&= \left[\left(\hat{s} t_{a\to s}^s \hat{s} + \hat{p}_-^{n_a} t_{a\to s}^p \hat{p}_-^{n_s}\right) + \left(\hat{s} t_{a\to s}^s r_{s\to m}^s \hat{s} + \hat{p}_-^{n_a} t_{a\to s}^p r_{s\to m}^p \hat{p}_+^{n_s}\right)\right] \bullet \left(\frac{E_{in}^s}{|E_{in}|} \hat{s} + \frac{E_{in}^p}{|E_{in}|} \hat{p}_-^{n_a}\right) |E_{in}| e^{ik_x x} \\
&= \left[\hat{s}\left(1 + r_{s\to m}^s\right) t_{a\to s}^s \hat{s} + \left(\hat{p}_-^{n_s} + r_{s\to m}^p \hat{p}_+^{n_s}\right) t_{a\to s}^p \hat{p}_-^{n_a}\right] \bullet e^{in} |E_{in}| e^{ik_x x} \\
&= \mathbf{e}^{\omega_i} |E_{in}| e^{ik_x x}
\end{aligned}
\tag{1.16}
$$

where,

$$
\mathbf{e}^{in} = \left(\frac{E_{in}^s}{|E_{in}|} \hat{s} + \frac{E_{in}^p}{|E_{in}|} \hat{p}_-^{n_a}\right) \tag{1.17}
$$

represents the incident field vector (from air) and

$$
\mathbf{e}^{\omega_i} = \left[\hat{s}\left(1 + r_{s\to m}^s\right) t_{a\to s}^s \hat{s} + \left(\hat{p}_-^{n_s} + r_{s\to m}^p \hat{p}_+^{n_s}\right) t_{a\to s}^p \hat{p}_-^{n_a}\right] \bullet \mathbf{e}^{in} \tag{1.18}
$$

represents the geometry coefficients, “nonlinear Fresnel Factors”, which are based on the linear Fresnel Factors and influence the measured nonlinear signal. The dot product analyzes the field into its s- and p- components. Equation (1.18) is valid for both incident fields, ($\omega_i = \omega_{Vis}$ *or* ω_{IR}).

The induced polarization at z=0-, equation (1.13), can be written now as;

$$
\begin{aligned}
P^{\omega_{SF}}(r) &= \varepsilon_o \chi^s : \mathbf{e}^{\omega_{Vis}} \mathbf{e}^{\omega_{IR}} \left|E_{in}^{Vis}\right| \left|E_{in}^{IR}\right| e^{i(k_{Vis}+k_{IR})x} \delta(z - 0^-) \\
&= \mathcal{P}\, e^{ik_{SF}x} \delta(z - 0^-)
\end{aligned}
\tag{1.19}
$$

where, $\mathcal{P}$ is the amplitude of the induced polarization,

$$
\mathcal{P} = \varepsilon_o \chi^s : \mathbf{e}^{\omega_{Vis}} \mathbf{e}^{\omega_{IR}} \left|E_{in}^{Vis}\right| \left|E_{in}^{IR}\right| \tag{1.20}
$$

This induced polarization is the source of the nonlinear signal. The generated field is given by equation (1.14) where,

$$E^{\omega_{SF}}(r) = \begin{pmatrix} \text{The generated signal at z = 0}^{-} \text{ then transmited throught the} \\ \text{medium/substrate interface, traveling inside the substrate} \\ \text{and finally transmited through the substrate/air interface} \end{pmatrix}$$
$$= \left(E_{+}^{s}\hat{s}.\hat{s}t_{m\to s}^{s}\hat{s}.\hat{s}t_{s\to a}^{s}\hat{s} + E_{+}^{p}\hat{p}_{+}^{n_m}.\hat{p}_{+}^{n_m}t_{m\to s}^{p}\hat{p}_{+}^{n_s}.\hat{p}_{+}^{n_s}t_{s\to a}^{p}\hat{p}_{+}^{n_a}\right)e^{i(k_{SF,x}x+k_{SF,z}z)}$$
$$= \left(E_{+}^{s}t_{m\to s}^{s}t_{s\to a}^{s}\hat{s} + E_{+}^{p}t_{s\to a}^{p}t_{m\to s}^{p}\hat{p}_{+}^{n_a}\right)e^{i(k_{SF,x}x+k_{SF,z}z)}$$

(1.21)

Using equation (1.9) with equation (1.21) gives;

$$E^{\omega_{SF}}(r) = \frac{i\omega_{SF}^{2}}{2k_{SF,z}c^{2}}\left(\hat{s}t_{ms}^{s}t_{sa}^{s}\hat{s} + \hat{p}_{+}^{n_m}t_{ms}^{p}t_{sa}^{p}\hat{p}_{+}^{n_a}\right).\mathcal{P}\, e^{i(k_{SF,x}x+k_{SF,z}z)}$$

(1.22)

The polarization components of the detected signal they can be denoted by

$$\mathbf{e}^{out} = \left(\frac{E_{out}^{s}}{|E_{out}|}\hat{s} + \frac{E_{out}^{p}}{|E_{out}|}\hat{p}_{+}^{n_a}\right),$$

where

$$|E_{out}|^{2} = |E_{out}^{s}|^{2} + |E_{out}^{p}|^{2},$$

and then the amplitude of $E^{\omega_{SF}}(r)$ can be rewritten as follows:

$$E^{\omega_{SF}} = \frac{i\omega_{SF}^{2}}{2k_{SF,z}c^{2}}\left(\hat{s}t_{m\to s}^{s}t_{s\to a}^{s}\hat{s} + \hat{p}_{+}^{n_m}t_{m\to s}^{p}t_{s\to a}^{p}\hat{p}_{+}^{n_a}\right)\bullet\mathbf{e}^{out}\bullet\mathcal{P}$$
$$= \frac{i\omega_{SF}^{2}}{2k_{SF,z}c^{2}}\mathbf{e}^{\omega_{SF}}\bullet\mathcal{P}$$

(1.23)

where,

$$\mathbf{e}^{\omega_{SF}} = \left(\hat{s}t_{m\to s}^{s}t_{s\to a}^{s}\hat{s} + \hat{p}_{+}^{n_m}t_{m\to s}^{p}t_{s\to a}^{p}\hat{p}_{+}^{n_a}\right)\bullet\mathbf{e}^{out}$$

(1.24)

Substituting from equation (1.19) in (1.23) gives;

$$E^{\omega_{SF}} = \frac{i\omega_{SF}^{2}}{2k_{SF,z}c^{2}}\left|\mathbf{e}^{\omega_{SF}}\bullet\chi^{s}:\mathbf{e}^{\omega_{Vis}}\bullet\mathbf{e}^{\omega_{IR}}\right|\left|E_{in}^{Vis}\right|\left|E_{in}^{IR}\right|$$

(1.25)

(1.25)

Recalling the assumption that the SFG signal is generated at the medium side of the interface and using the geometry of the generated SFG light, see Figure 1-5, one can find that:

$$\sec g' = \frac{n_m(\omega_{SF})\omega_{SF}}{k_{SF,z}c}$$

then equation (1.25) can be written as;

$$E^{\omega_{SF}} = \frac{i\omega_{SF}}{2c}\frac{\sec(g')}{n_m(\omega_{SF})}\left|\mathbf{e}^{\omega_{SF}} \bullet \chi^s : \mathbf{e}^{\omega_{Vis}} \bullet \mathbf{e}^{\omega_{IR}}\right|\left|E_{in}^{Vis}\right|\left|E_{in}^{IR}\right|$$

(1.26)

Equation (1.26) is the field equation which will be used for the evaluation of the experimental data. The corresponding intensity equation can be driven from the relation $I = (n\varepsilon_o c/2)\left|E^{SF}\right|^2$, [25]. It is worth to mention that in the model of Mizrahi and Sipe the created light is considered to be a SHG signal created by only one beam of intensity I^{ω}. If the signal is generated by two beams, each has a field strength of E^{ω_i} $(i = 1,2)$, then the intensity will be 4 times greater than that generated by one beam. This is because the case of two beams simulates one beam of field strength $2E^{\omega}$ and hence it's square value will be $4\left|E^{\omega}\right|^2$ in the intensity equation. This should be the case for two incident beams of different frequencies, the resultant SFG intensity can be written as follow:

$$I^{\omega_{SF}} = \frac{2\omega_{SF}^2}{n_a c^3 \varepsilon_o}\frac{\sec^2(g')}{n_m^2(\omega_{SF})}\left|d_{eff}\right|^2 I^{Vis} I^{IR}$$

(1.27)

Where,

$$\left|d_{eff}\right| = \left|\mathbf{e}^{\omega_{SF}} \bullet \chi^s : \mathbf{e}^{\omega_{Vis}} \bullet \mathbf{e}^{\omega_{IR}}\right|$$

(1.28)

is the effective hyper-susceptibility tensor.

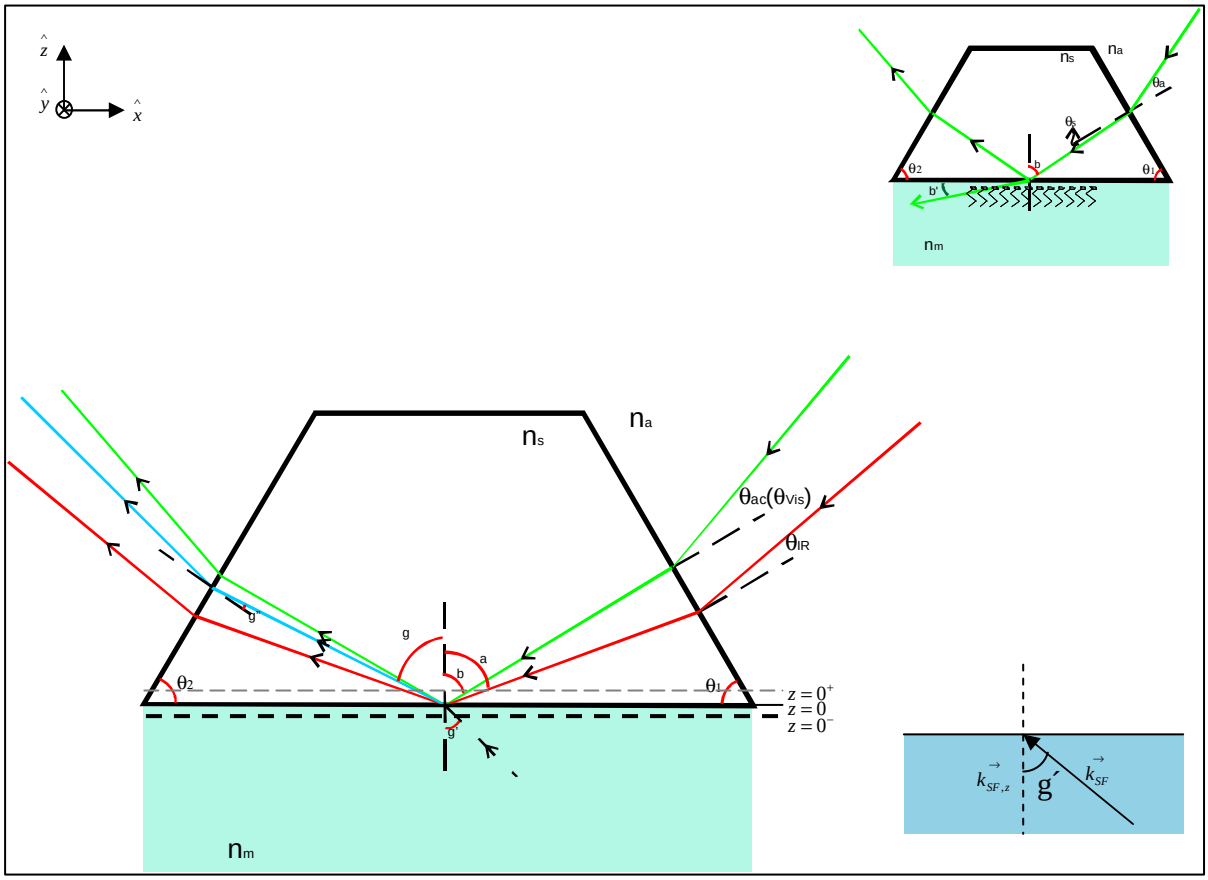

Figure 1-5 The prism substrate in contact with the medium. The arrows indicate the directions of incident beam and emitted signal, while the angles are analogous to those in the equations.

1.4 Optical Properties and Nonlinear Fresnel Factors

Generating fields and measured SFG field depend on linear optical properties of the interface, see equations (1.16) and (1.21). Therefore, consideration of linear optical properties of that interface is important. Before digging deeply in the optical properties of the interface, the sample (substrate) and the geometry of the experiment are described. The samples used in this study have the shape of prisms. Calculations of the prism dimensions as well as the angles of the incident and generated beams were reported in a previous work [26]. In the present work, a general case of prism dimensions and angles of the incident, reflected and refracted lights is considered. Figure 1-5 shows a conventional prism substrate of refractive index n_s in contact with a medium of refractive index n_m.

Some geometrical relations can be extracted from Figure 1-5 as described in the following:

From Snell's Law:

$$\begin{aligned} n_a \sin\theta_a &= n_s \sin\theta_s \\ n_s \sin b &= n_m \sin b' \\ \theta_s &= b - \theta_2 \end{aligned} \tag{1.29}$$

As will be discussed in the section of experimental setup (section 2.2), the SFG experiments in the presented work are carried in TIR configuration at the critical angle for the visible beam. In this configuration, the angle of refraction for the visible light is $b' = 90^\circ$ and the critical angle in the substrate is $b_c = \sin^{-1}(n_m / n_s)$. The corresponding critical angle from air θ_{ac} can be then derived as;

$$\theta_{ac} = \sin^{-1}\left(\frac{n_s}{n_a}\sin\left(\sin^{-1}\left(\frac{n_m}{n_p}\right) - \theta_2\right)\right) \tag{1.30}$$

Equation (1.30) is applicable for any three media including the medium which transports the laser beams to the experiment. Using this equation, the critical angle for the

visible light coming from air to the substrate and satisfying the TIR at the substrate/medium interface can be calculated.

1.4.1 The Nonlinear Fresnel Factors:

To use the linear Fresnel Coefficients, (see Appendix 2), in this model, they needed to be reformed as functions of two refractive indices and one angle, (the incident angle);

$$t^{p}(n_1,n_2,\theta)=\frac{2\sin\left(\sin^{-1}(\frac{n_1}{n_2}\sin(\theta))\right)\cos(\theta)}{\sin\left(\sin^{-1}(\frac{n_1}{n_2}\sin(\theta)+\theta)\right)\cos\left(\theta-\sin^{-1}(\frac{n_1}{n_2}\sin(\theta))\right)}$$ Transmission for p-polarization

$$r^{p}(n_1,n_2,\theta)=\frac{-n_1\cos\left(\sin^{-1}(\frac{n_1}{n_2}\sin(\theta))\right)+n_2\cos(\theta)}{n_2\cos(\theta)+n_1\cos\left(\sin^{-1}(\frac{n_1}{n_2}\sin(\theta))\right)}$$ Reflection for p-polarization

$$t^{s}(n_1,n_2,\theta)=\frac{2n_1\cos(\theta)}{n_1\cos(x)+n_2\cos\left(\sin^{-1}(\frac{n_1}{n_2}\sin(\theta))\right)}$$ Transmission for s-polarization

$$r^{s}(n_1,n_2,\theta)=\frac{n_1\cos(\theta)-n_2\cos\left(\sin^{-1}(\frac{n_1}{n_2}\sin(\theta))\right)}{n_1\cos(\theta)+n_2\cos\left(\sin^{-1}(\frac{n_1}{n_2}\sin(\theta))\right)}$$ Reflection for s-polarization

(1.31)

To understand the physical meaning behind the above formulae, a graphical representation is used. It is worth to mention that these formulae are complex quantities in the applied range of the incident angles. Therefore, they can be only plotted in terms of their absolute values. Figure 1-6 shows a graphical representation of the above formulae for sapphire, $n_1=1.771$, as a substrate and methanol, $n_2=1.3284$, as a contact medium.

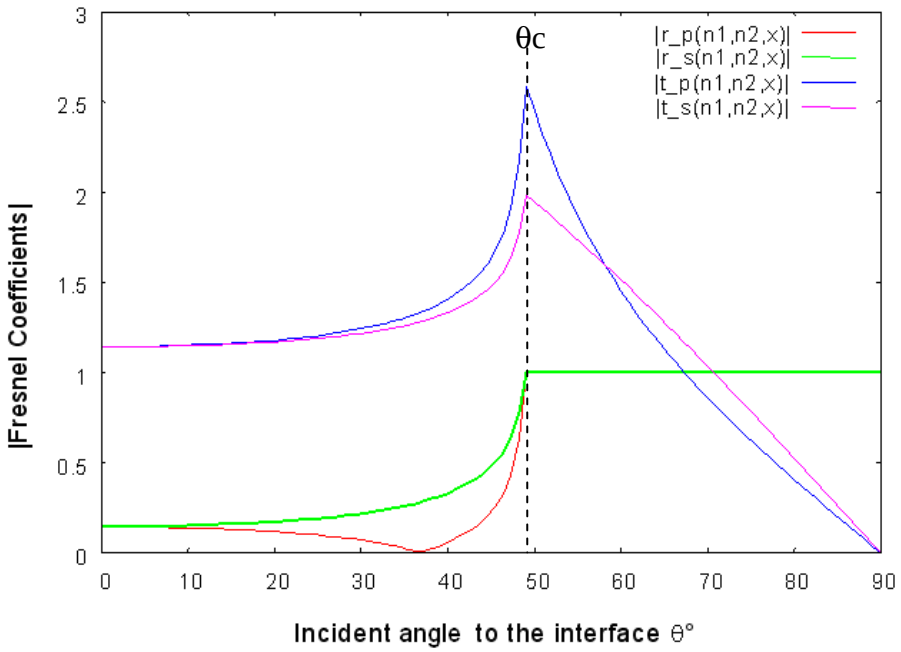

Figure 1-6 The Linear Fresnel coefficients at the sapphire/methanol interface

The most interesting information one can learn from Figure 1-6 is that the critical angle θ_c is a good choice for high efficiency, but small deviation from this angle may lead to a significant change in the Fresnel Coefficients. As seen in equations (1.18) and (1.24), the nonlinear Fresnel Factors, represented as $\mathbf{e}$-factors, are dependent on the linear Fresnel Factors. Therefore the enhancement of the generated signal is also highly sensitive to the incident angle in the vicinity of the critical angle. This means that special attention should be paid when setting up the experiment and aligning the beams.

Similar to the case of the linear Fresnel Factors, the nonlinear Fresnel Factors are given here in a general form and then tested for a special case of sapphire/methanol interface. Pondering on Figure 1-5 and using Fresnel Coefficients (equations (1.31)) in the $\mathbf{e}$-factors (equations (1.18) and (1.24)) the complete set of $\mathbf{e}$-factors can be obtained. The resultant $\mathbf{e}$-factors for the three beams are given as follows:

(1) For the incident tunable IR from the substrate side,

$$e_x^{IR}(n_{s,IR},n_{m,IR},a)=\left(1-r^p\left(n_{s,IR},n_{m,IR},a\right)\right)\cdot t^p\left(n_a,n_{s,IR},sin^{-1}\left(\frac{n_{s,IR}}{n_a}sin\left(\theta_2-a\right)\right)\right)\cdot cos(a)$$

$$e_y^{IR}(n_{s,IR}, n_{m,IR}, a) = \left(1 + r^s\left(n_{s,IR}, n_{m,IR}, a\right)\right) \cdot t^s\left(n_a, n_{s,IR}, \sin^{-1}\left(\frac{n_{s,IR}}{n_a}\sin\left(\theta_2 - a\right)\right)\right)$$

$$e_z^{IR}(n_{s,IR}, n_{m,IR}, a) = \left(1 + r^p\left(n_{s,IR}, n_{m,IR}, a\right)\right) \cdot t^p\left(n_a, n_{s,IR}, \sin^{-1}\left(\frac{n_{s,IR}}{n_a}\sin\left(\theta_2 - a\right)\right)\right).\sin(a)$$

(1.32)

(2) For the incident fundamental visible from the substrate side,

$$e_x^{Vis}(n_{s,Vis}, n_{m,Vis}, b) = \left(1 - r^p\left(n_{s,Vis}, n_{m,Vis}, b\right)\right) \cdot t^p\left(n_a, n_{s,Vis}, \sin^{-1}\left(\frac{n_{s,Vis}}{n_a}\sin\left(\theta_2 - b\right)\right)\right).\cos(b)$$

$$e_y^{Vis}(n_{s,Vis}, n_{m,Vis}, b) = \left(1 + r^s\left(n_{s,Vis}, n_{m,Vis}, b\right)\right) \cdot t^s\left(n_a, n_{s,Vis}, \sin^{-1}\left(\frac{n_{s,Vis}}{n_a}\sin\left(\theta_2 - b\right)\right)\right)$$

$$e_z^{Vis}(n_{s,Vis}, n_{m,Vis}, b) = \left(1 + r^p\left(n_{s,Vis}, n_{m,Vis}, b\right)\right) \cdot t^p\left(n_a, n_{s,Vis}, \sin^{-1}\left(\frac{n_{s,Vis}}{n_a}\sin\left(\theta_2 - a\right)\right)\right).\sin(b)$$

(1.33)

(3) For the emitted nonlinear SFG signal into the substrate,

$$e_x^{SF}(n_{s,SF}, n_{m,SF}, g) = t^p\left(n_{s,SF}, n_a, \theta_2 - g\right) \cdot t^p\left(n_{m,SF}, n_{s,SF}, \sin^{-1}\left(\frac{n_{s,SF}}{n_{m,SF}}\sin\left(g\right)\right)\right).\cos\left(\sin^{-1}\left(\frac{n_{s,SF}}{n_{m,SF}}\sin(g)\right)\right)$$

$$e_y^{SF}(n_{s,SF}, n_{m,SF}, g) = t^s\left(n_{s,SF}, n_a, \theta_2 - g\right) \cdot t^s\left(n_{m,SF}, n_{s,SF}, \sin^{-1}\left(\frac{n_{s,SF}}{n_{m,SF}}\sin\left(g\right)\right)\right)$$

$$e_z^{SF}(n_{s,SF}, n_{m,SF}, g) = t_p\left(n_{s,SF}, n_a, \theta_2 - g\right) \cdot t_p\left(n_{m,SF}, n_{s,SF}, \sin^{-1}\left(\frac{n_{s,SF}}{n_{m,SF}}\sin\left(g\right)\right)\right).\sin\left(\sin^{-1}\left(\frac{n_{s,SF}}{n_{m,SF}}\sin(g)\right)\right)$$

(1.34)

Figure 1-7 shows the change of the **e**-factors with the incident IR frequency in the range of 2500cm^{-1}-4000cm^{-1} for sapphire/methanol interface. The absolute values of the complex Fresnel Coefficients, for the IR and SFG, were plotted against the incident tunable IR frequency (in cm^{-1} units). The coefficients for the visible light were not plotted because they are simply constants. The complex refractive indices of sapphire and methanol as a function of wavenumbers were taken from literature, [27] and [28] respectively.

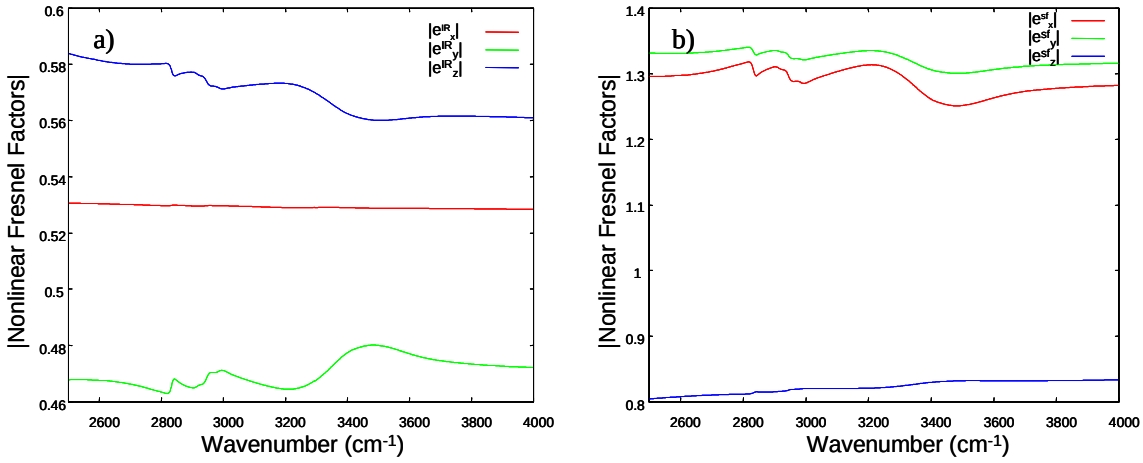

Figure 1-7 The absolute values of the nonlinear Fresnel factors for Sapphire/Methanol interface in the directions x, y and z for a) the IR incident light, and b) the generated SFG.

It is worth to mention that in this study the SFG angle was not taken as an approximated constant rather as a variable calculated from the momentum equation;

$$\theta_{SF} = Sin^{-1}\left(\frac{n_{Vis}\omega_{Vis}Sin\theta_{Vis} + n_{IR}\omega_{IR}Sin\theta_{IR}}{n_{SF}\omega_{SF}}\right) \tag{1.35}$$

where $\theta_{SF} = g$, $\theta_{Vis} = b$ and $\theta_{IR} = a$ regarding to the drawing shown in Figure 1-5

It is clear that θ_{SF} is a function of the IR wavenumber, see Figure 1-8. The refractive indices, $n_{IR}(\omega_{IR})$ and $n_{SF}(\omega_{SF})$, were taken also as functions of the incident IR and the generated SFG wavenumbers respectively, and they are complex quantities carrying information about the real (dispersion) and imaginary (absorption) parts.

Finally the *Geometry Factors* ($Geo_{SSP}, Geo_{PPP}, Geo_{PSP}, ...etc$), with which the detected SFG signal can be corrected, are defined as a combination of these nonlinear Fresnel Factors multiplied by the parameters found in equation (1.26).

$$Geo_{IJK} = \frac{\omega_{SF}\sec(g')}{n_m(\omega_{SF})}\left|\mathbf{e}_i^{SF} \bullet \mathbf{e}_j^{Vis} \bullet \mathbf{e}_k^{IR}\right| \tag{1.36}$$

where $IJK \in \{S, P\}$ and $ijk \in \{x, y, z\}$. The choice of *i*, *j* and *k* is χ^s_{ijk} dependent as explained in subsection (1.5.1)

The geometry factors of three special cases of polarization combinations (SSP, PPP and SPS) are drawn in Figure 1-9, in the range of 2500cm^{-1}-4000cm^{-1}, for the butanol/sapphire interface. The complex refractive index of butanol as a function of wavenumbers was obtained independently in a reflectivity experiment carried out in TIR configuration (section 3.1).

Figure 1-9 together with the above discussion show the importance of considering the nonlinear Fresnel coefficients and the *Geometry Factors* to correct the measured SFG signal and reach valuable quantitative or qualitative results. It is obvious that the SFG signal obtained experimentally for SPS polarization combination is not directly comparable to that obtained for the PPP or SSP from the same interface. This variance arises from the different reflectivity at the interface and thus is not necessarily due to differences in the nonlinear response of the second order nonlinear susceptibility tensor, χ^s. The obtained SFG spectra should be normalized to the proper geometry factors to allow reliable comparisons between these spectra. More details about the data treatment will be discussed in section (2.6.2).

In Figure 1-9, the features of the IR absorption resonances of the bulk butanol are clearly discernible. The broadband centred at 3350 cm^{-1} corresponds to the bulk OH vibrations of the polymeric hydrogen bonded molecules while the narrow bands at the low wavenumber spectral region correspond to the CH vibrations of the hydrocarbon chain. The band assignments will be discussed in detail in the results and discussion chapter. One should distinguish between the Geometry Factors and the SFG spectrum. Actually, the plotting in Figure 1-9 is not a SFG spectrum and it is not even IR absorption or transmission although it is based on the absorption coefficients of the two media (the substrate and the liquid). Such features are absent from the Geometry Factors in the case of an air/sapphire interface (see Figure 3-3) in the presence of an adsorbed butanol layer although they can be observed in the SFG spectra of this interface.

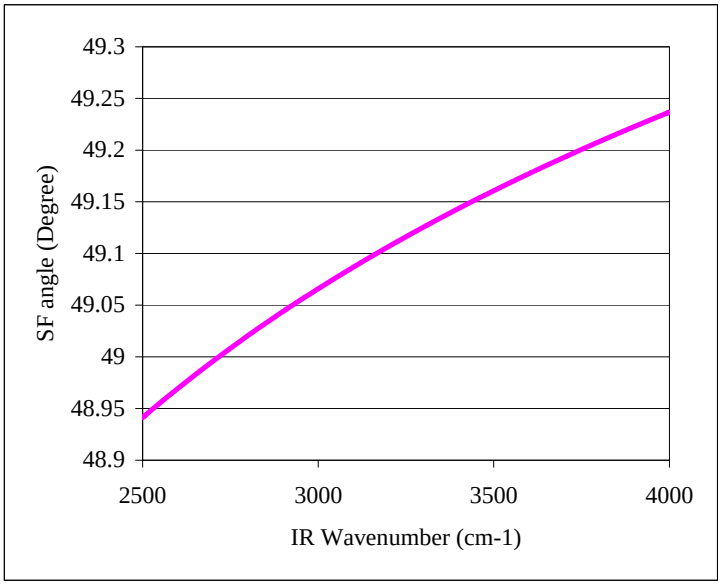

Figure 1.8 The angle of the emitted SF as a function of the incident IR wavenumber

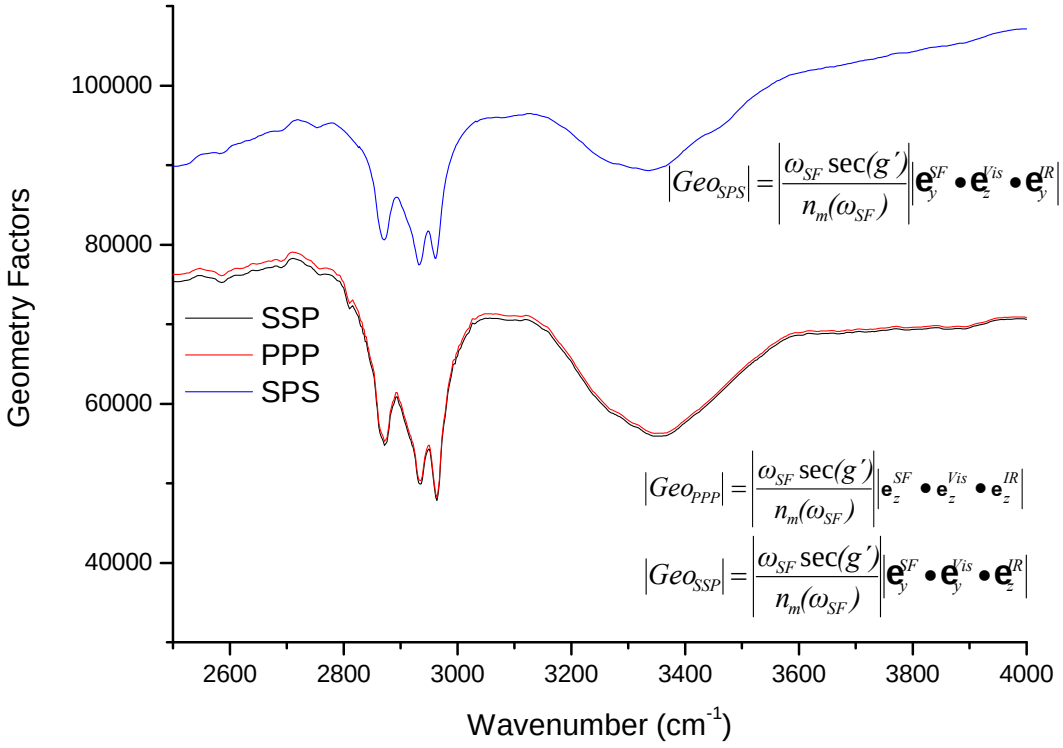

Figure 1.9 SSP and PPP Geometry factors for the sapphire/butanol interface.

1.4.2 The Optical constants:

As seen in the previous subsection, the optical constants of the liquid under study are crucial for accurate data analysis. Unfortunately the literature and data bases are lacking suitable data for the optical constants, i.e. one can find the optical constants for the required medium but in the unwanted range of wavelengths. Therefore, it is important to be able to measure the optical constants under the same experimental conditions as those used in the SFG measurements. Several methods were reported to measure optical constants, [28-34]. J. Bertie et al. [28] demonstrated good accuracy and reproducibility using *absorption transmition techniques* to investigate the optical constants of weakly absorbing materials. Their obtained optical constants for methanol were used in this study as a given values. However, *reflection techniques* are utilized for measuring the reflectivities at the IR region of strongly absorbing materials, from which the optical constants are extracted [31,34]. *Reflection*, particularly *Attenuated Total internal Reflection* (ATR), is the best technique which fits to our experimental conditions since it requires the same geometry used in the presented SFG measurements. In addition, it does not rely on sample thickness and is therefore also applicable to strongly absorbing media.

The optical constants, by which the spectroscopic properties of the matter are given, are described by the complex refractive index,

$$\hat{n}(\omega) = n(\omega) + ik(\omega),$$

(1.37)

which is frequency dependent. $n(\omega)$ is the real refractive index and $k(\omega)$ is the extinction coefficient

Recalling that the reflectivities, which can be measured experimentally at an interface, are given in terms of the Fresnel Coefficients r^p and r^s as,

$$R_p = \left|r^p\right|^2,$$
$$R_s = \left|r^s\right|^2,$$

(1.38)

for the p- and s- polarized lights respectively, they can be obtained as a function of the optical constants of the media as follows:

$$R_p(\hat{n}_1,\hat{n}_2,\theta)=\left|\frac{-\hat{n}_1\cos\left(\sin^{-1}(\frac{\hat{n}_1}{\hat{n}_2}\sin(\theta))\right)+\hat{n}_2\cos(\theta)}{\hat{n}_2\cos(\theta)+\hat{n}_1\cos\left(\sin^{-1}(\frac{\hat{n}_1}{\hat{n}_2}\sin(\theta))\right)}\right|^2,$$

$$R_s(\hat{n}_1,\hat{n}_2,\theta)=\left|\frac{\hat{n}_1\cos(\theta)-\hat{n}_2\cos\left(\sin^{-1}(\frac{\hat{n}_1}{\hat{n}_2}\sin(\theta))\right)}{\hat{n}_1\cos(\theta)+\hat{n}_2\cos\left(\sin^{-1}(\frac{\hat{n}_1}{\hat{n}_2}\sin(\theta))\right)}\right|^2$$

(1.39)

If the incident medium has known optical constants n_1,k_1, then measuring the reflectivities at a certain angle will give two equations with two unknowns, n_2,k_2. Solving equation (1.39) for n_2 and k_2 analytically is nearly impossible, however graphical and numerical solutions can be obtained. Figure 1-10 shows the reflectivities, as a function of the incident angle, corresponding to different values of n_2 and k_2. For simplicity, $\hat{n}_1$ was assumed as a real and constant value. The optical constants used in these curves are close to the real values of sapphire as the incident medium and 1-butanol as the liquid under investigation. From Figure 1-10, one can recognize the effect of the absorption as curve attenuation and the effect of the dispersion as horizontal shift in the reflectivities against the axis of the incidence angle.

If the reflectivities for only one polarization at certain wavelength were measured at different angles, a curve similar to one of those presented in Figure 1-10 is obtained. Then the obtained curve can be fit with the corresponding function from equation (1.39). This method gives accurate values for the optical constants provided that accurate measurements at, not little number of, different angles should be acquired. This requires a lot of experimental work and hence large uncertainty due to possible personal errors in the angle measurements. What about extensive calculations and minimum experimental work? As mentioned above, solving equation (1.40) for n_2 and k_2 needs a miracle but no doubt that there is only one set of (n_2,k_2) that satisfies R_p,R_s of the medium simultaneously. If the incident angle is kept constant and a 3D relation of $R_p(n_2,k_2)$ (or of $R_s(n_2,k_2)$ correspondingly) is plotted, a surface describing the dependency of R_p (R_s) on n_2 and k_2 can be obtained, Figure 1-11. The intersection of this surface with a horizontal plane at a given value of R_p (R_s) gives one

contour line of those shown at the base of the plotting. Each contour line represents the possible sets of (n_2, k_2) which give one value of R_p (R_s), *iso-reflectivity*. There is only one set of (n_2, k_2) satisfies a given value of R_p and a given value of R_s simultaneously. This set lies at the intersection of the two corresponding contours.

If we reduce the ranges of n_2, k_2 and increase the number of contour lines we can see the crossing contours better, Figure 1-12a. Figure 1-12b shows the 2D plotting of the contour lines (the base) of Figure 1-12a. By knowing the values of R_p and R_s experimentally at certain frequency, the corresponding optical constants of the medium can be determined at this frequency using Figure 1-12.

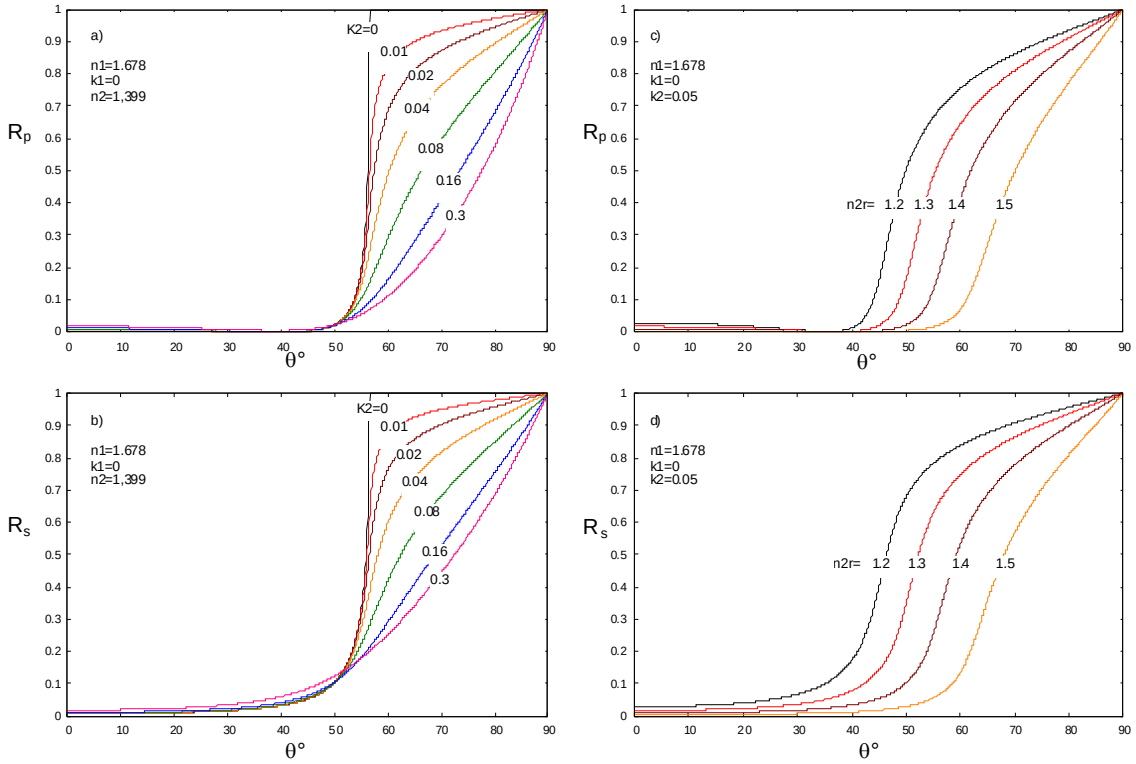

Figure 1.10 Reflectivities as a function of the incident angle at different absorption indices (a, b) and refractive indices (c, d) of the liquid

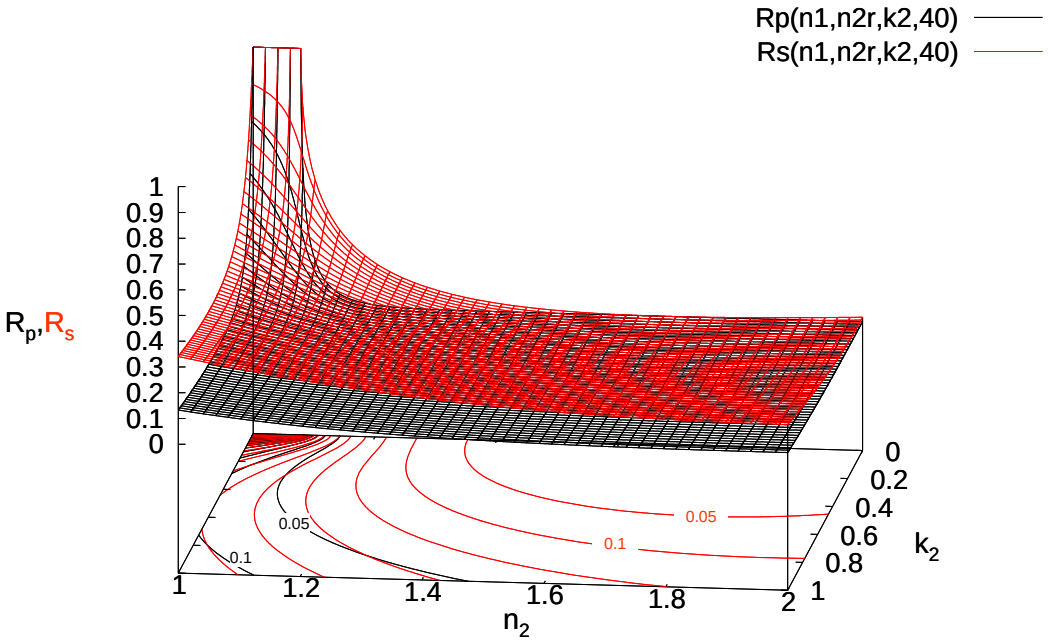

Figure 1.11: 3D plot of $R_p(n_2,k_2)$ and $R_s(n_2,k_2)$ at constant angle 40° and $n_1 = 1.678$.

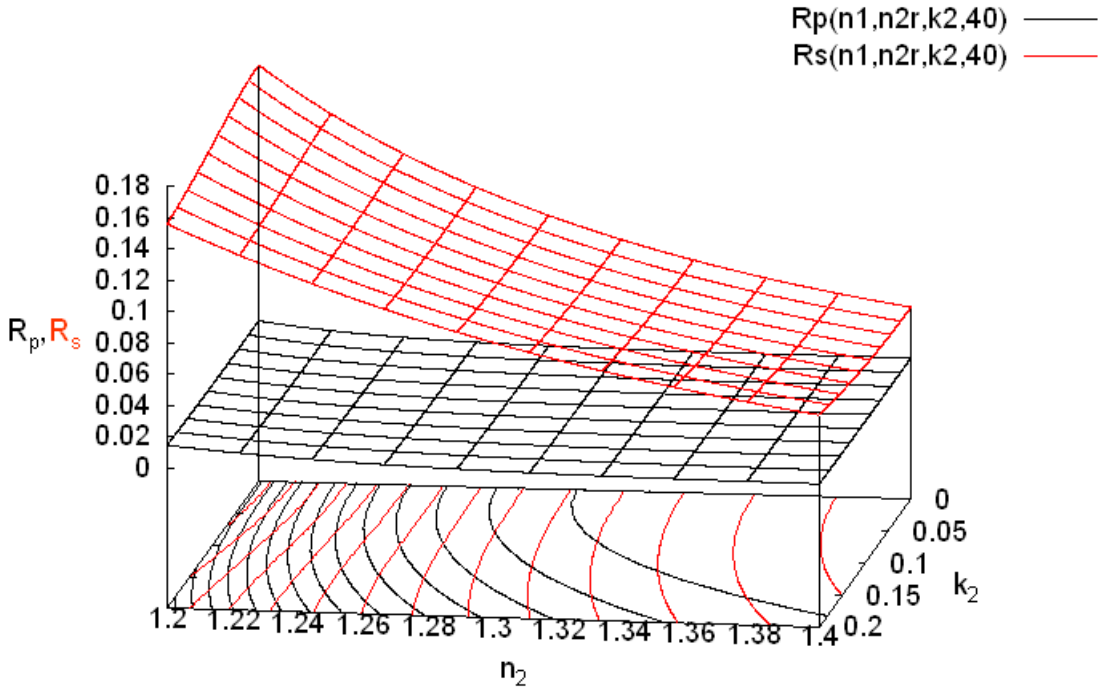

(a)

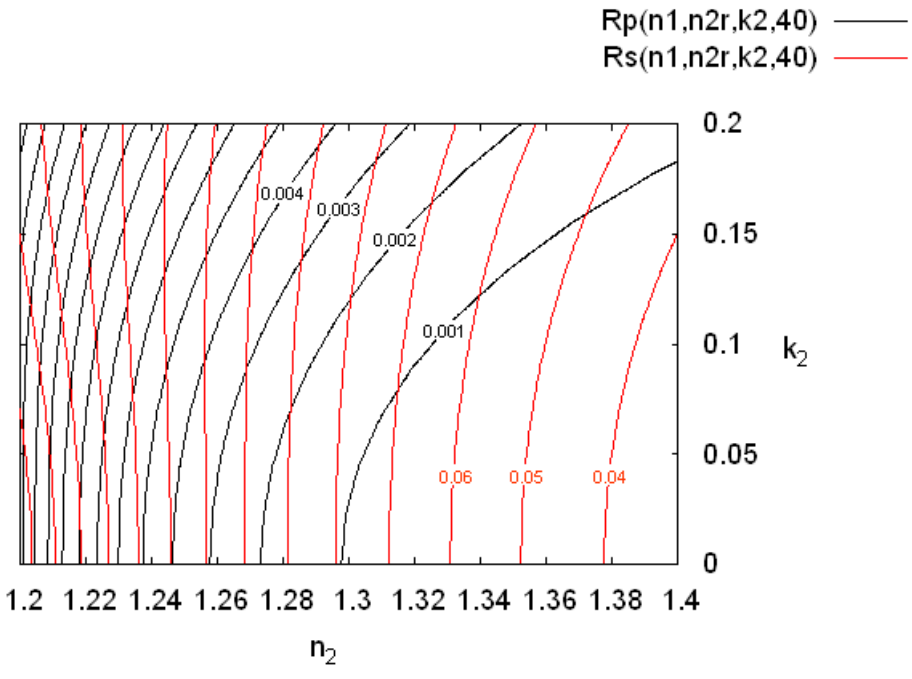

(b)

Figure 1.12 Zooming in the 3D plot of $R_p(n_2,k_2)$ and $R_s(n_2,k_2)$ at constant angle 40° and $n_1=1.678$, and the corresponding contours of constant R_p and R_s values

1.5 Macroscopic and Molecular Hyperpolarizability Tensors (χ^s_{IJK} , $\beta^s_{\alpha\beta\gamma}$)

1.5.1 Macroscopic hyperpolarizability tensor (χ^s_{IJK})

The field of the generated sum-frequency light is described by the macroscopic second order nonlinear susceptibility, χ^s_{IJK}, see equation (1.26). This term contains the chemical information, or more precisely, the nonlinear vibrational response, of the system under study. The generated sum-frequency light is described by the macroscopic second order nonlinear susceptibility. In the present experiments the SFG signal is detected while the frequency of the IR beam (ω_{IR}) is tuned. During the spectral scan, the frequency of the IR beam crosses the resonance frequencies of the functional groups under study. The laboratory coordinates are related to the surface coordinates by the following relation:

$$\chi^s_{IJK} = \sum_{ijk} U_{IJK;ijk} \chi^s_{ijk} \tag{1.40}$$

where $U_{IJK;ijk}$ is the transformation matrix from surface coordinates to laboratory coordinates, $IJK = X,Y,Z$ and $ijk = x,y,z$. The Macroscopic second order susceptibility tensor χ^s_{ijk} is expressed in terms of the ensemble average of the microscopic hyperpolarizability tensor β^s_{ijk} as follows:

$$\chi^s_{ijk} = N\left\langle \beta^s_{ijk} \right\rangle \tag{1.41}$$

where N is the number of sites or molecules contributing to the SFG signal. The microscopic quantities are best described by the molecule fixed coordinate system (a,b,c).This means that we need to transfer these quantities from the (a,b,c) system to their corresponding values in the (x,y,z) system.

$$\beta^s_{ijk} = \sum_{\alpha\beta\gamma} U_{ijk;\alpha\beta\gamma} \beta^s_{\alpha\beta\gamma} \tag{1.42}$$

where $U_{ijk;\alpha\beta\gamma}$ is the transformation coefficient which define the mutual orientation of (a,b,c) system and (x,y,z) system through the Euler angles, Figure 1-13

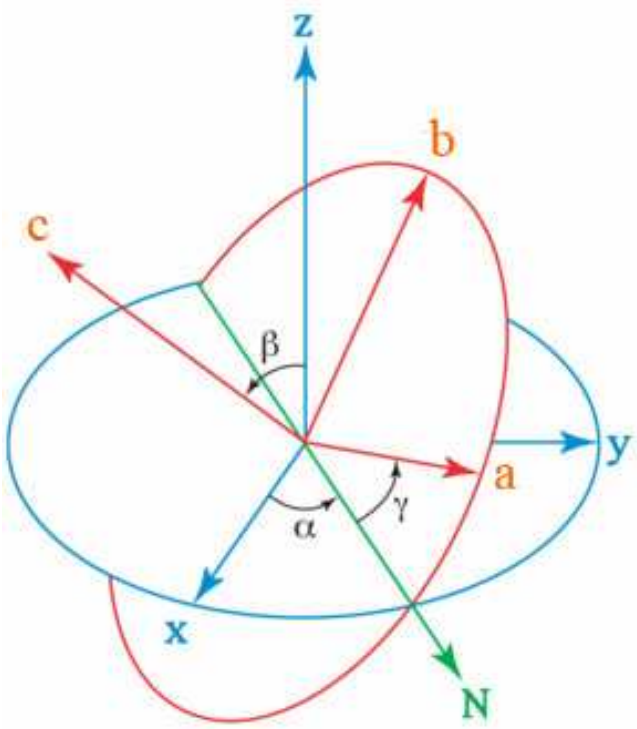

Figure 1-13 The Euler transformation between the surface coordinates xyz and the molecular coordinates abc through the Euler angles (α, β, γ).

In this work, the Euler angles are defined as follows: (starting with the *xyz*-frame),

1. Rotation with an angle α around the z-axis => *x* is transformed to $\mathbb{N}$ (The Node-line between the starting *x*-*y* plane and the final a-b plane)
2. Rotation with an angle β around the new *x*-axis ($\mathbb{N}$) => *z* is transformed to c
3. Finally, rotation with an angle γ around the new *z*-axis (*c*) => *x* is transformed to *a*, and *y* is transformed to *b*

This can be expressed in the matrix notation as follows: (refer to Appendix 3)

$$U = \begin{pmatrix} \cos(\gamma)\cos(\alpha) - \sin(\gamma)\sin(\alpha)\cos(\beta) & -\cos(\gamma)\sin(\alpha)\cos(\beta) - \sin(\gamma)\cos(\alpha) & \sin(\gamma)\sin(\beta) \\ -\cos(\gamma)\sin(\alpha)\cos(\beta) - \sin(\gamma)\cos(\alpha) & \cos(\gamma)\cos(\alpha)\cos(\beta) - \sin(\gamma)\sin(\alpha) & \cos(\gamma)\sin(\beta) \\ \sin(\alpha)\sin(\beta) & -\cos(\alpha)\sin(q) & \cos(\beta) \end{pmatrix} \tag{1.43}$$

This matrix is a transformation operator from the original coordinate system to the molecular coordinate system. To express the molecular coordinate in terms of the original coordinate we can use the Transposed Matrix, U^{-1}, then,

$$\begin{pmatrix} x \\ y \\ z \end{pmatrix} = U^{-1} \begin{pmatrix} a \\ b \\ c \end{pmatrix}$$

$$\begin{pmatrix} x \\ y \\ z \end{pmatrix} = \begin{pmatrix} \cos(\gamma)\cos(\alpha) - \sin(\gamma)\sin(\alpha)\cos(\beta) & -\cos(\gamma)\sin(\alpha)\cos(\beta) - \sin(\gamma)\cos(\mathrm{f}) & \sin(\alpha)\sin(\beta) \\ \sin(\gamma)\cos(\alpha)\cos(\beta) + \cos(\gamma)\sin(\alpha) & \cos(\gamma)\cos(\alpha)\cos(\beta) - \sin(\gamma)\sin(\alpha) & -\cos(\alpha)\sin(\beta) \\ \sin(\gamma)\sin(\beta) & \cos(\gamma)\sin(\beta) & \cos(\beta) \end{pmatrix} \begin{pmatrix} a \\ b \\ c \end{pmatrix}$$

or,

$$\begin{pmatrix} x \\ y \\ z \end{pmatrix} = \begin{pmatrix} u_{xa}^{-1} & u_{xb}^{-1} & u_{xc}^{-1} \\ u_{ya}^{-1} & u_{yb}^{-1} & u_{yc}^{-1} \\ u_{za}^{-1} & u_{zb}^{-1} & u_{zc}^{-1} \end{pmatrix} \begin{pmatrix} a \\ b \\ c \end{pmatrix}$$

(1.44)

One should not confuse the Euler angles $\alpha\beta\gamma$ with the summation indices $\alpha\beta\gamma$ of equation (1.42). Equation (1.42) can be written as:

$$\beta_{ijk}^{s} = \sum_{\alpha\beta\gamma} \begin{pmatrix} u_{xa}^{-1} & u_{xb}^{-1} & u_{xc}^{-1} \\ u_{ya}^{-1} & u_{yb}^{-1} & u_{yc}^{-1} \\ u_{za}^{-1} & u_{zb}^{-1} & u_{zc}^{-1} \end{pmatrix} \beta_{\alpha\beta\gamma}^{s}$$

(1.45)

This means that, for example,

$$\beta_{xxz}^{s} = u_{xa}^{-1}u_{xa}^{-1}u_{za}^{-1}\beta_{aaa}^{s} + u_{xb}^{-1}u_{xb}^{-1}u_{zb}^{-1}\beta_{bbb}^{s} + u_{xc}^{-1}u_{xc}^{-1}u_{zc}^{-1}\beta_{ccc}^{s} + u_{xa}^{-1}u_{xb}^{-1}u_{zc}^{-1}\beta_{abc}^{s} ...etc$$

(1.46)

which has 27 terms. Most of them, however, can be zero due to the group symmetry of the molecule as will be explained in the next section.

Let us consider the simple case of $C_{\infty\upsilon}$ -symmetry (OH has such symmetry). The non-zero hyperpolarizability terms in this case are $\beta_{aac} = \beta_{bbc} = R\beta_{ccc}$ where R is a factor equal to the bond polarizability derivative ratio, [35,37]. From equations (1.43) and (1.46),

$$\beta_{xxz}^{s} = u_{xa}^{-1}u_{xa}^{-1}u_{zc}^{-1}\beta_{aac}^{s} + u_{xb}^{-1}u_{xb}^{-1}u_{zc}^{-1}\beta_{bbc}^{s} + u_{xc}^{-1}u_{xc}^{-1}u_{zc}^{-1}\beta_{ccc}^{s}$$

$$\beta_{\mathrm{xxz}} = \beta_{\mathrm{ccc}}\cos(\beta)\begin{bmatrix} \sin(\gamma)^2\sin(\alpha)^2\cos(\beta)^2\mathrm{R} + \cos(\gamma)^2\sin(\alpha)^2\cos(\beta)^2\mathrm{R} + \\ \sin(\gamma)^2\cos(\alpha)^2\mathrm{R} + \cos(\gamma)^2\cos(\alpha)^2\mathrm{R} + \sin(\alpha)^2\sin(\beta)^2 \end{bmatrix}$$

(1.47)

Now one can obtain the macroscopic second order susceptibility tensor χ^s_{ijk} using some assumptions:

1. There is a large number of molecules at the probed site. This enables integration instead of summation in equation (1.41) to determine the averaged β^s_{ijk}.
2. Assume rotation symmetry around the bond axis (c-axis). Hence the integration takes place from $\gamma = 0$ to 2π.
3. Assume rotation symmetry around the sample normal (z-axis). Hence the integration takes place from $\alpha = 0$ to 2π.
4. All members of the same species have the same polar orientation β_o with respect to the surface normal. Hence the integration takes place from $\beta = 0$ to π and is governed by the Dirac Delta function, $\delta(\beta - \beta_o)$.

Thus equation (1.41) can be written as:

$$\chi^s_{ijk} = N\int_0^{\pi}\delta(\beta-\beta_o)d\beta\int_0^{2\pi}\frac{1}{2\pi}d\alpha\int_0^{2\pi}\frac{1}{2\pi}d\gamma\beta^s_{ijk} \tag{1.48}$$

Applying this equation to the selected simple case ($C_{\infty\upsilon}$) gives:

$$\chi^s_{xxz} = \frac{N}{4\pi^2}\int_{\beta=0}^{\pi}\int_{\alpha=0}^{2\pi}\int_{\gamma=0}^{2\pi}\delta(\beta-\beta_o)\beta_{ccc}\cos(\beta)\begin{pmatrix}\sin(\gamma)^2\sin(\alpha)^2\cos(\beta)^2\mathrm{R}+\\ \cos(\gamma)^2\sin(\alpha)^2\cos(\beta)^2\mathrm{R}+\\ \sin(\gamma)^2\cos(\alpha)^2\mathrm{R}+\\ \cos(\gamma)^2\cos(\alpha)^2\mathrm{R}+\sin(\alpha)^2\sin(\beta)^2\end{pmatrix}d\beta d\alpha d\gamma \tag{1.49}$$

After integrations and simplifications, using wxMaxima software[2], the following result was obtained:

$$\chi^s_{xxz} = \frac{N}{2}\beta_{ccc}\cos(\beta)\left(\mathrm{R}(1+\cos(\beta)^2)+\sin(\beta)^2\right) \tag{1.50}$$

[2] http://wxmaxima.sourceforge.net/wiki/index.php/Main_Page

Using the same procedure, the macroscopic second order susceptibility tensors can be obtained as show in the following Table 1.1

The non-zero macroscopic second order susceptibility tensors		The G. Sym. and the corresponding non-zero hyper-pol. tensor elements
$\chi^s_{xxz} = \chi^s_{yyz}$	$\frac{N}{2}\beta_{ccc}\cos(\beta)\left(R(1+\cos(\beta)^2)+\sin(\beta)^2\right)$	$C_{\infty\upsilon}$ **- (OH, CH, …)** $C_{3\upsilon}$ **Symmetric Stretching (SS) - (CH_3, NH_3, …)** $\left(\beta_{aac}=\beta_{bbc}=R\beta_{ccc}\right)$
$\chi^s_{xzx} = \chi^s_{zxx} = \chi^s_{yzy} = \chi^s_{zyy}$	$\frac{N}{2}\beta_{ccc}\cos(\beta)\sin(\beta)^2(1-R)$	
χ^s_{zzz}	$N\beta_{ccc}\cos(\beta)\left(R\sin(\beta)^2+\cos(\beta)^2\right)$	
$\chi^s_{xxz} = \chi^s_{yyz}$	$-N\beta_{aca}\cos(\beta)\sin(\beta)^2$	$C_{3\upsilon}$ **Asymmetric Stretching (AS) - (CH_3, NH_3, …)** $\left(\begin{array}{l}\beta_{aca}=\beta_{bcb},\\ \beta_{caa}=\beta_{cbb},\\ \beta_{aaa}=-\beta_{bba}=-\beta_{abb}=-\beta_{bab}\end{array}\right)$
$\chi^s_{xzx} = \chi^s_{zxx} = \chi^s_{yzy} = \chi^s_{zyy}$	$N\beta_{aca}\cos(\beta)^3$	
χ^s_{zzz}	$2N\beta_{aca}\cos(\beta)\sin(\beta)^2$	
$\chi^s_{xxz} = \chi^s_{yyz}$	$\frac{N}{2}\cos(\beta)\left[\left(\langle\cos(\gamma)^2\rangle\beta_{aac}+\langle\sin(\gamma)^2\rangle\beta_{bbc}+\beta_{ccc}\right)+\left(\langle\sin(\gamma)^2\rangle\beta_{aac}+\langle\cos(\gamma)^2\rangle\beta_{bbc}-\beta_{ccc}\right)\cos(\beta)^2\right]$	$C_{2\upsilon}$ **Symmetric Stretching (SS) - (CH_2)** * $\left(\beta_{aac},\beta_{bbc},\beta_{ccc}\right)$
$\chi^s_{xzx} = \chi^s_{zxx} = \chi^s_{yzy} = \chi^s_{zyy}$	$\frac{N}{2}\cos(\beta)\sin(\beta)^2.\left(\langle\sin(\gamma)^2\rangle\beta_{aac}+\langle\cos(\gamma)^2\rangle\beta_{bbc}-\beta_{ccc}\right)$ **	
χ^s_{zzz}	$N\cos(\beta)\left[\left(\langle\sin(\gamma)^2\rangle\beta_{aac}+\langle\cos(\gamma)^2\rangle\beta_{bbc}\right)+\left(\langle\sin(\gamma)^2\rangle\beta_{aac}+\langle\cos(\gamma)^2\rangle\beta_{bbc}-\beta_{ccc}\right)\cos(\beta)^2\right]$	
$\chi^s_{xxz} = \chi^s_{yyz}$	$-N\beta_{ijk}\cos(\beta)\sin(\beta)^2\langle\sin(\gamma)^2\rangle$	$C_{2\upsilon}$ **Asymmetric Stretching (AS) - (CH_2)*** $\left(\begin{array}{l}\beta_{aca}=\beta_{caa},\\ \beta_{bcb}=\beta_{cbb}\end{array}\right)$ **AS-b$_1$ =>** $\beta_{ijk} = \beta_{aca}$ **AS-b$_2$ =>** $\beta_{ijk} = \beta_{bcb}$
$\chi^s_{xzx} = \chi^s_{zxx} = \chi^s_{yzy} = \chi^s_{zyy}$	$-\frac{N}{2}\beta_{ijk}\cos(\beta)\left(1-2\langle\cos(\gamma)^2\rangle-2\langle\sin(\gamma)^2\rangle\cos(\beta)^2\right)$	
χ^s_{zzz}	$2N\beta_{ijk}\cos(\beta)\sin(\beta)^2\langle\sin(\gamma)^2\rangle$	

Table 1.1: The non-zero tensor elements, of the nonlinear susceptibility tensor, corresponding to the symmetry groups describing the molecules used in this work. * For $C_{2\upsilon}$ -symmetry, if the CH_2 group can rotate freely around the c-axis then $\langle\sin(\gamma)^2\rangle=\langle\cos(\gamma)^2\rangle=1/2$. R=0.32, 3.4 and 0.27 for $C_{\infty\upsilon}$, $C_{3\upsilon}$ and $C_{2\upsilon}$, respectively

It is worth to mention that for CH_2 $\beta_{aac} + \beta_{bbc} = 2\beta_{ccc}$. This reduces equation (**), in Table 1.1, to $\chi^s_{xzx} = \chi^s_{zxx} = \chi^s_{yzy} = \chi^s_{zyy}$=0 for freely rotating H-C-H group ($\langle \sin(\gamma)^2 \rangle = \langle \cos(\gamma)^2 \rangle = 1/2$). Thus, according to Table 1.2, a freely rotating H-C-H group should not generate any SPS or PSS signal. Observing signal from these polarization combinations means that the twist angle γ cannot be rotationally averaged and hence $\langle \sin(\gamma)^2 \rangle, \langle \cos(\gamma)^2 \rangle \neq 1/2$.

The next step is to connect the laboratory coordinates with the macroscopic second order susceptibility tensors. The complex amplitude of the non-linear polarization at sum frequency $P^s(\omega_1 + \omega_2)$, equation (1.4), can be written as:

$$P^s(\omega_1+\omega_2) = 2\varepsilon_o \begin{pmatrix} \chi_{xxx} & \chi_{xyy} & \chi_{xzz} & \chi_{xyz} & \chi_{xxz} & \chi_{xxy} & \chi_{xzy} & \chi_{xzx} & \chi_{xyx} \\ \chi_{yxx} & \chi_{yyy} & \chi_{yzz} & \chi_{yyz} & \chi_{yxz} & \chi_{yxy} & \chi_{yzy} & \chi_{yzx} & \chi_{yyx} \\ \chi_{zxx} & \chi_{zyy} & \chi_{zzz} & \chi_{zyz} & \chi_{zxz} & \chi_{zxy} & \chi_{zzy} & \chi_{zzx} & \chi_{zyx} \end{pmatrix} \begin{pmatrix} A_x(\omega_1)A_x^*(\omega_2) \\ A_y(\omega_1)A_y^*(\omega_2) \\ A_z(\omega_1)A_z^*(\omega_2) \\ A_y(\omega_1)A_z^*(\omega_2) + A_z(\omega_1)A_y^*(\omega_2) \\ A_x(\omega_1)A_z^*(\omega_2) + A_z(\omega_1)A_x^*(\omega_2) \\ A_x(\omega_1)A_y^*(\omega_2) + A_y(\omega_1)A_x^*(\omega_2) \\ A_z(\omega_1)A_y^*(\omega_2) + A_y(\omega_1)A_z^*(\omega_2) \\ A_z(\omega_1)A_x^*(\omega_2) + A_x(\omega_1)A_z^*(\omega_2) \\ A_y(\omega_1)A_x^*(\omega_2) + A_x(\omega_1)A_y^*(\omega_2) \end{pmatrix} \tag{1.51}$$

Recalling our simple case $C_{\infty\upsilon}$, only seven tensors from the above equation are non-zero, see Table 1.1. This yields the following result:

$$P^s(\omega_1+\omega_2) = 2\varepsilon_o \begin{pmatrix} 0 & 0 & 0 & 0 & \chi_{xxz} & 0 & 0 & \chi_{xzx} & 0 \\ 0 & 0 & 0 & \chi_{yyz} & 0 & 0 & \chi_{yzy} & 0 & 0 \\ \chi_{zxx} & \chi_{zyy} & \chi_{zzz} & 0 & 0 & 0 & 0 & 0 & 0 \end{pmatrix} \begin{pmatrix} A_x(\omega_1)A_x^*(\omega_2) \\ A_y(\omega_1)A_y^*(\omega_2) \\ A_z(\omega_1)A_z^*(\omega_2) \\ A_y(\omega_1)A_z^*(\omega_2) + A_z(\omega_1)A_y^*(\omega_2) \\ A_x(\omega_1)A_z^*(\omega_2) + A_z(\omega_1)A_x^*(\omega_2) \\ A_x(\omega_1)A_y^*(\omega_2) + A_y(\omega_1)A_x^*(\omega_2) \\ A_z(\omega_1)A_y^*(\omega_2) + A_y(\omega_1)A_z^*(\omega_2) \\ A_z(\omega_1)A_x^*(\omega_2) + A_x(\omega_1)A_z^*(\omega_2) \\ A_y(\omega_1)A_x^*(\omega_2) + A_x(\omega_1)A_y^*(\omega_2) \end{pmatrix}$$

$$= 2\varepsilon_o \begin{pmatrix} \left(A_x(\omega_1)A_z^*(\omega_2) + A_z(\omega_1)A_x^*(\omega_2)\right)\chi_{xxz} + \left(A_z(\omega_1)A_x^*(\omega_2) + A_x(\omega_1)A_z^*(\omega_2)\right)\chi_{xzx} \\ \left(A_y(\omega_1)A_z^*(\omega_2) + A_z(\omega_1)A_y^*(\omega_2)\right)\chi_{yyz} + \left(A_z(\omega_1)A_y^*(\omega_2) + A_y(\omega_1)A_z^*(\omega_2)\right)\chi_{yzy} \\ \left(A_x(\omega_1)A_x^*(\omega_2)\right)\chi_{zxx} + \left(A_y(\omega_1)A_y^*(\omega_2)\right)\chi_{zyy} + \left(A_z(\omega_1)A_z^*(\omega_2)\right)\chi_{zzz} \end{pmatrix}$$

(1.52)

In the laboratory coordinates we use the $S \equiv \begin{pmatrix} 0 \\ y \\ 0 \end{pmatrix}$ and $P \equiv \begin{pmatrix} x \\ 0 \\ z \end{pmatrix}$ notations for S-polarized light and P-Polarized light respectively. This means that if we measure SSP configuration we will consider only tensor elements which have indices of *yyx* or *yyz* (i.e. χ_{yyx} or χ_{yyz}). In addition, only the *y*-component of the incident visible light and the *x*- and/or *z*- components of the incident IR are not zero. This reduces equation (1.52) to:

$$P^s_{SSP}(\omega_1+\omega_2) = 2\varepsilon_o \begin{pmatrix} 0 \\ A_y(\omega_1)A^*_z(\omega_2)\chi_{yyz} \\ 0 \end{pmatrix}$$

Similarly, we can find that:

$$P^s_{SPS}(\omega_1+\omega_2) = 2\varepsilon_o \begin{pmatrix} 0 \\ A_z(\omega_1)A^*_y(\omega_2)\chi_{yzy} \\ 0 \end{pmatrix}$$

$$P^s_{PPP}(\omega_1+\omega_2) = \begin{pmatrix} \left(A_x(\omega_1)A^*_z(\omega_2)+A_z(\omega_1)A^*_x(\omega_2)\right)\chi_{xxz} + \left(A_z(\omega_1)A^*_x(\omega_2)+A_x(\omega_1)A^*_z(\omega_2)\right)\chi_{xzx} \\ 0 \\ \left(A_x(\omega_1)A^*_x(\omega_2)\right)\chi_{zxx} + \left(A_z(\omega_1)A^*_z(\omega_2)\right)\chi_{zzz} \end{pmatrix}$$

$$P^s_{PSS}(\omega_1+\omega_2) = \begin{pmatrix} 0 \\ 0 \\ \left(A_y(\omega_1)A^*_y(\omega_2)\right)\chi_{zyy} \end{pmatrix}$$

$$P^s_{SPP}(\omega_1+\omega_2) = P^s_{SSS}(\omega_1+\omega_2) = P^s_{PPS}(\omega_1+\omega_2) = P^s_{PSP}(\omega_1+\omega_2) = 0$$

A similar procedure gives the following table:

Pol. Set	$C_{\infty\upsilon}$	$C_{3\upsilon}$; $\hat{m} \perp \hat{a}$	$C_{3\upsilon}$; $\hat{m} \perp \hat{b}$
SSS		χ_{yyy}	
SSP	χ_{yyz}	χ_{yyz}	χ_{yyz}, χ_{yyx}
SPS	χ_{yzy}	χ_{yzy}	χ_{yzy}, χ_{yxy}
SPP		χ_{yxx}	
PPP	$\chi_{xxz}, \chi_{xzx}, \chi_{zxx}, \chi_{zzz}$	$\chi_{xxz}, \chi_{xzx}, \chi_{zxx}, \chi_{zzz}$	$\chi_{xxz}, \chi_{xzx}, \chi_{zxx}, \chi_{xxx}, \chi_{zzz}$
PPS		χ_{xxy}	
PSP		χ_{xyx}	
PSS	χ_{zyy}	χ_{zyy}	χ_{zyy}, χ_{xyy}

Table 1.2: The non-zero tensor elements of the non-linear second order susceptibility corresponding to different polarization combinations. The yellow shadowed elements are the elements which vanish in TIR at the critical angle.

An interesting advantage of using TIR at critical angle configuration, is that the PPP-polarization combination gives a direct measurement of χ_{zzz} where the rest ($\chi_{xxz}, \chi_{xzx}, \chi_{zxx}$) will vanish. Hence, the SFG signal in the PPP-polarization combination under TIR at critical angle configuration depends exclusively on χ_{zzz}. One can understand this from the TIR geometry. The incident p-polarized light in the yz-plane has two components ($\hat{x}$-component and $\hat{z}$-component). At the interface, the incident and the reflected beams will have the same absolute field strength but with opposite directions for the in-plane components ($\pm\hat{x}$-components). Thus the electric field at the interface is only $//\hat{z}$ and no $\hat{x}$-component, see Figure 1-14. This reduces the number of non-zero elements, exciting PPP SFG signal, to only one tensor element (χ_{zzz}).

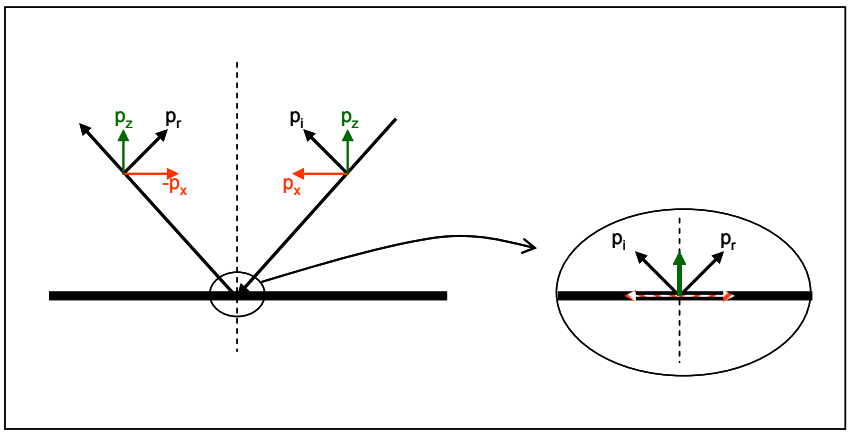

Figure 1-14 A schematic representation that shows the vanishing x-component of the incident p-polarized field in the case of TIR.

1.5.2 Molecular hyperpolarizability tensor ($\beta^s_{\alpha\beta\gamma}$)

As any physical property of the medium, the molecular hyperpolarizability tensors should have certain symmetry group which reflects the structural symmetry of the medium. According to Neumann's principle, "*Symmetry elements of any physical property of a crystal must include all symmetry elements of the point group of the crystal*", the tensor representing any physical property should be invariant with respect to any of the symmetry operations of the considered crystal class. Hence the total number of independent elements can be reduced drastically depending on the symmetry operations of the respective group by determining equal and/or zero elements. This can be expressed mathematically as follows:

$$\left(\hat{i}.S\right)\beta^s_{ijk} : \left(S.\hat{j}\right)\left(S.\hat{k}\right) = \beta^s_{ijk}$$

where S is a second-rank three-dimensional tensor representing the symmetry operation. If we consider, for example, the reflection operator in the ac plane, $S_{R(ac)}$, for the methyl group $C_{3v} : m \perp^r \hat{a}$,

$$S_{R(ac)} = \begin{pmatrix} 1 & 0 & 0 \\ 0 & -1 & 0 \\ 0 & 0 & 1 \end{pmatrix}$$

This leads to the following transformations:

$$\begin{bmatrix} \hat{a} \to \hat{a} \\ \hat{b} \to -\hat{b} \\ \hat{c} \to \hat{c} \end{bmatrix} \Rightarrow \begin{matrix} \left(S.\hat{a}\right) = 1 \\ \left(S.\hat{b}\right) = -1 \\ \left(S.\hat{c}\right) = 1 \end{matrix}$$

Let us check the remaining elements of the 27 mentioned in the previous section,

$$\begin{aligned} \beta^s_{aaa} &= (1)(1)(1)\beta^s_{aaa} \\ \beta^s_{aac} &= (1)(1)(1)\beta^s_{aac} \\ \beta^s_{aab} &= (1)(1)(-1)\beta^s_{aab} = 0 \\ \beta^s_{abc} &= (1)(1)(-1)\beta^s_{abc} = 0 \\ &\vdots \\ &\textit{etc.} \end{aligned}$$

Thirteen elements will vanish due to this single operator.

The most common non-vanishing and/or equal tensor elements, particularly those required in the presented study, are included in Table 1.1, [35 - 40]. The generating matrices of the 32 point groups (Crystal classes) are summarized in appendix 4.

1.5.3 Molecular Orientations

Calculating the molecular orientations of the adsorbed molecules with respect to the surface plays an important role in describing the mechanism of adsorption and helps in understanding the interaction at the interfacial region on the molecular scale. Table 1.1 shows the non vanishing tensor elements as a function of the molecular hyperpolarizability tensors, the amount of species and the Euler angles. Combination of two or more of these relations can exclude all the unknowns but keep one. At this stage, Table 1.2 tells which polarization combination one can measure in the lab to find this unknown parameter. As an example, the ratio $|SSP|/|PPP|$ will represent $|\chi_{yyz}|/|\chi_{zzz}|$ for the $C_{\infty v}$ and C_{3v} which correspond to OH and CH_3-SS vibrations, respectively, in the case of TIR at the critical angle. Figure 1-15 shows the calculated $|\chi_{yyz}|/|\chi_{zzz}|$ ratios for OH-SS and CH_3-SS vibrations as functions of the polar orientation angle of the species' transition dipole moments with respect to the normal of the surface. If the value of $|SSP|/|PPP|$ is obtained experimentally, the corresponding angle of orientation can be determined by Figure 1-15.

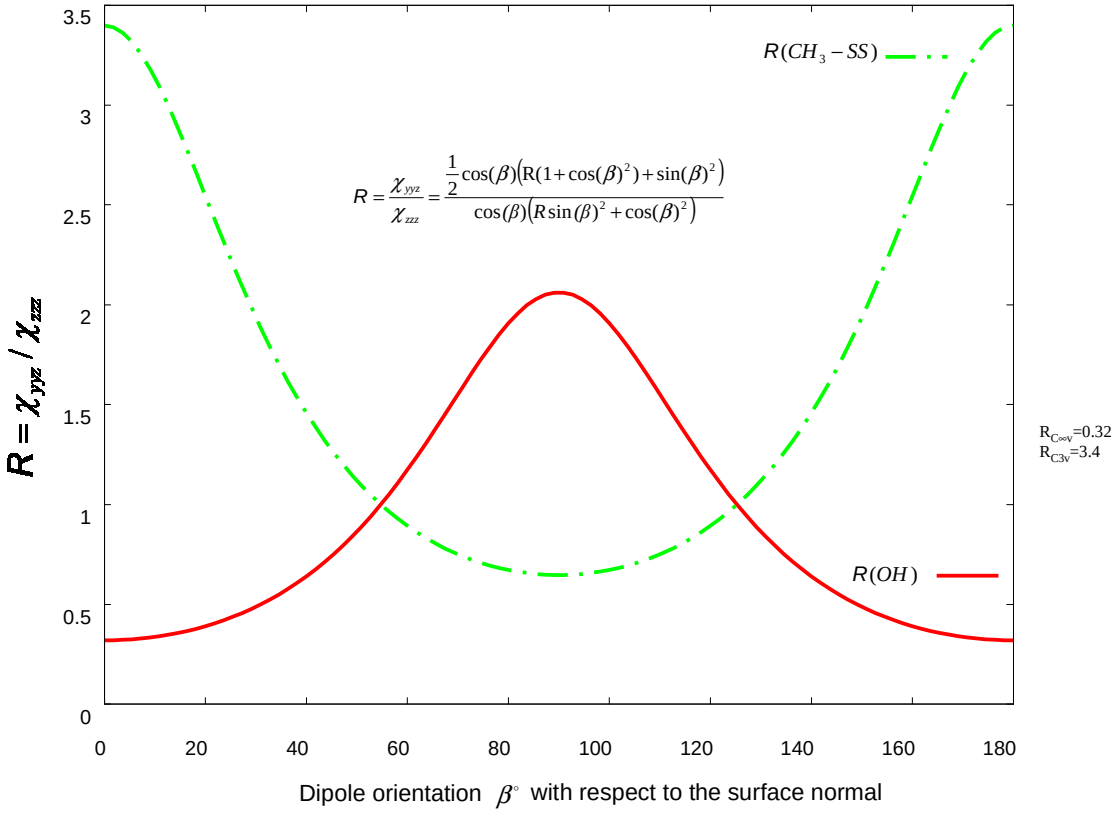

Figure 1-15 Determination of the orientation of transition dipole moments from the $|\chi_{yyz}|/|\chi_{zzz}|$ ratio. One can conclude from this figure that in the OH region PPP can be considered as a scope on the species oriented perpendicular to the interface while SSP is the scope on the species oriented parallel to the interface and vice versa for the CH_3-SS bands

1.6 Resonance function

As mentioned at the beginning of this chapter, the SFG signal is strongly enhanced when the incident infrared photons resonantly excite one or more of the vibrational transitions of adsorbates. These resonance frequencies characterize the physical and chemical properties of the medium. From the classical anharmonic oscillator model, the resonant second order susceptibility at natural frequency ω as a function of the three linear susceptibilities ($\chi_\nu(\omega_{IR}), \chi_\nu(\omega_{Vis})$ and $\chi_\nu(\omega_{SF})$) can be expressed as follows [Appendix 5];

$$\begin{aligned}\chi_\nu^s(\omega_{IR}) &= A_\nu^s\left(\chi(\omega_{IR})\chi(\omega_{Vis})\chi(\omega_{SF})\right) \\ &= \frac{A_\nu^s}{(\omega_\nu^2 - \omega_{IR}^2 - i\Gamma_\nu\omega_{IR})(\omega_\nu^2 - \omega_{Vis}^2 - i\Gamma_\nu\omega_{Vis})(\omega_\nu^2 - \omega_{SF}^2 - i\Gamma_\nu\omega_{SF})}\end{aligned} \tag{1.53}$$

A_ν^s, ω_ν and Γ_ν are the strength, frequency and damping constant of the ν^{th} vibrational mode respectively. The SFG signal will be enhanced once the frequency of one of the fundamental beams or the SFG is tuned to the resonance frequency of the oscillating dipole. The SFG signal is proportional to the effective surface nonlinear susceptibility which can be written as

$$\begin{aligned}\chi^s &= \chi_{NR}^s + \chi_R^s \\ &= \chi_{NR}^s + \sum_\nu \chi_\nu^s\end{aligned} \tag{1.54}$$

where χ_{NR}^s is the non-resonant contribution to the nonlinear susceptibility and χ_R^s is the resonant contribution.

Equation (1.53) is called the "resonance function" and Γ_ν is the transverse relaxation rate, which describes the homogeneous broadening of the vibrational resonance. Γ_ν includes the effect of the vibration dephasing and relaxation on the line width. The signal obtained in the lab is Gaussian broadened due to intrinsic interactions among the large number of molecules involved, thermal effects and spectral width of the incident light. To include the resultant inhomogeneous broadening, Gaussian distribution of the vibrational frequency ω, around the central frequency ϖ, is assumed [41]. Then, the "resonance function" translates into the following form:

$$V_\nu^s(\omega) = \int_{-\infty}^{\infty} \chi_\nu^s(\omega) \frac{1}{\sigma\sqrt{2\pi}} e^{-\frac{(\omega-\varpi)^2}{2\sigma^2}} d\varpi \tag{1.55}$$

where σ and ϖ are the variance due to inhomogeneous broadening and the mean value of the resonance, respectively.

To obtain the parameters (ω_ν, A_ν^s and Γ_ν) of the individual bands, the obtained experimental results are fitted to the resonance function as will be described in the data fitting subsection 2.6.3

1.7 Adsorption of Organic Compounds to Solid Minerals

The adsorption process of organic compounds from the gas and liquid phases to solid mineral, attracted a lot of interest due to its importance of understanding the migration of fatty organic compounds, "Humic Substances", in the environment, [42]. Humic acids are one of the major components of humic substances (or Natural Organic Matter (NOM)) which are dark brown and major constituents of soil organic matter humus that contributes to the chemical and physical quality of soil and are also precursors of some fossil fuels. The influence of humic acids on the migration behaviour of radioactive and non-radioactive substances in nature has become a point of interest. Environmental issues require a good understanding of the interaction of these materials with natural clay minerals. Sapphire (Al_2O_3) is a model for natural clay minerals and analogous iron phases. We are interested in the interaction of the functional species with humic acids and radionuclides. In this work, the interaction of an important constituent of humic acids with definite cuts of the sapphire surface shall be investigated systematically.

The adsorption of piperidine vapour on hydrated alumina indicated that the piperidine is protonated by the surface hydroxyl groups upon adsorption (Allen et al. 2004) [43]. Extensive work on adsorption of alcohols and carboxylic acids on alumina, silica, titanium oxides, and iron oxides was performed [43 - 54].

1.8 Sapphire: α-Alumina (α-Al_2O_3)

1.8.1 Crystal structure of sapphire

α-Al_2O_3, (sometimes called Corundum), is a common inorganic constituent of soil. It transforms under surface conditions (i.e. in contact with water or other liquids and also under temperature changes) to secondary minerals (e.g. Koalinite, gibbsite, zoisite…etc), [55 , 56]. The bulk of α-Al_2O_3 is composed of alternating O and Al planes perpendicular to the *c*-axes (i.e. parallel to the 001 planes), Figure 1-16 (b,c,d). The unit-cell of α-Al_2O_3 is rhombohedral and belongs to the $R\bar{3}c$ space group, Figure 1-16(a). The Al atoms are arranged hexagonally in each layer, Figure 1-16 (e). In each Al layer the octahedrally coordinated Al atoms occupy 2/3 of the available octahedrons, Figure 1-16 (c). Figure 1-16 (c) shows that the vacant octahedral sites change position from one layer to the next but they are repetitive each three layers. This means that the Al ions arrange themselves in one of three hexagonal networks of

different vacant positions, from layer to layer. Actually, inspection of Figure 1-16(c) shows out of plane atomic displacements in each Al layer (// to 001) which form two separated sublayers. This is due to the electrostatic repulsion arising from the face sharing of Al octahedrons in adjacent layers where there are always one Al ion at one side and one vacancy at the other side (up or down) for each Al ion in the same vertical plane (// to 110 plane).

1.8.2 Propagation of Light in Sapphire Crystal

The ***refractive index***, ***n***, of the medium is determined by the mobility of charges vibrating in the medium under the influence of alternating electric field ***E,*** which is a function of the atomic and electronic structure of the material. In ***anisotropic media*** the response of these charges is different for different directions. The variation of ***n*** with direction in a crystal is represented 3 dimensionally by the so called "***Optical Indicatrix***", Figure 1-17. The radius, ***r***, of the optical indicatrix at any polar angle is the refractive index measured with ***E*** // ***r***. There are three types of the optical indicatrix, (*isotropic, uniaxial, biaxial*), generated from the seven crystal symmetry systems, [Appendix 8].

Sapphire crystal is a uniaxial crystal ($n_a = n_b \neq n_c$) which has two ***Permitted Vibration Directions*** (PVD) of refractive indices $\boldsymbol{n_c}$ and $\boldsymbol{n_a}$ along the long axis, ***c***, and the short axes, ***a***, respectively. These are the extraordinary and ordinary axes respectively. Thus it is called birefringent crystal of birefringence $\Delta n = n_c - n_a$. To avoid any influence of the birefringencity of the sapphire crystal on beam propagation and polarization, we have to restrict ourselves to certain crystal cuts (001 and 110 in this study) and geometries for the incident beams such that the light beam can pass through the crystal without experiencing more than one value of n even if it is not equal to one of the principle indices $\boldsymbol{n_c}$ and $\boldsymbol{n_b}$. Figure 1-18 shows that the cross section of the indicatrix at the hypotenuse surface is circular, however it is elliptical at the entrance face. The S-polarized light will suffer $\boldsymbol{n_a}$ and the P-polarized light will suffer $\boldsymbol{n_a} < \boldsymbol{n_x} < \boldsymbol{n_c}$ which is constant along the path of propagation inside the crystal. The generated sum frequency light with S- or P-polarization will travel toward the exit face suffering also from one of these two indices ($\boldsymbol{n_a}$ or $\boldsymbol{n_x}$ respectively). From the geometry and the equation of ellipse, Figure 1-18(b), $\boldsymbol{n_x}$ is related to $\boldsymbol{n_a}$ and $\boldsymbol{n_c}$ by the following relation:

$$\frac{1}{n_x^2} = \frac{\sin^2\theta}{n_c^2} + \frac{\cos^2\theta}{n_a^2}$$

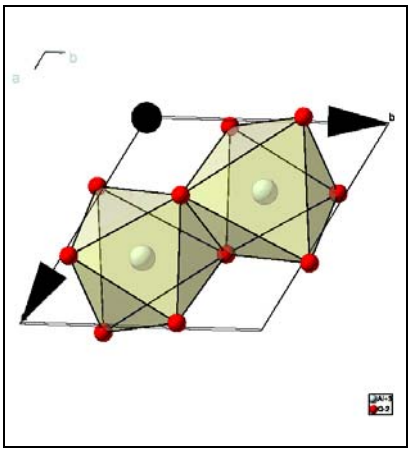

(a) Top view (001) of the rhombohedral unit cell and two of the included octahedrons

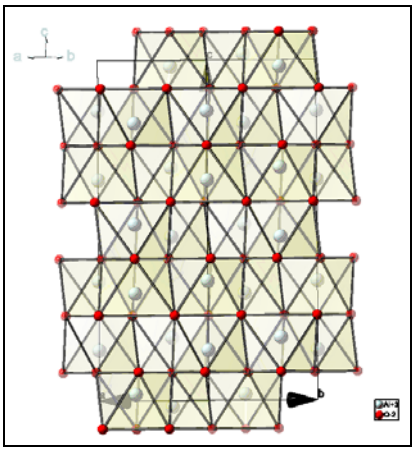

(b) Top view of 110 cut (2 layers of Al planes). Side view of 001-planes (// to the upper edge)

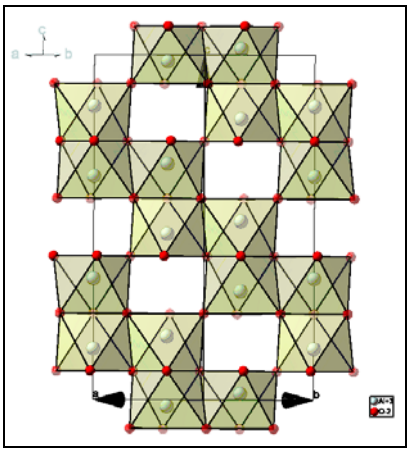

(c) Top view of 110 cut (1 layer of Al plane)

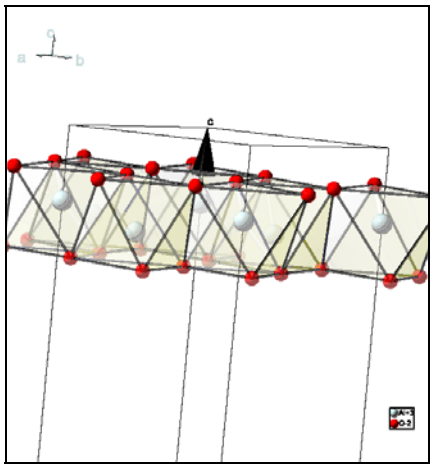

(d) Side View of the 001 plane (Semi-horizontal view of slice of 3 planes)

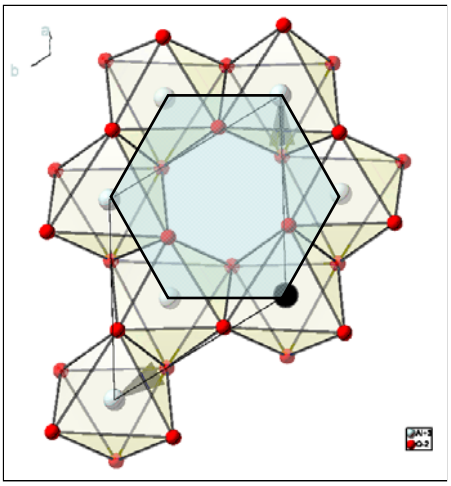

(e) Top view of the 001 cut

Figure 1.16 α-Al_2O_3 crystal bulk and surface structure

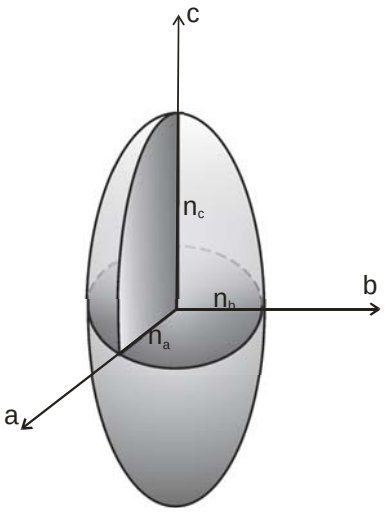

Figure 1.17 The optical Indicatrix which represent the variation of refractive index with direction in a crystal.

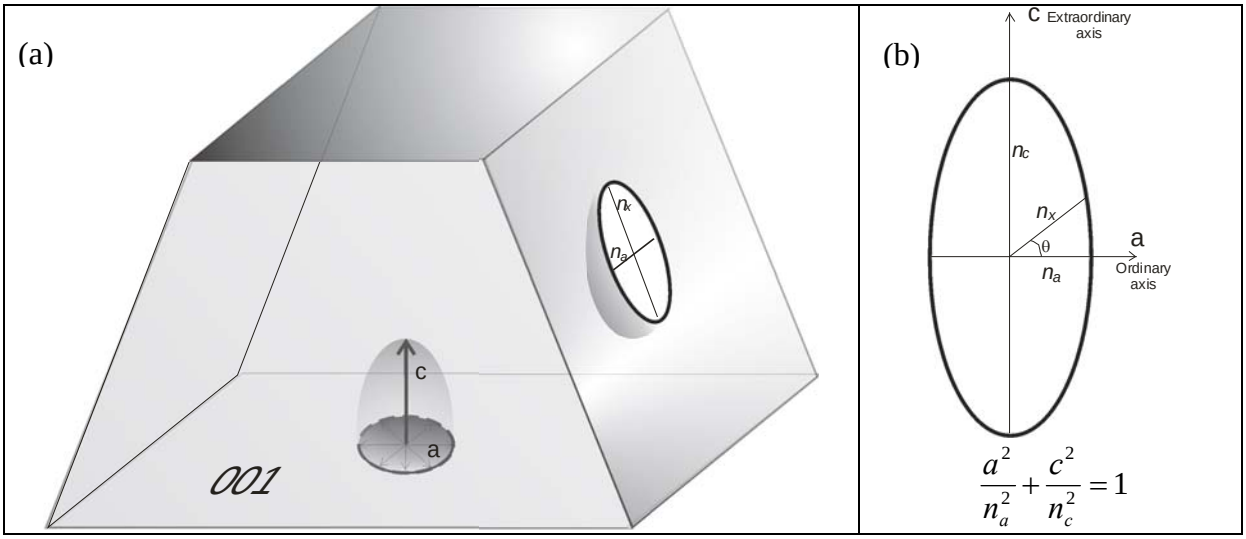

Figure 1.18 a) Different cross sections of the indicatrix for the uniaxial sapphire crystal at different crystallographic faces ($\perp$ to the plane of incidence). In our SF experiments the incident light hits the face at the right hand side. b) The elliptic cross section of the indicatrix // to the plane of incidence.

CHAPTER 2

EXPERIMENT, MATERIALS AND DATA ANALYSIS

2. Experiment, Materials and Data Analysis

2. Experiment, Materials and Data Analysis

2.1 The Laser System

The laser system used in this work is a commercial laser system delivered by ***Euroscan Instruments***[1]. It is composed of a pulsed Nd:YAG laser system generating the fundamental and second harmonic beams and an Optical Parametric Oscillator (OPO) generating the mid-infrared radiation required to excite molecular vibrations. The laser system generates pulse trains of about 160 pulses per train at 25 Hz repetition rate and ~12ps pulse duration per pulse. The spectral resolution is about $\Delta\lambda$=2-3 cm^{-1} for the IR generated by the Optical Parametric Oscillator (OPO). In Figure 2-1, the four main stages of the laser system are sketched as follows:

(1) Nd:YAG mode-locked Oscillator using an all-solid-state system design,

(2) Nd:YAG Amplifier,

(3) Fundamental beam splitting, spatial filtering and frequency doubling,

(4) Narrow band tunable Mid-IR Optical Parametric Oscillator (OPO) with two different operating wavelength ranges depending on the nonlinear crystal used ($LiNbO_3$: 2.5-4μm and $AgGaS_2$: 4-10μm)

In the first stage, the oscillator, a mode-locked pulse train of ~210 successive 12ps pulses is generated at a wavelength of 1024nm. The Pulse Repetition Rate of these pulse trains is PRR=25Hz (more details about this laser cavity are published in [57]). This pulse train is amplified in the second stage, the amplifier. Before the amplifier stage, the pulse is modulated by an Acousto-optical Modulator (AOM) to cut off the first ~50 pulses within a ~500ns interval, which have high energy but show a pulse duration in the ns regime. The remaining ~160 pulses (~1.6μs total duration) with a pulse duration of ~12ps are then allowed to pass the AOM undisturbed . The AOM is triggered from inside the oscillator cavity by a signal reflected from a GaAs plate to a photodiode. After the amplifier stage, the pulse train arrives at the third stage where the output of the amplifier is divided into two parts using a beam splitter: 20% for generating the second harmonic light (532nm, “green”) using a BBO (Bariumborate, β-$BaBO_3$) crystal and 80% for pumping the fourth stage, which generates the

[1] www.euroscan.be

mid IR radiation. Both beams undergo spatial cleaning using a spatial filter made of thin plates of aluminium and placed at the focus of telescopes 2 and 4, respectively. The fourth stage, the OPO, generates the tunable IR from the fundamental light using DFG under phase matching condition in the nonlinear optical crystal (NLC) during its computer controlled rotation inside the OPO cavity. The direction of the generated light is defined by the phase matching conditions within the NLC. The DFG process generates two frequencies from the fundamental frequency (ω_{fund}):

The *signal* (ω_{signal}) which will be captured inside the OPO cavity, resonating between the two end mirrors (M15 and M16)

The *idler* ($\omega_{idler} = \omega_{fund} - \omega_{signal}$) which will be coupled out of the cavity using two computer controlled counter rotating mirrors (M13 and M14).

The synchronization between the rotational motions of the NLC and the two mirrors is done through a complex calibration process. Further, the optical length of the OPO cavity should be optimized such that the generated captured pulses are synchronized with the incoming fundamental pulses. Due to this synchronization between the OPO signal and the OPO pump (the incoming fundamental), the DFG process is amplified selectively for the chosen wavelength. Since the frequency of the OPO *signal* ($\omega_{signal} = \omega_{fund} - \omega_{idler}$) is changing during the scan, the geometrical length of the OPO should be optimized during the scan. In the present system, this optimization used to be achieved by changing the OPO cavity length manually using a manual translation micro-stage placed under M16. Since this optimization is done manually, the spectral scan used to be divided into three or four parts each of which has the OPO cavity length optimized at the central wavelength of the selected part. Also the calibration of the rotational motions of the moving optical components inside the OPO cavity should be divided into two or three domains for the selected NLC. Each of these domains has its own calibration file which should be uploaded to the controller software to enable the measurement in this domain. Anyway, I have changed this tedious experimental procedure recently as will be discussed in the section of *System Development* (section 2.7).

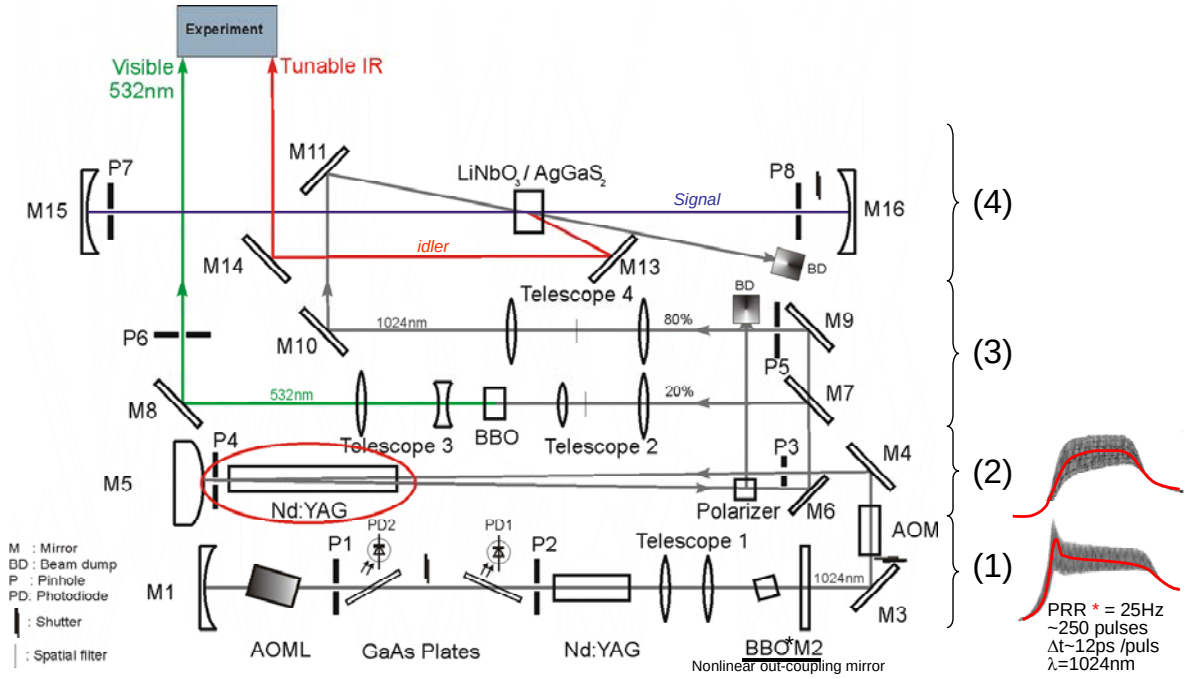

Figure 2.1 Schematic representation of the used Laser system

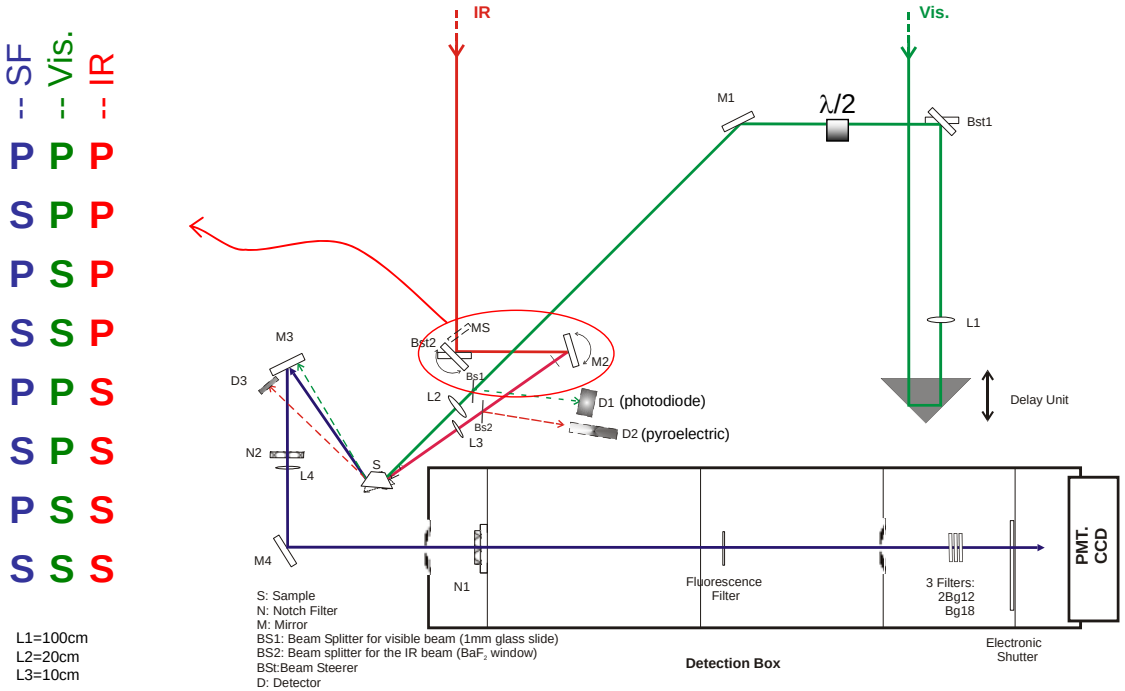

Figure 2.2 Schematic representation of the experimental setup

2.2 The SFG and IR-TIR setup

Figure 2-2 shows the setup which was used in both SFG and reflectivity measurements. The experiments were carried out in Total Internal Reflection (TIR) configuration from the sapphire side to overcome the strong absorption of the used liquids in the selected range of wavelengths (2.5 to 4μm). This configuration benefits also from the intense fields at the interface. In addition the sample was adjusted to the TIR at the critical angle of the green beam to reduce the number of nonlinear susceptibility tensor elements (section 1.5) contributing to the signal. Thus, the determination of molecular orientations, as discussed in Chapter 1, became reliable. For generation of SFG, the tunable IR, generated by the OPO, and the green beam were spatially and temporally overlapped at the interface. The "Delay Unit" was used to adjust the temporal delay, while the lens L3 was mounted on a 3D holder to adjust the spatial overlap. The sample holder was mounted on a 6-degrees-of-freedom goniometer to allow fine tuning of the required orientation of the sample with respect to the incident beams including the possibility to find the critical angle. During the experiments the prism-like sample was pressed against a Teflon flow cell (the measuring cell) with the hypotenuse facing the wall of the cell where a hole of 4mm diameter had been drilled to allow contact between sample surface and the medium contained in the cell. This configuration was kept in place using a home-built cell holder.

The height of the incident beams was changed from the laser output level (50mm) to the sample level (150mm) using two beam steerers Bst.1 and Bst.2 in the beam paths of the Visible and IR lights, respectively. The polarization of the visible beam was adjusted using a half wave plate in the beam path. In the original setup, the IR could be used in P-polarization only. However, as shown in Figure 2-2 an additional mirror (MS) was mounted recently and the upper mirror of the beam steerer Bst2 was mounted on a rotating stage to enable the change of the polarization of the IR beam to S-polarization. To this end, mirror M2 had to be placed on a rotating mount to readjust the beam direction. With this small modification of the set-up, all the eight possible polarization combinations, as shown in Figure 2-2, became possible. Before, only four polarization combinations had been applicable.

During the experiment, the intensities of the incident beams were monitored using a reflection of the visible beam from a glass plate to a UV-Visible Photo-receiver (D1) from NEW FOCUS and a reflection of the IR beam from a BaF_2 plate to a pyroelectric detector (D2) from SCIENTECH.

The SFG signal was generated in the region of the interface where the inversion symmetry is broken. This signal of frequency $\omega_{SF} = \omega_{Vis} + \omega_{IR}$ was collected by the optics placed after the sample and detected by the Photomultiplier Tube (PMT). The SFG was separated from stray light using a set of optical filters, providing a narrow window of transmission for the generated SFG light only. A collimating lens (L4) was used to collimate the generated beam onto the PMT. The signal detected by the PMT is then acquired by an electronic system connected to a PC and stored in terms of intensity values of visible, IR, SFG, and their respective backgrounds.

The OPO and the experimental set-up, excluding the detection box and the PMT, were placed in an argon box to avoid the absorption of the IR in the range from 2.4μm to 3μm by water vapor. The fundamental and the second harmonic of the Nd:YAG laser were guided through the wall of the argon box by means of 1mm glass windows.

In both, the SFG and the linear TIR experiments, the sample was placed in the same geometry with respect to the incident and emitted beams. This geometry is shown in Figure 1-5. In the SFG experiments, the incident angle of the visible (the green) beam from air to the entrance side of prism-like sample was chosen to satisfy the critical angle of TIR at the sapphire/contact-medium interface. The incident IR beam was chosen such to lie at arbitrary angle close to the visible one (10˚ in this study). The generated sum frequency light was collected as described above. In the linear reflectivity experiments, the visible light was blocked and the IR light was allowed to incident on the entrance side of the prism-like sample with a specific angle for each polarization (S or P) and each contact-medium. The respective angles were calculated beforehand for each contact-medium and each polarization, to satisfy one condition: The two contour lines (described in section 1.4.2) which correspond to the two measured reflectivities (R_p and R_s) should be as perpendicular as possible to each other. It was found that if the intersecting contour lines are semi-parallel to each other, the sensitivity of the position of intersection point to the fluctuations in the reflected signal will be high. On the other hand, the intersection point is less sensitive to the fluctuations in the reflectivity signal as long as the angle between the contour lines approaches 90˚. The reflected light was collected at a position right after the sample using a piezo detector (D3)

2.3 Liquid pump and measuring cell

The liquids and vapours studied in this work were delivered to the measuring cell using the cycle shown in Figure 2-3. The compounds were prepared or mixed in the reservoir R1 and then pumped into the measuring cell R2. During the experiments the prism like samples were pressed against a PTFE ("teflon") flow cell with the hypotenuse of the prism facing the wall of the cell where it had a hole of 4mm diameter to allow access to the cell medium from the prism side. This configuration was kept in place using a home-built cell holder. Changing the concentrations, measuring the pH and purging inert gas (Argon) into the solution were done in an external Teflon reservoir R1 using a specially designed cap constructed at NILES[1] for this purpose. This reservoir was connected to the measuring cell through Tygon MHLL[2] tubes using a peristaltic pump. Purging inert gas optionally was used in the water/sapphire interface experiments to get rid from the CO_2 content, particularly at high pHs. The entire experiment could therefore be carried out in-situ. The saturated vapours could be pumped into the measurement cell by inversing the cycling direction shown in Figure 2-3 while the large reservoir R1 was filled with the liquid of the wanted vapour.

[1] NILES: National Institute of Laser Enhanced Science -Egypt
[2] Ismatec SA, Switzerland (www.ismatec.com)

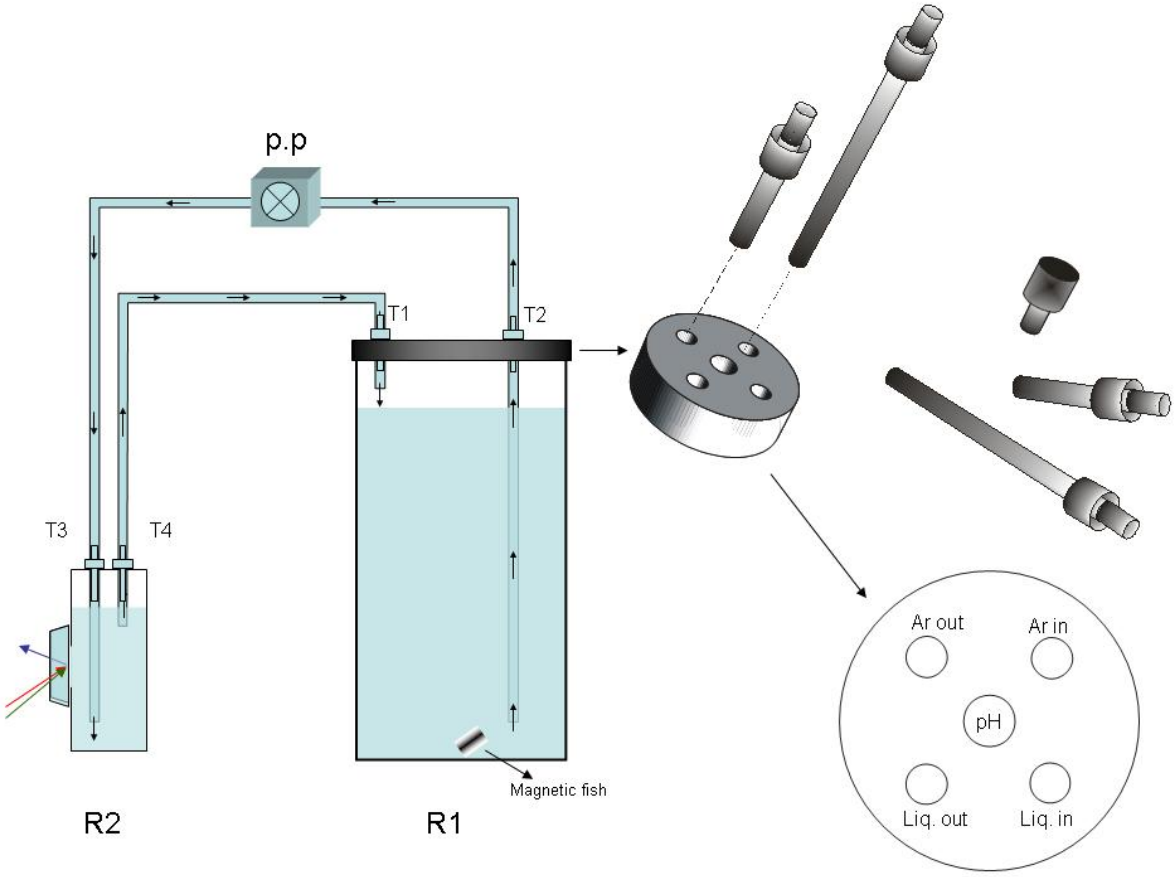

Figure 2.3 The liquid cycle: the peristaltic pump (p.p.), the exchanging reservoir (R1), the home made cover and the measuring cell (R2).

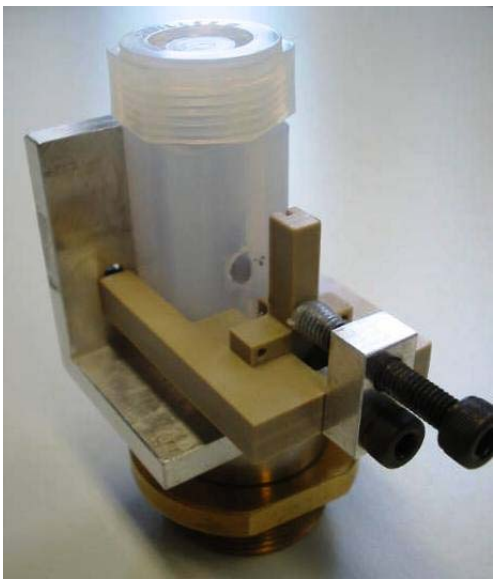

Figure 2.4 The home made sample holder and the measuring cell (R2)

2.4 The Chemicals

The chemicals used in this work either for cleaning or for investigation are listed in Table 2.1. The chemicals were used as they were without any purification or treatment.

Chemicals	Formula chemical data	Purity %	Source
Propionic acid p.a.	**CH_3CH_2COOH 1L=0.993 kg M=74.08 g/mol**	**99.8**	**Fluka Germany**
Methanol p.a.	**CH_3OH 1L=0.79 kg M=32.04 g/mol**	**≥ 99.9 Water content ≤ 0.05**	**Merck KGaA, Darmstadt, Germany www.merck.de**
Ethanol p.a.	**$CH_3(CH_2)OH$ 1L=0.79 kg M=46.07 g/mol**	**≥ 99.8 Water content ≤0.0001**	**Carl Roth GmbH Schoemperlenstr. 3-5 76185 Karlsruhe**
1-Propanol p.a.	**$CH_3(CH_2)_2OH$ 1L=0.80 kg M=60.10 g/mol**	**≥ 99.8 Water content ≤ 0.02**	**Merck KGaA, Darmstadt, Germany www.merck.de**
1-Butanol for spec.	**$CH_3(CH_2)_3OH$ 1L=0.81 kg M=74.12 g/mol**	**≥ 99.9 Water content ≤ 0.05**	**Merck KGaA, Darmstadt, Germany www.merck.de**
Sulfuric acid p.a.	**H_2SO_4 1L=1.84 kg M=98.08 g/mol**	**95-79**	**Merck KGaA, Darmstadt, Germany www.merck.de**
Chloroform p.a.	**$CHCl_3$ 1L=1.48 kg M= 119.38 g/mol**	**99-99.4**	**Merck KGaA, Darmstadt, Germany www.merck.de**
Milli-Q water		**resistivity > 18.2MΩcm**	**Milli-Q Synthesis system from Millipore GmbH**

Table 2.1 List of the chemical used in this work

2.5 Sample and Cleaning

The prism-like single crystal sapphire samples used in these experiments were 001 or 110 cuts at the hypotenuse face (10x10mm^2). The prisms used were of isosceles triangle side cuts of either 60° or 45°, respectively.

The samples were used as received from the manufacturer[1] without any further annealing or polishing. For cleaning, each sample was put in chloroform or concentrated H_2SO_4 for ~30min. In the case of concentrated H_2SO_4, X-ray Photoelectron Spectroscopy (XPS) measurements showed that the surface was sulfated. The sulfated surface was allowed to equilibrate in sodium hydroxide solutions (of pH=12) for 12 to 16hr. The cleaning with H_2SO_4 gave better results in removing the hydrocarbon contaminants on the surface. However, the surface is expected to be affected due to the dissolution of sapphire at pH12 after being in contact for long time. The effect of H_2SO_4 on the surface during the 30min is also worth of consideration. After the chloroform (or H_2SO_4) stage the sample was immersed in methanol for ~30min. Finally the samples were rinsed extensively with Milli-Q water (resistivity > 18.2MΩcm). The XPS results from the best two cleaning procedures are summarized in Table 2.2. UV cleaning was used only in the contact angle measurement experiments which were carried out late in this work. UVO-cleaner (Model 342-220) from JELIGHT[2] COMPANY INC was used for this purpose. UV cleaning results were best of all in removing the hydrocarbons adsorbed to the surface without the need to deal with aggressive acids or bases, especially pH12 which requires high precautions to avoid its greediness to adsorb CO_2 from air. It was sufficient to clean the sample with methanol to remove the thick indirectly bonded contaminants on the surface and then remove the directly bonded layer using the UV light with Ozone. Some results of the contact angle are tabulated in Table 3.4.

Element	**Al**	**O**	**C**	**F**	**Fe**	**Ca**	**S**	**N**	**Cu**
Atomic concentration % relative error +/- (10-20)%	**H_2SO_4 (30min)→ pH12 (12hr) → methanol (30min) → Milli-Q water**								
	39.9	**57.8**	**1.5**	**0.4**	**~0,02**	**0.1**	**0.3**		
	Methanol → UV-Ozone → Methanol → Milli-Q water								
	42.1	**55.0**	**1.7**	**0.9**	**0.3**				

Table 2.2 XPS results for two different cleaning procedure

[1] V. Kyburz AG, Safnern, Switzerland (www.kyburz-sapphire.ch)
[2] JELIGHT COMPANY, INC (jci12@jelight.com)

Both cleaning procedures, shown in Table 2.2, gave a ratio of Al:O equals to ~ 40:60 within the error tolerance (10-20 %). This is the expected ratio for sapphire 001 surface. Cleaning with annealing might be another option, but it was excluded because of potential silica contaminants from the used oven [58].

The most prominent contaminant was carbon (XPS is not capable to detect hydrogen). The small amount of carbon may come from adsorbed hydrocarbons from air during transportation to the XPS system. These hydrocarbons did not show their fingerprints in the CH vibrational region in the spectra collected in the water experiments due their random orientation on surface. Other strongly adsorbed hydrocarbons (from the fabrication process, packaging and transportation by the manufacturer) were detected in the water spectra before sample cleaning. However, as mentioned in the beginning of this section, using H_2SO_4 instead of chloroform as first step in the cleaning procedure was successful in removing them. Tiny amounts of F, Fe, Ca and S were observed in the XPS measurements. These contaminants are expected to originate from the cleaning chemicals themselves and/or the handling and transportation of the samples. Fluorine is expected to come from the Teflon ware which was used for cleaning and storing the samples. However, these contaminants have no effect on the intrinsic SFG particularly in the range of wavelengths used in this study. The expected influence of these contaminants is a slight change in the surface charge and hence the adsorption mechanism. This influence was found to be within the acceptable experimental tolerance.

2.6 Data Acquisition and Analysis

The SFG data obtained from the system used in this work were collected with data acquisition electronics connected to a PC where the data sets were stored for subsequent analysis.

2.6.1 Data acquisition

The Labview software[1] was used for data acquisition. The Labview program code which was used to control the experiment and to collect the data was provided by the manufacturer of the laser system. The software drives the experiment by rotating the NLC, mirror M13 and mirror M14 stepwise, thereby referring to a calibration file, which contains the information about the relative motions of these three components in the OPO cavity. Simultaneously, the software records the signals from the SFG, IR and visible beams through three independent channels as a function of the IR wavenumber and measures the background frequently every given number of scan steps (usually 25 steps in the presented work). The steps of the scanned wavenumber range can be defined by the user (-2 or -4 wavenumbers/step in this work). After each point of measurement, the rotating components rest and the detection electronics start to collect data, from the three channels, at a sampling rate of 10MHz integrated over predefined time gates. The time gates are set independently for the three detectors to fit their individual response times. The mean value of the integrated signals over a defined number of pulses for each channel (64 pulse trains ≡ 2.5sec, in this work) is then sent to the computer as one measured point. The three measured points from the three channels are stored as one row of the complete data set. Then, the program rotates the optics again to the next step and so on.

The background generated from the visible light is measured when the IR is cut by blocking the OPO cavity using the shutter in front of M16 inside the OPO cavity. At this state the backgrounds on the IR-detector-channel and the PMT-channel are measured. The background on the visible-detector-channel is measured by cutting the fundamental light using the shutter between the oscillator and the amplifier (after M3).

[1] www.labview-service.de

2.6.2 Data analysis

The data set is stored in the computer in the form of two tables. The first table includes four columns: wavenumber, SFG intensity, IR intensity and visible intensity. The second table has the same columns but for the background measurements. The data sets are treated as follows:

1. The background is averaged and subtracted from the obtained signal for each channel.
2. The SFG intensity is corrected to the spectral absorption of the used filters and the polarization analyser in the detection path.
3. The SFG intensity is normalized to the incident intensities, I(SFG)/I(IR)/I(Vis).
4. If the detectors are used at different amplifications from one experiment to the other, the intensities of the three channels are divided by the amplification factors. This is necessary if the results from different experiments are compared.
5. The data are then converted to field strengths ($E = \sqrt{I}$)
6. The field is then corrected by the Geometry Factors described in section (1.4.1).

$$Geo_{IJK} = \frac{\omega_{SF}\,\sec(g')}{n_m(\omega_{SF})}\left|\mathbf{e}_i^{SF} \bullet \mathbf{e}_j^{Vis} \bullet \mathbf{e}_k^{IR}\right|$$

After step #6, the data represents the second order nonlinear susceptibility:

$$\frac{E^{\omega_{SF}}}{Geo_{IJK}\left|E_{in}^{Vis}\right|\left|E_{in}^{IR}\right|} \Rightarrow \chi^s$$

7. This data are then fitted to equation (1.54) using the Gnuplot[1] software. Gnuplot is a text mode based fitting program, which has the advantage of the possibility to define specifically required fitting functions. Also, it deals with complex numbers. This software has been used in fitting both the SFG and the IR-TIR results.

[1] www.gnuplot.info

It is worth to mention here that the step of correcting the obtained SFG data for the geometry factors is obligatory to allow the comparison of spectra from different media and even spectra from the same medium but obtained with different polarization combinations. Also, since the geometry factors are dependent on the optical properties of the media through which the light travels, it is important to consider the effect of temperature change on the optical constants. For example, if the optical constants of the contact medium were taken from the literature, the SFG experiment should be carried out in the way that the temperature at the interface is the same as that of the experiment to determine these optical constants. In this work, this problem was avoided by determining the optical constants of the used media in independent reflectivity experiments under the same conditions as those of the SFG experiments and with the same TIR configuration.

In the linear reflectivity experiments, the reflected light from the interface was normalized to the incident light. Two full spectral scans, R_p and R_s, were carried (one full scan for each polarization). The optical constants were calculated in two steps: the first step was to determine one set of optical constants, (n_2, k_2), each 50cm^{-1} using the graphical method described in section (1.4.2). Afterwards, the graphically obtained sets of optical constants were fed into a home-programmed numerical-solution-code [59] as starting parameters. The numerical solution code required these starting values to calculate the optical constants over the full spectral range with the given wavenumber steps (2cm^{-1} in this study).

2.6.3 Data fitting

The data fitting is the process of deconvolution of the obtained spectra into individual resonance bands each of which describing a certain physical or chemical property. In SFG, the resonance function equation (1.53) is a complex function (i.e. it has real and imaginary parts), which contains information about the relative phases of the individual bands. In this case, the fitting code (program) should be able to deal with complex numbers (i.e. it should understand the $i = \sqrt{-1}$). Therefore, the Gnuplot [see Appendix 7j] software, which is able to deal with complex numbers, was used in this work to extract information not only on the relative magnitudes of the resonances, but also about the phase of the signals. Considering the effect of phases gives more realistic results and provides information about the relative orientations of different species. To explain the advantage of phase sensitive analysis, let us assume a simple form of equation (1.53), apply it to two hypothetical resonance modes lying

next to each other within a short spectral range, assume a zero non–resonant background $\chi^s_{NR} = 0$ and ignore the resonances in the SFG and fundamental-visible wavelength range (weak contribution) . Equations (1.53) and (1.54) can then be simplified to:

$$\chi^s_1(\omega_{IR}) = \frac{A^s_1}{(\omega^2_1 - \omega^2_{IR} - i\Gamma_1\omega_{IR})}$$
$$\chi^s_2(\omega_{IR}) = \frac{A^s_2}{(\omega^2_2 - \omega^2_{IR} - i\Gamma_2\omega_{IR})}$$
$$\chi^s_T(\omega_{IR}) = \chi^s_1(\omega_{IR}) + \chi^s_2(\omega_{IR})$$

Figure 2-5 (a) and (b) show a simulation of SFG spectra using the above equations with two different resonance modes (one is a broad band centred at 3100cm^{-1} and the other is a relatively narrow band centred at 2950cm^{-1}) under the following conditions: (a) both bands have the same phase $\varphi_1 = \varphi_2 = 0$ and (b) they have relative opposite phases $\varphi_1 = 0$, $\varphi_2 = \pi$ (180° out of phase). The difference in the resultant SFG signals is visible. In-phase peaks resulted in SFG curve of a small tail on the lower wavenumber side of the narrow peak, while out-of-phase peaks resulted in SFG curve of intensity lower than that of the original peak on the lower wavenumber side of narrow peak. In addition, the valley between two peaks is shallower in the case of out-of-phase peaks than that of in-phase peaks. It is clear now that the shape of the SFG spectrum can be strongly affected by the phase angle between different peaks. To see more cases, one should change the parameters and the number of peaks, plot the resultant SFG and inspect the differences. Actually and practically, this is a good recommendation to train the eyes on recognising the differences in the SFG curves from the first look at the collected spectra before starting the fitting. This will help in estimating the starting fitting parameters. Finally, sometimes, for better understanding of the contributions of the individual resonances to the SFG spectra, the real and imaginary parts are plotted for the individual peaks, Figure 2-5 (c), (d), (e) and (f). In this case the imaginary parts (corresponding to the absorption resonances) of different modes can be inspected and the signs can be compared directly.

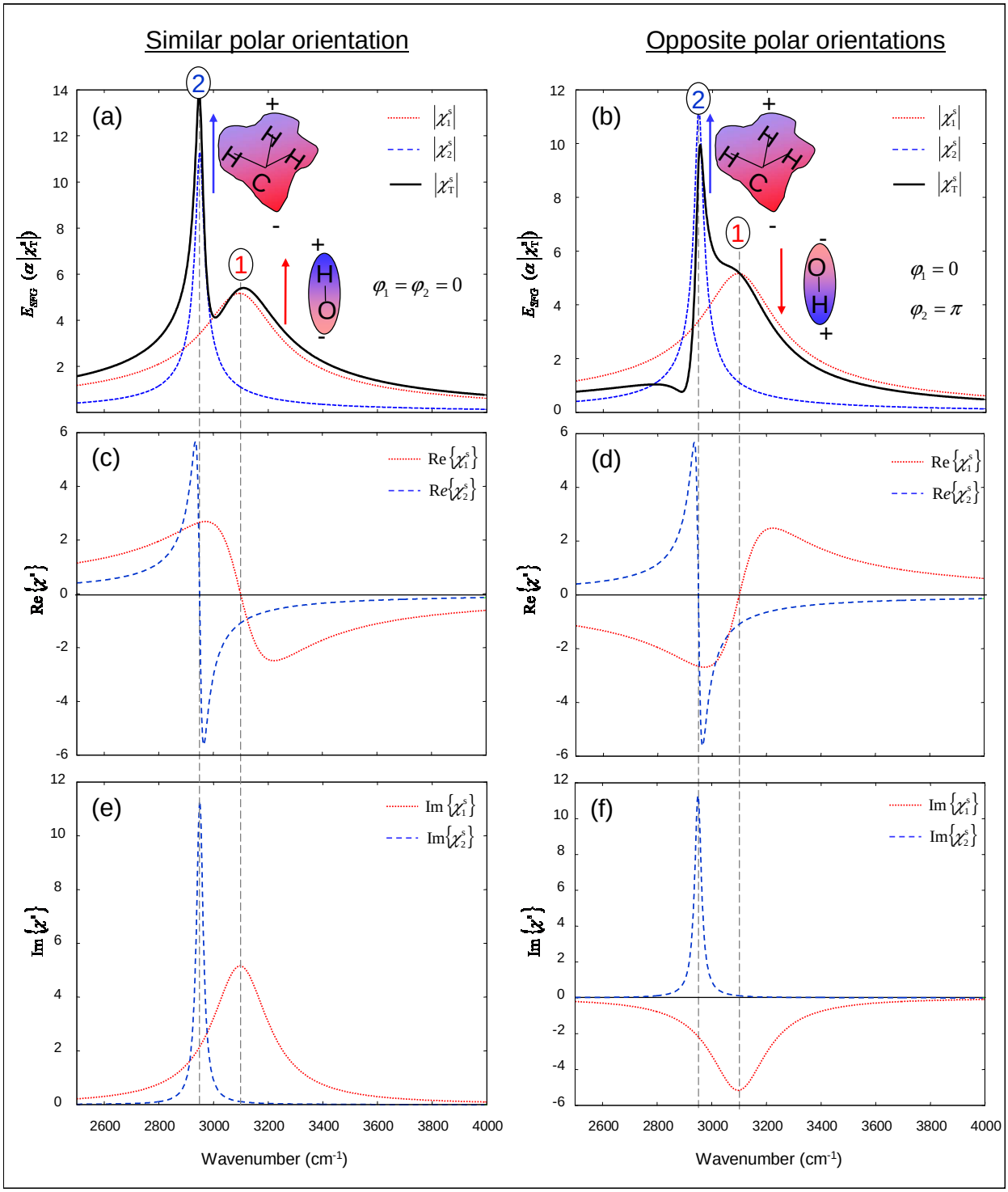

Figure 2-5 (a) and (b): A simulation of SFG spectra resulting from the convolution of two different resonance modes (one is a broadband, $\Gamma_1 = 250$, of amplitude A_1=4 centred at 3100cm^{-1} and the other is a relatively narrow band, $\Gamma_2 = 30$, of amplitude A_2=1 centred at lower wavenumber= 2950cm^{-1}) for two cases: (a) both have the same phase $\varphi_1 = \varphi_2 = 0$ (b) they have relative opposite phases $\varphi_1 = 0$, $\varphi_2 = \pi$ (180° out of phase). (c) and (d): comparisons of the real parts of $\chi^s(\omega_{IR})$ for the two cases (a) and (b), respectively. (e) and (f): comparisons of the imaginary parts of $\chi^s(\omega_{IR})$ for the two cases (a) and (b), respectively. ($\chi^s_{NR} = 0$ in all cases)

2.7 System Development

Although marginal compared to the surface science and spectroscopy discussed in this thesis, I will demonstrate in this section the work I did in improving the laser and the spectroscopic system itself. Before starting the experimental work and processing the data, such complex spectroscopic techniques, which are based on nonlinear phenomena, should be well understood. It is highly recommended to study the technical parameters of the system and test the reproducibility of the results obtained. I will discuss in the following sections some of the technical difficulties of this laser system and the experimental setup and explain the precautions taken to overcome them. I will also give some recommendations on the best way of carrying out the experiment and how to avoid collecting bad data. Some parts of the laser system and the OPO had to be improved to accomplish better operation of the laser, facilitate the experimental work, and hence achieve higher reliability of the experimental data.

2.7.1 Pointing stability

The two most annoying phenomena that occurred with this Laser system were a kind of ***seasonal*** instability and the low signal-to-noise ratio of the SFG signal. Figure 2-6 shows typical SFG spectra of the methanol/sapphire interface. Figure 2-6a exemplifies the typical spectrum quality used to be obtained by this system before the modifications were implemented. It could be noticed that the quality of the spectra obtained varied from time to time. My preliminary observations on this phenomenon indicated that the fluctuations of the spectra might be due to variations in the atmospheric conditions (temperature, relative humidity, and air flow) in the laboratory. In fact, a study on the effect of the temperature and humidity in the laboratory on the signal stability showed that these two parameters play a big role in these fluctuations of the signal. In principle, these two parameters should affect laser operation and possibly also the electronics. However, I found that the sensitivity of the laser operation in this system with respect to variations in temperature and humidity was extreme and exceeded the expected dependency on these two parameters by far. Therefore, controlling these two parameters (temperature and humidity) without any additional modifications of the laser system itself was not sufficient to solve these problems.

An inspection of the laser beam at different points inside and outside the laser system showed that the spatial fluctuations of the fundamental beams at the output of the ***amplifier*** were the reason for the fluctuations in the SFG data. This inspection was performed by

coupling out a fraction of the laser beam at selected points and detecting it using a CCD chip removed from a commercial webcam. In this way, the spatial fluctuations were recorded, stored in a PC and subsequently graphically analyzed. These pointing fluctuations, generated at the amplifier, were transformed into instabilities of the SFG signal due to the spatial miss-overlap of IR and visible beam at the interface under study. Why did the ***amplifier*** *cause such problems*? Why ***seasonal phenomena***?! If we look carefully at the design of the laser, Figure 2-1, we find that the beam passes through the *amplifier-rod* twice. There is a high probability for the beam to interfere with itself before and after the amplifier-rod (under the red ellipse), particularly very close and at the back mirror of the amplifier (M5). Hence it is the ***amplifier***. Since we speak about interference then we speak about refractive index then we speak about ambient conditions (Temperature change, humidity change, medium homogeneity, air flow … etc), hence it is ***seasonal*** (i.e. depends on the atmosphere of the lab and the possible air currents which change from day to day and from season to season). To this end, the laser cavity in general has been better thermally isolated and in particular the shielding of *the area around the amplifier-head* has been improved by building a small sub-housing around the amplifier head and the back mirror. Figure 2-6 shows the quality of the spectra before and after fixing the laser instability problem. Before this development, the quality seen in Figure 2-6b used to be accidentally obtained depending on the surrounding atmospheric conditions in the lab. Today, however, this is now standard quality under the usual ambient conditions. Figure 2-6a shows the low quality of the data prior to the modification of the laser system.

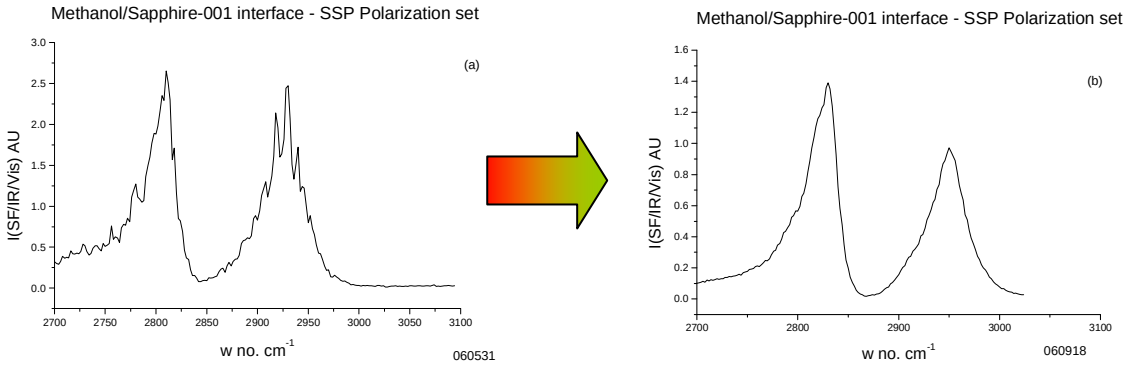

Figure 2-6 The SFG signal in the CH stretching region at the methanol/Sapphire-001 interface (a) before and (b) after improvement of the laser oscillator and amplifier

To overcome the effect of temperature change on the optical length of the oscillator, the end mirror of the oscillator (M1) had been placed on a micro-stage by the manufacturer to allow for manual compensation of the change in the optical length. However, I found that this correction is not sufficient, because the more crucial parameter is the positioning of the non linear crystal (BBO*) and the exit dichroic mirror (M2), of the nonlinear out-coupling mirror combination, and the optical distance between them. To make the positioning of the BBO* crystal adjustable, it has been placed on another micro-stage with the possibility to rotate it axially and translate it in the vertical plane. This is a better design to adjust the BBO* for best phase matching condition.

2.7.2 Irreproducibility due to the temporal miss-overlap

The spectroscopic system used in this work relies on the generation of tunable IR radiation in the range of 2.6-10μm using two nonlinear crystals ($LiNbO_3$ for 2.6-4μm and $AgGaS_2$ for 4-10μm) mounted on a rotating stage inside the OPO cavity. As mentioned in section 2.1, the OPO cavity length should be optimized for each scan sub-range, of the total spectral range, at specific points within the scan range. I found that this process is not reproducible as will be discussed in this section.

Figure 2-7 shows that different SFG spectra could be obtained from the same interface under the same conditions due to different OPO alignments (from one scan to another). These spectra were obtained at the methanol/sapphire interface for the same sample under the same conditions. The scans were carried out successively one after the other after readjusting the cavity length of the OPO at different frequencies within the same spectral range. Two spectral ranges were tested; (a) at the region of high wavenumbers corresponding to the major part of the OH vibrations and (b) at the region of low wave numbers corresponding to the CH vibrations. The IR intensity for each alignment position was plotted. As seen in Figure 2-7, the spectra do change with OPO realignment, which can be wrongly attributed to sample interactions with the solution and thus cause a wrong interpretation of the experimental results; Reproducibility the results may be expected only if all the experiments are carried out at once and without changing the frequency range (i.e. without starting the measurements in the CH vibrational region and then switching to the water bands or the free OH bands and then going back to the CH region and so on). Anyway, this problem appears too crucial to remain unsolved.

To determine the origin of this problem the following test was performed. What can we expect if we do a simple experiment by changing the OPO length (detuning the OPO manually) around a certain wavelength? No doubt that the IR intensity will be reduced and accordingly the detected SFG signal too. I detuned the OPO manually using a micro-stage placed under one of the two end mirrors (M16 in Figure 2-2) and detected the reflected IR (RIR) from the interface and the generated SFG signal as well. Two mutual relations were recorded in dependence of the change of the cavity length; the first is between the RIR and incident IR (IIR) and the second is between the detected SFG and the IIR. Figure 2-8 shows this complex relation when the cavity length was detuned, to shorter and longer lengths, around an optimum length for a certain frequency. The cavity length was optimized to the

highest IR output intensity at a given frequency (wavenumber = 2800cm^{-1}) and then tuned systematically to shorter and longer lengths with detecting the IIR, RIR and SFG intensities. The RIR showed linear dependency on the IIR in both cases, so the reflectivity at the interface was not the reason for the strange phenomenon. Concerning the SFG response to the change of the cavity length, the dependence of the SFG intensity on the IIR intensity is more or less linear particularly in the region where the IIR intensity is higher than 35% of its maximum value, when the cavity length increases longer than the optimum length (the red triangles). However, an unexpected plateau was found in the SFG<>IIR relation when the cavity length decreases shorter than the optimum length (the red squares). This means that the SFG is not always linear with respect to the IIR! If we understand the mechanism of the SFG scan, we can avoid this problem, but not solve it. If we run the SFG scan from higher to lower wavenumbers (i.e. from lower wavelength to higher wavelength), the wavelength of the produced IR elongates during the scan, or in other words, the cavity length shortens relative to the generated wavelengths. To keep the cavity length always longer than the optimum cavity length during the scan, one should chose the longest wavelength (lowest wavenumber) point of the selected scan range to be the point of optimum cavity length (i.e. if the scan will be carried out in the range 2700-3000cm^{-1}, the cavity length should be optimized at 2700cm^{-1} and the scan be carried out from 3000cm^{-1} to 2700cm^{-1}). In addition the scan should be in a range where the IIR does not drop lower than 35% of its maximum value during the scan. In this way, one can produce respectably reproducible spectra. So, the phenomenon has been avoided, but its origin has not been determined yet.

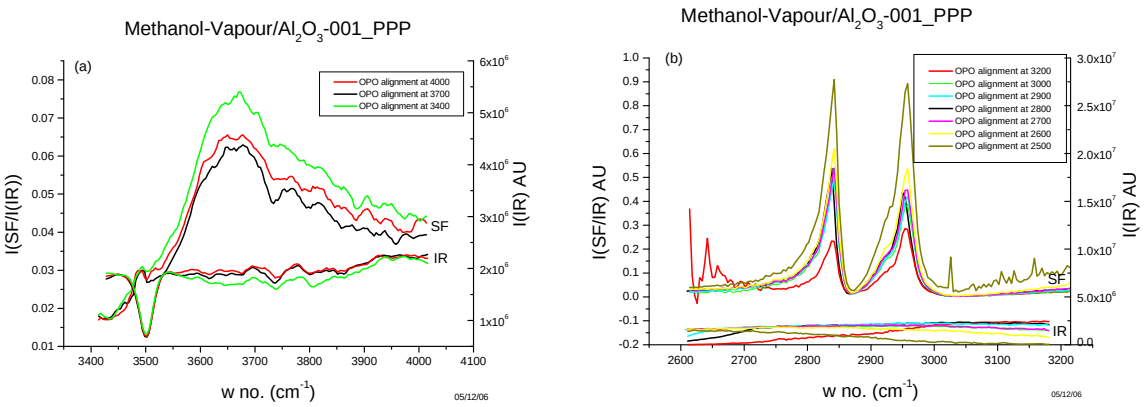

Figure 2-7 The effect of OPO different alignments on the SF signal at methanol-vapour/Sapphire interface under the same experimental conditions in the (a) CH region (with spatial overlap at 2800) and (b) OH region (with spatial overlap at 3700).

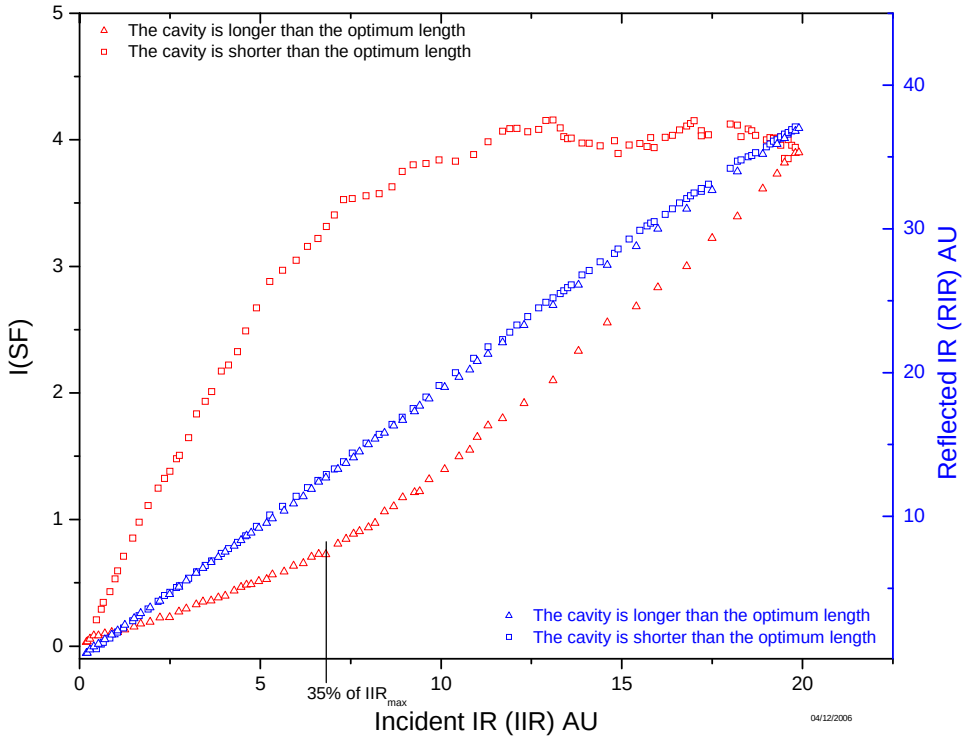

Figure 2-8 The complex relation between the detected SFG and the RIR and the IIR from methanol/sapphire interface. The optimum cavity length was chosen at 2800cm^{-1} (3.571=μm). The RIR has been obtained by introducing D3 to the setup, see Figure 2-2.

It was expected that the beam characteristics (spatial profile, temporal width and the pulse delay) of the tunable IR is the origin of this problem. If one or more of these characteristics are changing during the scan, the efficiency of the SFG process will change too. To study the temporal characteristics of the IR beam, cross-correlation experiments were performed. The SFG at constant IR wavenumber ($2800cm^{-1}$) was obtained from the methanol/sapphire interface. The IR beam was temporally analyzed by changing the temporal delay of the visible light and detecting the resulting SFG at three different optimum cavity lengths (at 3200, 2800 and 2600). The temporal scans were performed using the delay unit in the path of the visible beam. The intensity of the generated SFG signal was measured as a function of the delay unit displacement and plotted as shown in Figure 2-9. The displacement of the delay unit can be translated later into a time delay of the visible beam. However, the transformation from displacement units to time units has not been done here since we are not interested in the actual delay time rather than the temporal shape of the IR beam. Figure 2-9 shows that different OPO alignments lead to changes in the IR pulse delay and/or width, which in turn will change the efficiency of the SFG process. A similar experiment was performed for a SFG signal corresponding to an IR wavenumber of $3700cm^{-1}$ and an OPO cavity optimization at the same wavenumber. The result is plotted in Figure 2-10 together with the cross correlation for the SFG at $2800cm^{-1}$ and an OPO cavity optimization at $2800cm^{-1}$. The data show that the efficiency of the SFG process will change from one scan range to the other if the temporal delay is kept constant.

According to the discussion above, it is expected that some changes in the spectra can be due to miss-synchronization between the incident beams, in addition to those, which may come from miss-spatial overlap, and accordingly are not due to medium/surface interactions. Hence, a scan of wide spectral range at once is useless and could lead to wrong interpretations. This effect is mostly generated by the rotation of the nonlinear crystal in the OPO cavity during the spectral scan and the according change in path and orientation of the beam within the crystal. The recommendation here is to split the scan of the entire spectral range required into small parts each of which with its own OPO alignment, delay adjustment and spatial overlap. However, this process is rather tedious and therefore has been automated as will be discussed in the next subsection.

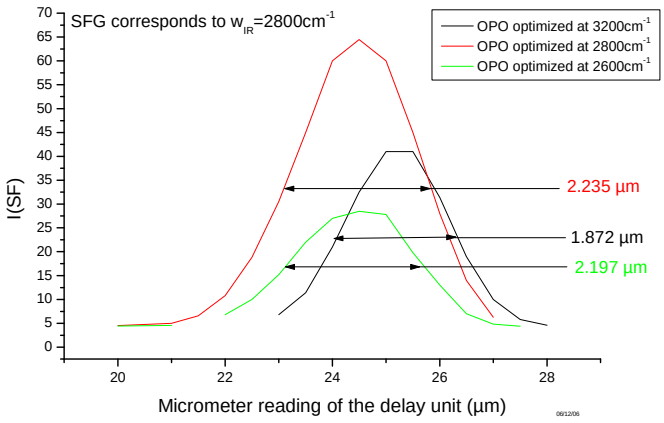

Figure 2-9 A cross-correlation relation between the IR and the visible beams. The SFG at methanol/sapphire interface was obtained at constant wavelength during scanning the IR beam temporally by the visible beam for three different optimum lengths of the OPO cavity at 3200cm^{-1}, 2800cm^{-1} and 2600cm^{-1}.

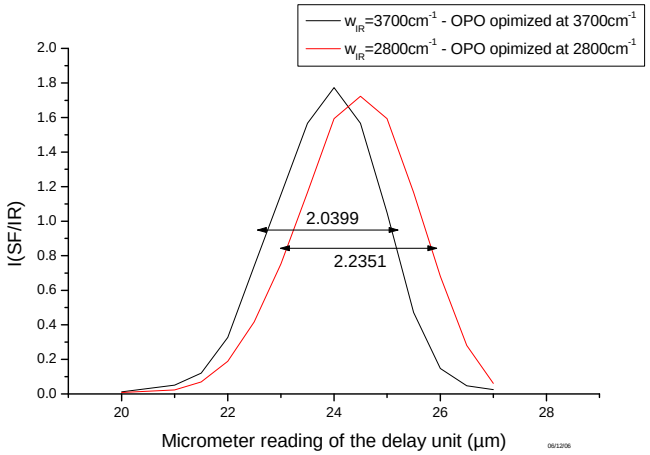

Figure 2-10 A cross-correlation relation between the IR and the visible beams for two SFG signals corresponding to two different IR frequencies (3700cm^{-1} and 2800cm^{-1}) each of which has the OPO cavity length optimized at it.

2.7.3 Automation of the OPO cavity length and delay unit

The importance of the adjustment of the OPO cavity length and the temporal delay from point to point during the scan was described in the last subsection. Also, it was recommended to divide the entire scan range into small parts each of which with its own cavity length and delay optimization. Further, it was mentioned in the laser description section that the OPO cannot be calibrated to the full spectral range achievable with using only one of the two nonlinear optical crystals. To overcome these difficulties, two computer-controlled micrometer screws (PI M-230)[1] have been added to the system. The first micrometer screw was installed under the back mirror (M16, Figure 2-2) of the OPO cavity and the second one was coupled to the delay unit. The screws can be programmed to move during the scan process in a way that they keep the conditions always optimal.

Concerning the calibration of the OPO cavity, the moving stage under M16 was programmed in such a way that it moves continuously during the calibration process of each of the NLC, M1 and M2 of the OPO cavity. This continuous motion was programmed to have the OPO cavity always optimized to generate sufficient IR intensity at all wavelengths. Finally, a calibration file for the full spectral range was obtained. The advantage of this full-scan calibration file is that the scan can be carried out for the full spectral range given by the selected NLC in a single run since there is no need to interrupt the scan and load specific calibration files from range to range.

It is worth to mention that this development of the system not only solved the discussed problems but also reduced the time for an experiment to 25% of that required in the past. The full spectral scan, which used to take more than 40min with the risk of introducing additional errors arising from the manual optimization, takes now 10min with higher repeatability of components positioning.

[1] Physik Instrumente (PI), www.pi.ws

2.7.4 Reflectivity at the interface

As discussed in chapter (1), the optical constants at the interface and hence the corresponding Fresnel Factors play an important role in the obtained results. In other words, the experimental geometry influences the efficiency of the generated signal. As discussed in the section of the data analysis, the obtained signal will be corrected for the Geometry Factors. Thus one should assure that the Geometry Factors used in the theoretical calculations agree with the experimental ones. The easiest way to do this is to test if the experimental reflectivity at the interface agrees well with the theoretically calculated one. The reflectivity is a liner process that has less number of parameters than those of the SFG. Figure 2-11 shows the reflectivity (for S-polarization) from the methanol/sapphire interface obtained at different incident IR energy densities in the spectral range from 2750 to 3200cm^{-1}. The angle of incidence of the IR beam from air to the prism side was 13°. It shows also the theoretical curve. It is obvious that the higher the incident energy density the more the experimental reflectivity deviated from the calculated one while better results were obtained by defocusing the IIR beam. Similar results were obtained by reducing the energy density by fractional absorption of the incident light. This means that increasing the energies of the incident beams in the SFG experiment to get a higher SFG signal is not always an advantage. Extreme focusing and intensifying the incident beams may result in the acquisition of meaningless data.

Potential reasons for this behavior are that the high fields at the interface generate mechanical waves, cause ***thermal effects,*** and/or saturation in the absorption of the layers close to the interface and within the penetration depth of the light. One should recall here that the laser system applied is a pulse-train system and not single pulse system. Although it therefore has the advantage of having high output power due to the pulse trains it has the disadvantage, particularly when dealing with liquids, that with each pulse train an extensive shower of individual pulses bombards the interface within short time intervals of few nanoseconds only. Therefore, the medium under study has no time for relaxation between two consecutive pulses within the same pulse train. All these phenomena can change the optical properties of the media at the interface. In addition, an intense focused beam can produce bubbles in the liquid phase which in turn form moving lenses at the interface, which might act as microlenses. This, however, should lead to strong fluctuations in the detected SFG signal. As seen from Figure 2-11, reducing the energy density by defocusing the IR beam gives

reasonable reflectivity. The suggestion here is to adjust the incident field strength in a way that the optical constants are still not affected, while the intensity is sufficiently large to allow SFG with reasonable S/N ratio. Reducing the field strength can be accomplished by either partial light absorption or defocusing. The partial absorption of the tunable IR can be achieved by introducing two suitable optical plates of high refractive index (e.g. Si-windows) in the IR path. By rotating the two plates counterwise, the transmitted field will be reduced further while the beam path will be preserved. On the other hand, the IR field can be reduced by defocusing the IR beam using the lens L3 in Figure 2-2. Both methods were used in this work. However, defocusing is the recommended method for the reasons discussed in the next subsection. It was found that the optimum energy density for the system used in this work is 4mJ/cm^2.

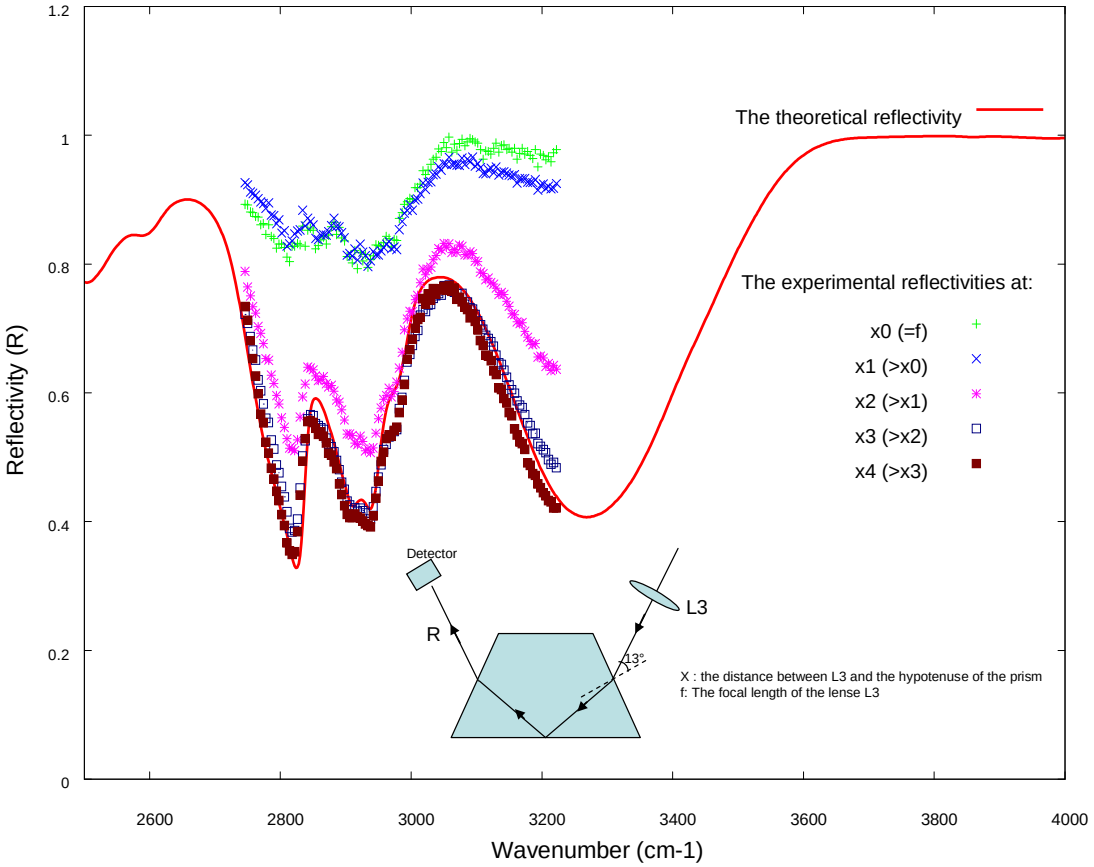

Figure 2-11 The IR reflectivity at the methanol/sapphire interface at different distances from the focus x0=f of lens L3, Figure 2-2. (S- Polarized beam)

2.7.5 The spatial overlap

As discussed in context with the experimental setup (section 2.2), the spatial overlap is achieved using the 3D movable holder of lens L3. However, during the scan this overlap drifts due to the fact that the tunable IR will suffer refraction at the air/sapphire interface at the incident side of the prism-like sample. This refraction is wavelength dependent and hence the focus of the IR beam will move during the scan. This movement will cause a change of the position of IR spot on the medium/sapphire interface, which displaces it from the overlap position. This problem can be solved by increasing the overlap area as long as the system achieves still an energy density at the interface sufficiently high to produce SFG. For this reason, the alternative of reducing the energy density by defocusing the IR beam was recommended in the previous subsection. However, the effect of beam displacement on the overlap discussed here is much smaller than that on the calculated Geometry Function discussed in the analysis section.

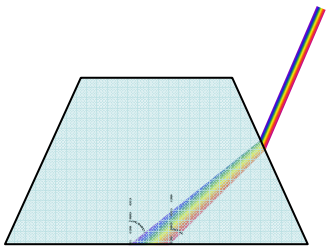

Figure 2-12 The resultant miss- spatial overlap and angle of incident at the medium/solid interface due to the wavelength change during the scan

It is worth to mention that the effect of the angular change of the incident IR and the corresponding generated sum frequency beam were taken into consideration in calculating the Geometry Factors and the optical constants on basis of the IR-TIR results discussed in this thesis. Thereby, the two angles were introduced into the equations as functions of the wavenumbers. These functions were governed by Snell's law of refraction.

2.7.6 Electronic interference

Complex ultrashort pulse lasers and spectroscopic systems as used in the present work are packed with sensitive electronic components and connections. I found that a bad contact in the PNC cables caused some spikes in the spectra. The grounding of the electronics and the electrical components in the lab should be as best as possible. Sometimes long term fluctuations, not like those in Figure 2-6 but rather of larger time scale (few seconds to minutes), could be observed. Good grounding for the electronics and the metallic optical bench yielded better stability.

The system was equipped with two shutters for measuring the background as described in the data acquisition section, which were connected directly to the electronic box used for handling the trigger signal. This electronic box was weakly biased and thus the operation of the shutters was not satisfactory although they were not designed for high current. These two shutters were replaced by two others (Interlock SH-20-12) from Laser 2000[1] with 15msec response time and 1 inch aperture. The new shutters required 7.2watt power (12V, 600mA). I built a two channel amplifier circuit to amplify the signal coming from the controller using external biasing, Figure 2-13. I installed a third shutter inside the oscillator cavity. This shutter was used as safety shutter to cut the lasing operation in case of any accident or malfunction. It is worth to mention that, if the mode locking condition is lost for any reason inside the cavity, long high energy pulses will be transmitted to the AOM and damage it. Also, if the AOM malfunctioned accidentally for any reason, a non-modulated pulse trains will pass to the amplifier. All components in the amplifier and after the amplifier are then at risk due to the high power of the non-modulated beam.

[1] Laser 2000 GmbH**,** Argelsrieder Feld 14, D-82234 Wessling - Germany

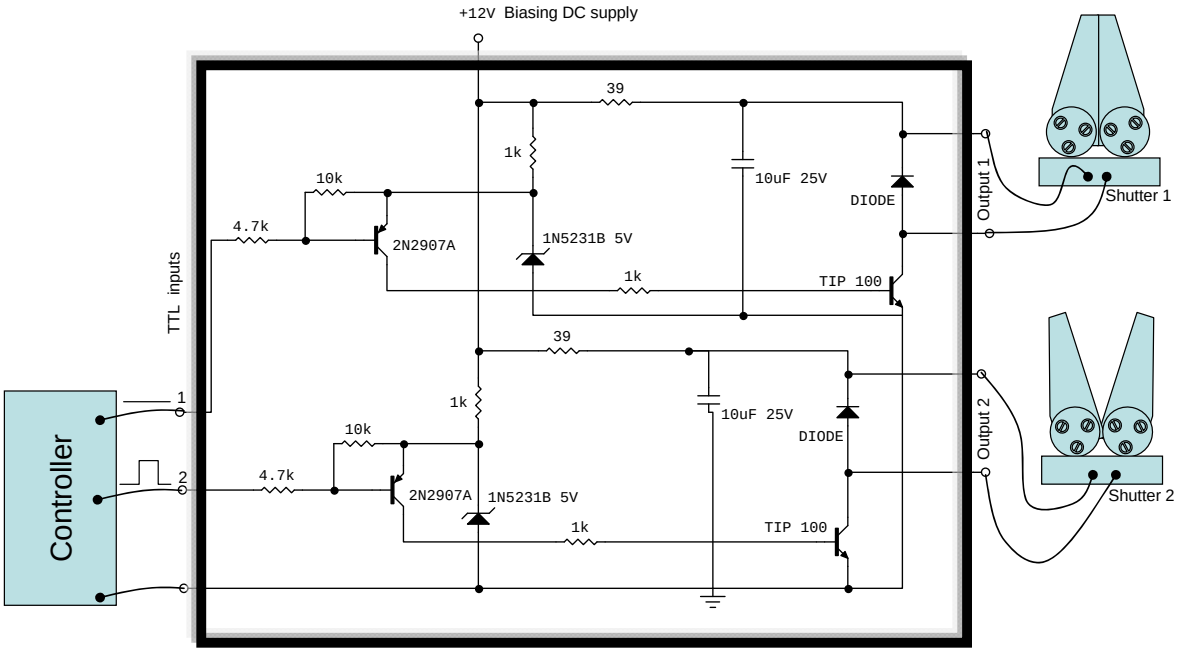

Figure 2-13 A sketch of the home made two-channel-amplifier circuit which has been used to amplify the signal coming from the controller to drive the shutters

2.8 The home made Contact Angle Measurement Instrument (CAMI)

It is always advantageous to have a simple inspection tool at hand to check on cleanness and wetting behavior of the sample surface prior to any elaborate analysis. For this reason, I decided to build the CAMI described in the following, using equipment already present in our laboratories. Geometrically, the contact angle is defined as the angle formed by a liquid at the three phase boundary where a liquid (L), vapour (V) and solid (S) intersect. It is a quantitative measure of the wetting of a solid by a liquid (hydrophilicity / hydrophobicity), surface tension, adhesion, cleanliness, and biocompatibility [see Appendix 9a].

My home made ***Contact Angle Measuring Instrument CAMI*** is based on the use of a "Leica/Wild Heerbrugg M8" Optical Microscope as an inspection unit coupled to a "*uEye"* CCD Camera, which in turn is connected to a PC. The "*uEye*" software provided with the camera is able to capture high resolution images from this combination. The design and construction of the required mechanics for converting this combination to CAMI have been done at INE. The final construction can be used as either an ordinary optical microscope or a CAMI, depending on the orientation of the system with respect to the sample surface (vertical for microscope mode, horizontal for CAMI). The sample under inspection is illuminated with a fibre optics coupled to the "*SCHOTT"* light source. The device has been calibrated to one state of focus (when the liquid droplet is positioned at the focus of the optical microscope while the magnification is put to maximum). However, a different calibration is always possible and described in the subsection 2.8.3.

The components of the CAMI are shown in Figure 2-14, each of which has its function either in measurement and/or in calibration. The alignment, measurement and calibration of the instrument will be described in the following three subsections. The instrument has been used in this work to differentiate between the different cleaning steps and to observe, roughly, the wettability of the sample surface after exposure to different media. However, many physical parameters can be extracted from contact angle measurements. Useful formulas are presented in [Appendix 9b].

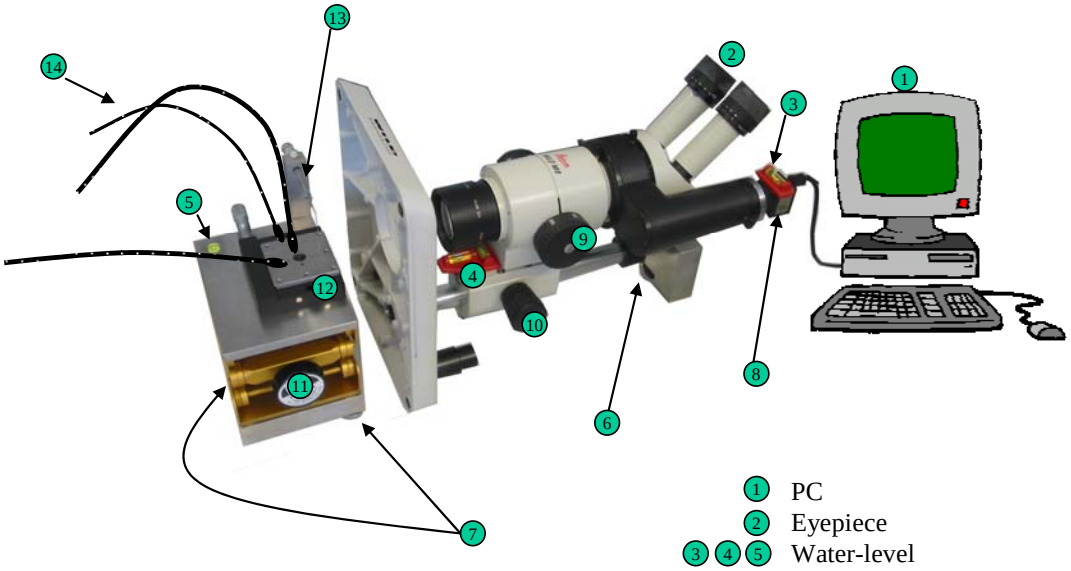

(a) The Contact Angle Instrument Sketch

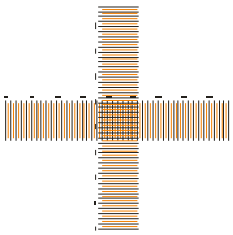

(b) The Calibration Cross

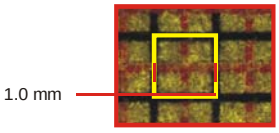

(c) The captured image

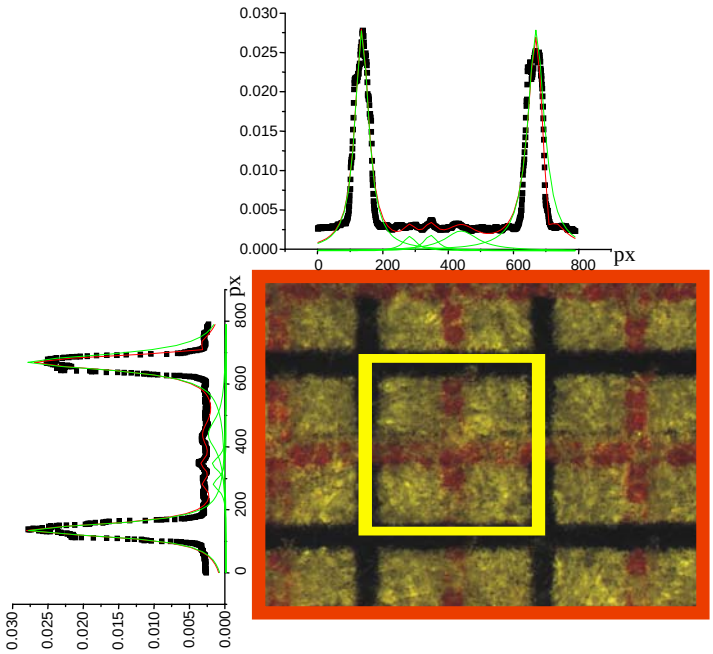

(d) Picture deconvolution

Figure 2-14 (a) Sketch of the home made contact angle instrument including the termination of the different components, (b) The calibration cross which can be used in calibrating the CCD camera, (c) A captured image showing the calibration cross and (d) the transformation of the captured image to intensity distributions in x and y direction.

2.8.1 CAMI Alignment

1. Adjusting the microscope and the sample holder horizontally using the levelling screws (6 and 7) and the water-levels (3, 4, and 5).
2. Placing the sample on the sample holder (12) and using the illumination fibres to get the best view of the sample edge from the Eyepiece (2)
3. Running the camera software and confirming that the camera (8) is aligned horizontally by focusing the view on the sample holder edge (12). If required, the camera can be rotated using the side screw which keeps the camera in place. The focus can be adjusted by the Focus Knobs (9 and 10). It is recommended to adjust the focus using (10) and keep (9) at the setpoint 50 to use the default calibration.

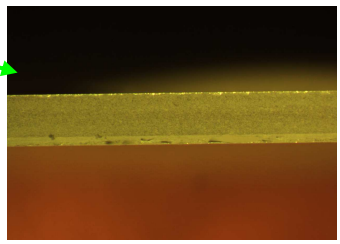

Tip: Whenever the horizon can not be brought into sharp focus, the microscope should be tilted about 3° using (6).

2.8.2 Contact Angle Measurement

4. The Syringe tip (13) should be adjusted right over the sample.
5. Using (10), (11) and the micrometer screw of the sample holder (12), the syringe tip can be brought into the focus.
6. By operating the syringe carefully, a small hanging droplet of water can be generated at its tip.
7. By elevating the sample slightly and carefully, using (11), the surface will touch the water droplet and the droplet will adhere to the surface.
8. Adjusting the focus again until the rim of the half sphere formed by the droplet is in focus. It is better to use the same droplet volume (using a graduated syringe) in all experiments if comparing of results is demanded. It is also recommended to use a droplet as small as possible to minimize the influence of gravity on the shape of the sessile drop.

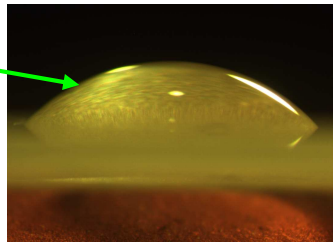

9. Now, a picture can be acquired by means of the camera system, stored and then edited with a suitable graphic software (Corel designer is recommended).

10. It can be roughly decided whether the surface is hydrophilic or hydrophobic in dependence of whether the contact angle is smaller or larger than 90 degree, respectively.
11. Using the graphics software two lines can be drawn; one is parallel to the base and the other is the tangent to the half sphere border; then the contact angle is defined as the inner angle of these two lines, i.e. the angle inside of the drop.

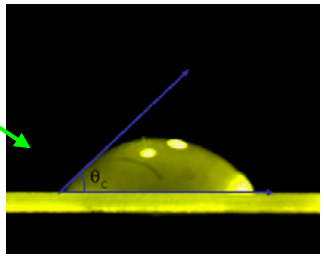

12. If the study requires measuring the dimensions of the droplet on the surface, then the camera should be calibrated.

2.8.3 CAMI Calibration

The camera is already calibrated to the state where the focus is obtained by knob (10) when knob (9) is at 50. In this case the dimensions will be related to the number of pixels measured by the graphic software as follows:

x: 1mm~505px

y: 1mm~530px

This means that the resolution of the camera of 1280px X 1024px corresponds to 2.55mm X 1.93mm. (The obtained picture should be resized to these dimensions)

To calibrate the camera for a different setting, the following steps can be performed:

1. A small millimetre paper is to be stacked on the sample holder edge. It is recommended to use the Standard Calibration Cross SCC, Figure 2-14b which can be printed from www.amamonem.de
2. By following the steps 1-3 in (section 2.8.1) an image of the SCC with good resolution should be acquired, Figure 2-14c.

Using suitable software (Winspec is recommended)[1], one can transfer this obtained 2D image to 3D (x,y,Intensity), and deconvolute it to I(x) and I(y) as shown in Figure 2-14d. To get an exact calibration, one can fit the intensity peaks to Lorentz bands using, for example, the Origin software. The difference between the central positions of two successive peaks in pixels corresponds to 1 mm.

[1] WinSpec/32 from Roper Scientific

2. Experiment, Materials and Data Analysis

CHAPTER 3

RESULTS AND DISCUSSION

3. Results and Discussion

3. Results and Discussion

The air-solid and/or liquid-solid interfaces of methanol, ethanol, 1-propanol, 1-butanol, chloroform and propionic acid in contact with sapphire 001 and/or 110 were investigated in this work by means of nonlinear optical vibrational spectroscopy, i.e. SFG, to better understand the complex interaction of organic substances with mineral surfaces on the molecular level. The SFG spectra were collected in the regions of the CH and OH stretching vibrations (~2500-4000cm^{-1}). All the results showed high affinity between sapphire and water molecules and gave evidence for the existence of strongly bonded water on the sapphire surface prepared as detailed in section (2.5) and investigated under the experimental conditions described in section (2.2). To provide a reasonable analysis and interpretation of the data, linear and nonlinear techniques were applied. The optical constants of the liquids used were determined for the TIR geometry used in the SFG experiments. From these linear measurements, first the Fresnel coefficients were calculated and then the nonlinear Geometry Factors described in section (1.4) determined. On this basis, the SFG data were not only corrected with respect to the transmission of the optical elements, such as the used optical filters, but more importantly to the Geometry Factors. This correction paved the way for proper determination of the preferential orientation of molecular groups interacting with the sapphire surface.

3.1 Linear Spectroscopy: Total Internal Reflection (TIR)

The IR signal reflected from the liquid/sapphire interface was detected at a position right after the sample in the geometry described in chapter (2). Figure 3-1 shows the experimentally measured reflectivities for P- and S-polarized beams for methanol, ethanol, 1-propanol, and 1-butanol. The laser output energy was held at a minimum value still sufficient to produce a signal with reasonable S/N ratio in the SFG experiments. This condition was chosen because of the requirement to obtain comparable values of *n* and *k* to those in the literature and to acquire good quality SFG spectra at the same time. The *n* and *k* values of each medium were calculated as described in section (1.4.2). The calculated *n* and *k* values are displayed graphically in Figure 3-2. The values obtained for methanol are in a good agreement with those published by J. Bretie [28], while the values for the other compounds were not found in the literature. It is obvious that *n* and *k* depend on the frequency and thus their contribution to the Geometry Factors is significant.

3. Results and Discussion

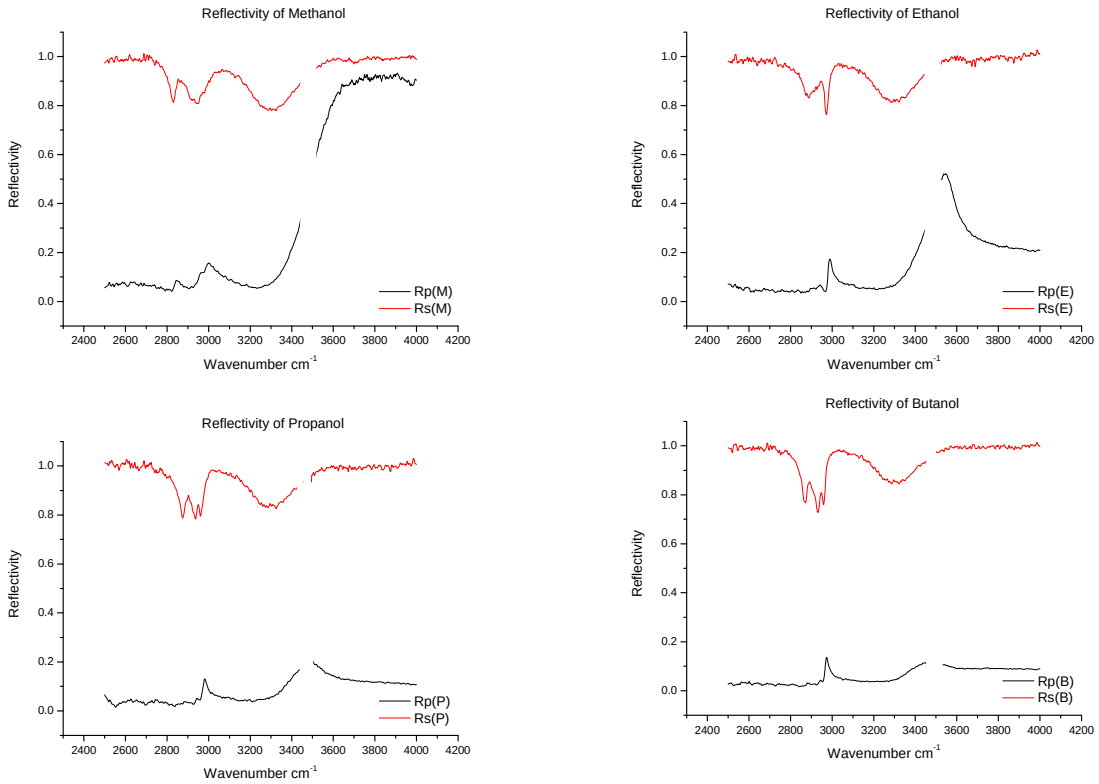

Figure 3-1 The experimentally measured reflectivities for P- and S- Polarized light for methanol, ethanol, 1-propanol and 1-butanol.

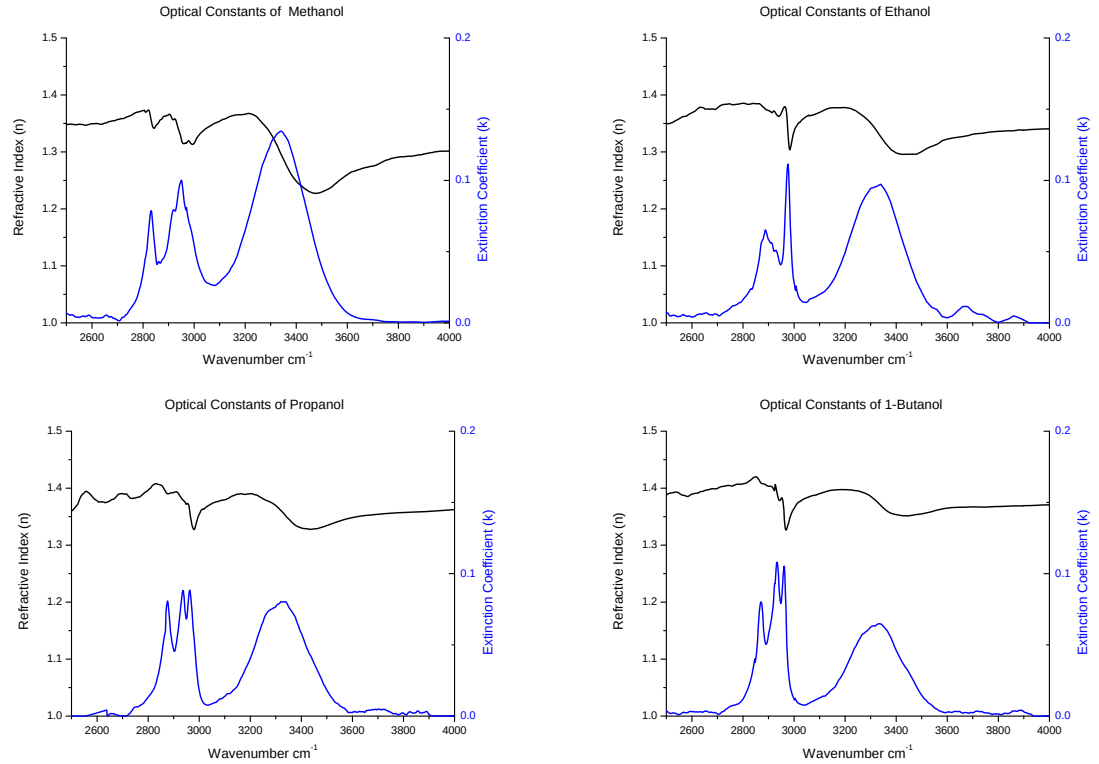

Figure 3-2 Real *n* and imaginary *k* parts of the complex refractive index for P- and S- Polarized light for methanol, ethanol, 1-propanol and 1-butanol.

The optical constants of the chloroform were also investigated but they are not plotted here because they found to be weakly dependent on the wavelength in the selected range. However, the mean value of the extinction coefficient was about $\langle k \rangle$ =0.005, which is more or less zero over the selected range, and that of the real part was about $\langle n \rangle$ =1.4.

In the following, the Geometry Factors are calculated for each liquid/sapphire interface. The Geometry Factors were calculated for the specific incident angles used in the corresponding experiment. The experiments should have been carried out at the critical angle of the total internal reflection for the reasons discussed in section (1.5.1). However, in some cases the spectral scans of different media had to be carried out at the same angle (e.g. at the critical angle for only one of them) to maintain some condition or to observe intentionally some change upon changing the medium. In these cases, the Geometry Factors of these media were calculated with the given angle. To ignore the angular dependency of the Geometry Factors in such a case would make a drastic difference. As an example, Figure 3-3 compares the Geometry Factors at the water/sapphire interface for the two cases that (i) the experiment is carried out at the critical angle of 1-butanol/sapphire or (ii) at that of the water/sapphire interface, respectively. Evidently, the deviation between the two data sets is sufficiently high to introduce a large error in an experiment, if, e.g., the critical angle of the 1-butanol/sapphire interface would be chosen to measure the water/sapphire interface. Also, the figure illustrates the variance that occurs in the Geometry Factors upon changing the contact medium at the same angle of incidence.

It is worth to mention that the Geometry Factors for mixtures should be calculated independently since the optical constants of the mixtures change with the relative concentration. However, in the present work, the effect of mixing two liquids on the resultant optical constants was ignored because the compounds were prepared at tiny amount of one liquid dissolved in the other. Namely, in the experiments of butanol-water mixture/sapphire interface the volume of the water ranged from 0 to 15% of the total volume. In addition, the main conclusions are drawn from the lowest concentrations where the water volume was lower than 7% of the total volume.

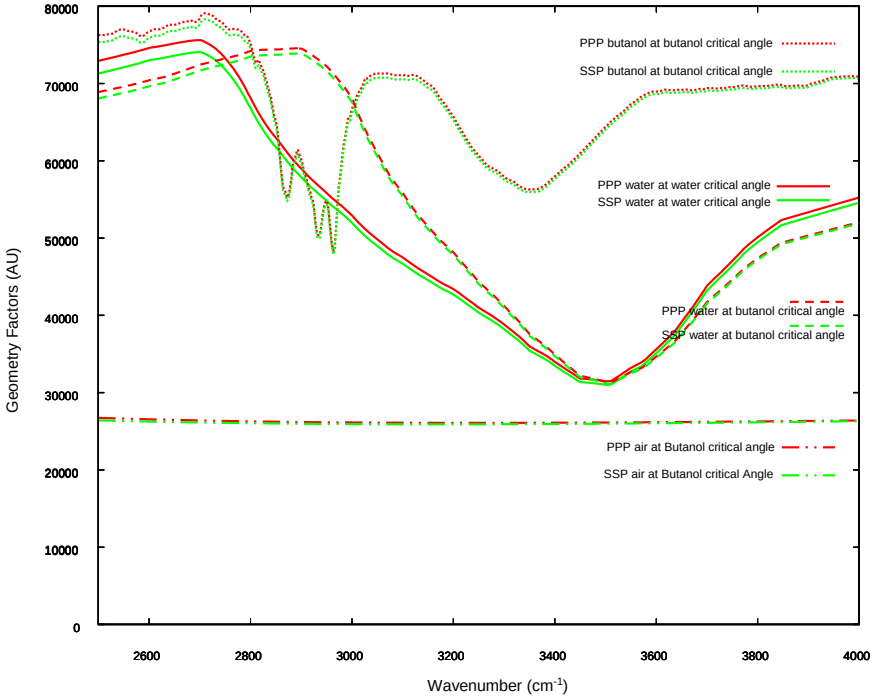

Figure 3-3 The Geometry Factors for different liquid/sapphire 001 interfaces at the critical angle of TIR for 1-butanol.

3.2 Nonlinear Spectroscopy: SFG

This section is divided into five subsections, each of which describes one system of the studied liquid/sapphire interfaces. However, the subsections are crosslinked and interact with each other. The focus will be on the first subsection where the adsorption-desorption of 1-butanol on the sapphire surface in the presence of different amounts of water will be discussed. The following subsections will be used to confirm the conclusions drawn from the first one. The concentrations in the butanol-water mixtures experiments will be expressed in terms of the **bulk** Mole Fraction of butanol in the butanol-water mixtures. It is worth to mention here that the bulk concentration does not necessarily correspond to the molecular concentration at the surface; however, the bulk concentration will serve as a reference. All the following spectra are corrected with respect to the Geometry Factors and the optical filters used and represented in field (E) units unless something else is stated. The spectra are represented in field units because this quantity is directly proportional to the second order nonlinear susceptibility. The use of intensity units ($=E^2$) usually hides some important features in the spectra. The discontinuity in the spectra around $3490cm^{-1}$ is due to the absorption of the $LiNbO_3$ crystal in the OPO system. This discontinuity hampers the data fitting in the region of the OH stretching vibrations.

3.2.1 SFG at the butanol-water mixture/sapphire-001 interface

In order to investigate whether butanol molecules and/or water molecules adsorb to the surface and with what affinity, the following procedure was chosen: first a spectrum was obtained at the neat butanol/sapphire interface, then small amounts of water were added to the initial volume of butanol (100mL) under steering in the mixing reservoir. Increasing water concentration by very tiny steps showed an inversion in the spectral line shape. The detection of this phenomenon required high laser stability, high signal-to-noise ratio and high spectral resolution, which were described in the section of system development (section 2.7). An animated representation of this inversion point in the spectra is submitted with the electronic version of this thesis and can be found under the URL link mentioned in Appendix (7e). Figure 3-4 shows SFG spectra at the butanol-water mixture/sapphire interface for different compositions. Relative concentrations are expressed in terms of the bulk butanol Mole Fraction X_B. The collection of spectra was started at $X_B = 1$ and stopped at $X_B = 0.522$ where the experiment is limited by the finite miscibility of water in butanol (1.95mL water in

9.05mL butanol, $X_B = 0.5$). Beyond this value, phase separation would occur in the bulk solution.

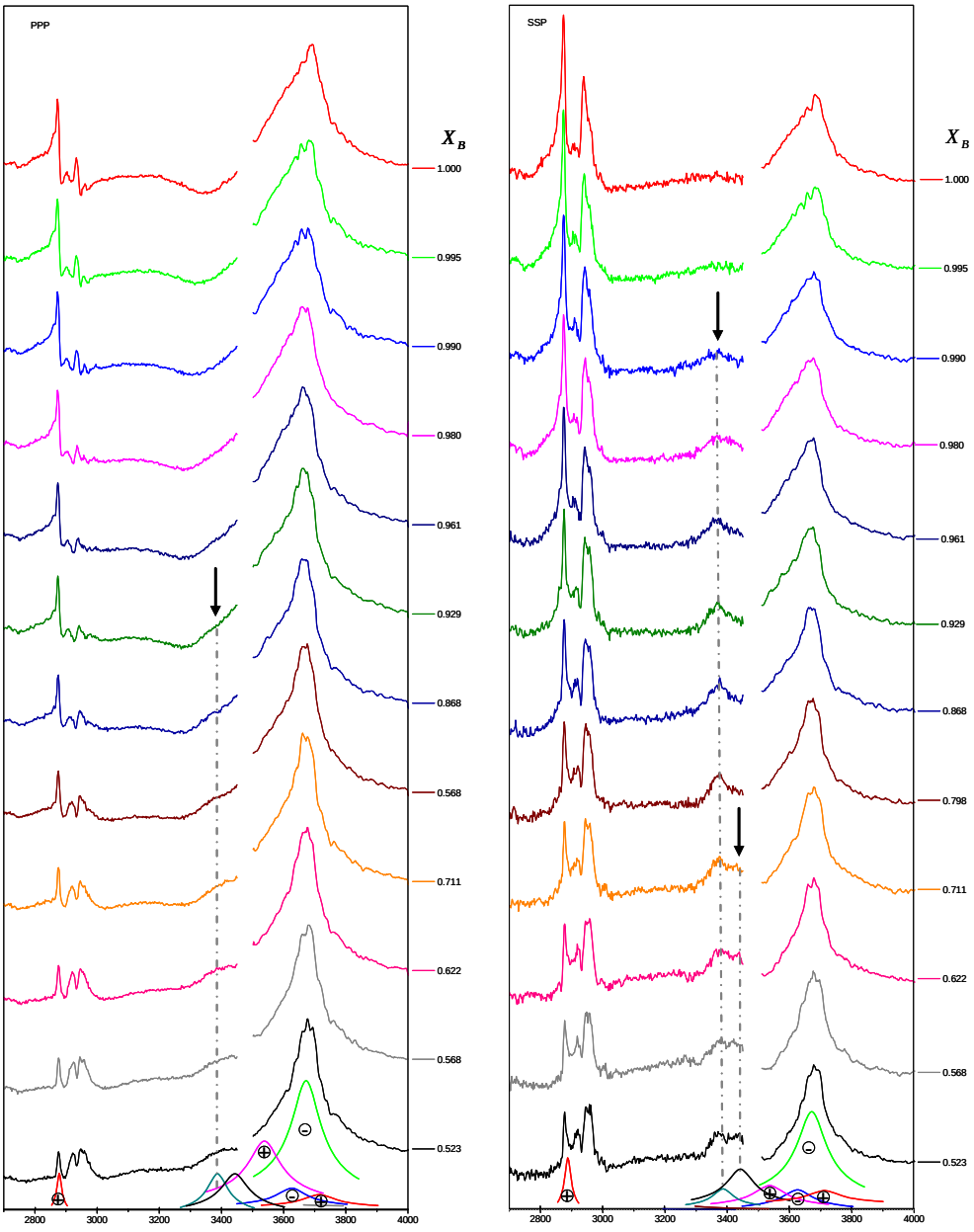

Figure 3-4 SFG spectra for PPP and SSP polarization sets at butanol-water mixture/sapphire interface for different compositions (X_B). At the bottom of each set of spectra, individual de-convoluted bands are shown. Not all the de-convoluted peaks are displayed but only those which participate in the interpretations

Following the evolution of the spectral features upon the successive addition of water, by either watching the animation file or by close inspection of Figure 3-4, it can be seen that some parts of the spectra either increase in PPP and decrease in SSP or decrease in PPP and increase in SSP or either increase in both or decrease in both. In some cases the observed changes are correlated and in other cases not. A close inspection of these findings allows an interpretation which gives plausible answers to the following questions: **What is the mechanism of interaction?** Do butanol molecules desorb due to addition of water (competition)? Do they rearrange (Orientation?)? Do they H-bond to surface OH? Do they H-bond to sorbed water OH? Do water molecules form a strongly bond film on sapphire? Do we measure water and/or aluminol species at high wavenumbers? ***Can we answer these 'Do' questions? (and if so, with what accuracy?)!***

Requirements for answering these questions are: 1) technically, high resolution spectra, good stability and reproducibility, 2) experimentally, appropriate sample preparation and cleaning, 3) analytically, good fitting (starting parameters, reasonable band assignments ...etc), 4) theoretically, calculating the molecular orientations based on the fitting results.

The deconvolution of the spectra results in a large number of peaks. The broad features at the high wavenumbers part of the spectrum (OH stretching vibrations) are typically difficult to resolve. This is because the OH stretching vibrations from water, alcohols and surface hydroxyls may contribute to this part. Their bands, whether in H-bond environment or not, are expected to overlap. This has been shown in many previous investigations of water/mineral, air/mineral, air/(water or liquid) interfaces [49, 53, 64, 65, 66, 69, 75, 77]. The details are coming within the following subsections when discussing the individual bands. Since the bands produced by the CH vibrations are comparatively narrow, their interference with the background and the broad water bands is weak. In addition, they have relatively well defined peak positions compared to the OH vibrations. Thus, this part of the spectrum is a good choice for starting the fitting procedure and identifying reasonable starting parameters. In principle, bands at high wavenumbers may affect the parameters of the CH bands and hence the overall results; e.g. the values of the calculated orientation angles with respect to the surface normal, but to what extent? To answer this question, four different models were chosen to describe the high wavenumbers region of the spectra. If one of these models is the right one then all others are absolutely wrong, if not all of them. Figure 3-5 shows four different cases of fitting the CH vibrational bands of the neat butanol/sapphire interface with

the different models for the high wavenumbers region. In Figure 3-5a both a resonant and a non-resonant background, which result in the occurrence of certain interference effects in the CH vibrational region, were assumed. As seen in the figure, it was possible to find a set of parameters which fits both the PPP and SSP spectra of the data set simultaneously. In Figure 3-5b, a high non-resonant background without resonant broadband was assumed and another self-consistent set of parameters was found to fit the same data set. In Figure 3-5a and Figure 3-5b, it was assumed that the used SFG system does not collect data in the OH stretch region and only the CH region is accessible (this is a common practice in many of the published studies). In Figure 3-5c it was assumed that the free OH vibrational region is a composition of a large number of narrow bands corresponding to different surface hydroxyl groups of different orientations and H-bonding (oscillator) strengths. This assumption would be in good agreement with numerical results obtained by *Quantum Chemical theory* for a bare hydroxylated sapphire surface in contact with water vapor [67]. However, this is not necessarily a relevant case because these theoretical results did not take into account the effect of H-bonding on the vibrations of the bare hydroxyl groups. This becomes evident when comparing bands of hydroxyl groups measured in the absence of water with spectra obtained in the presence of water. Again a self-consistent set of parameters that fits the PPP and SSP spectra of the same data set was obtained. Finally, in the fourth case shown in Figure 3-5d, some broad OH bands, which agree with those published in the literature for air/water interface and air/oil interface [12, 48, 69, 71], were assumed along with a minimum number of additional bands required to fit the data set in both polarization combinations. In Figure 3-5c and Figure 3-5d the high wavenumbers region was taken into account in the fitting assuming that the only contribution may arise from an ordered, low symmetry water structure in vicinity of the surface.

These are four out of an infinity number of possible solutions which can yield good fitting for SSP and PPP spectra. This indicates that this is not the way to determine the right solution. So, what is the appropriate approach? The reassuring result of this fitting exercise is that the high wavenumbers region does not affect significantly the results for the CH region independent of the model used for their description (e.g., the variation in the calculated chain orientation angle of the butanol molecules is about ±3° as will be shown later). Therefore to start the fitting with the CH bands, calculate the orientation of the butanol chain axis with respect to the surface normal and determine the influence of the wrong assumptions on this result is a reasonable strategy.

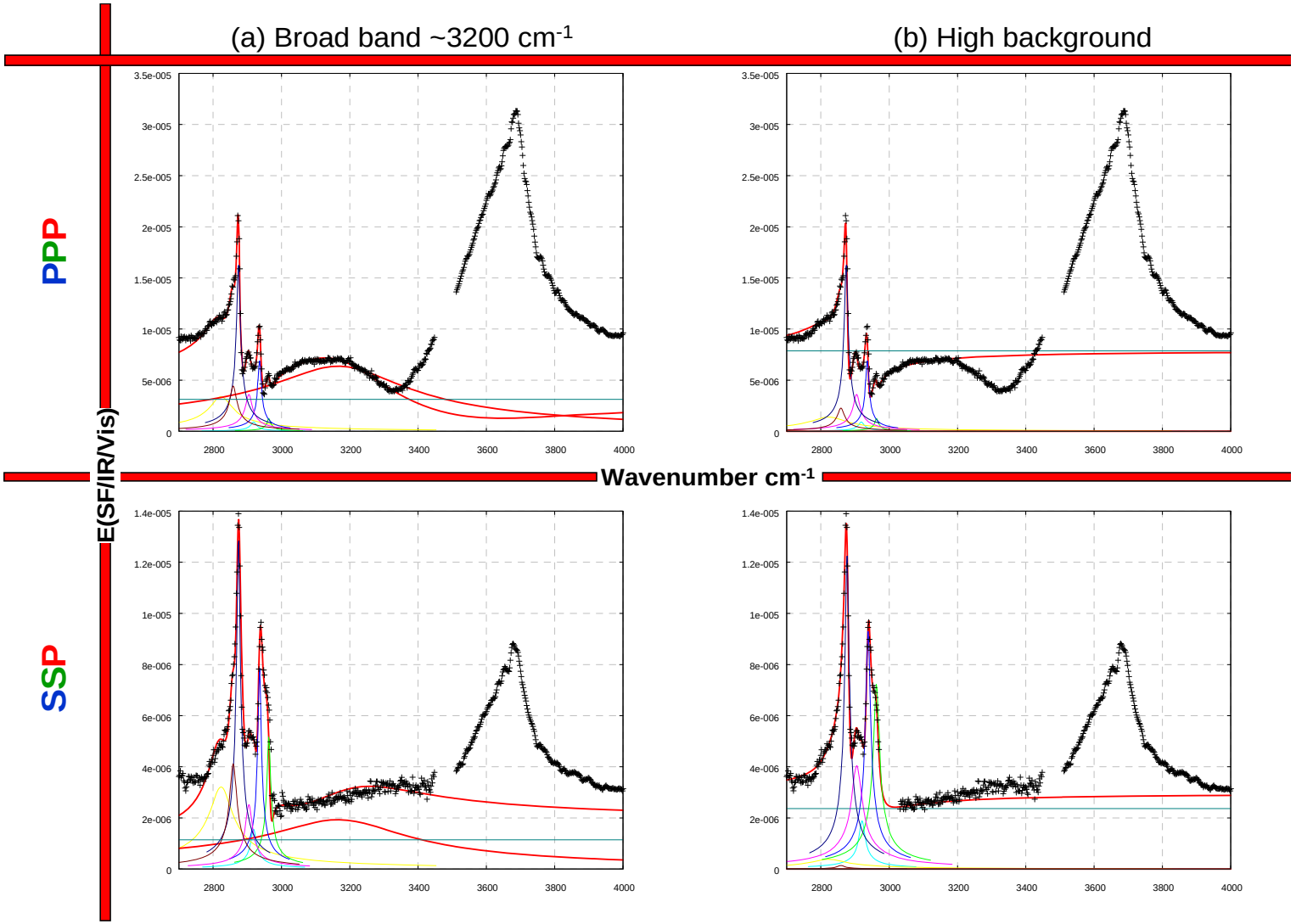

Figure 3-5 Four different fitting options of the CH vibrational bands of the neat butanol/sapphire interface based on different assumptions with respect to the spectral features at high wavenumbers.

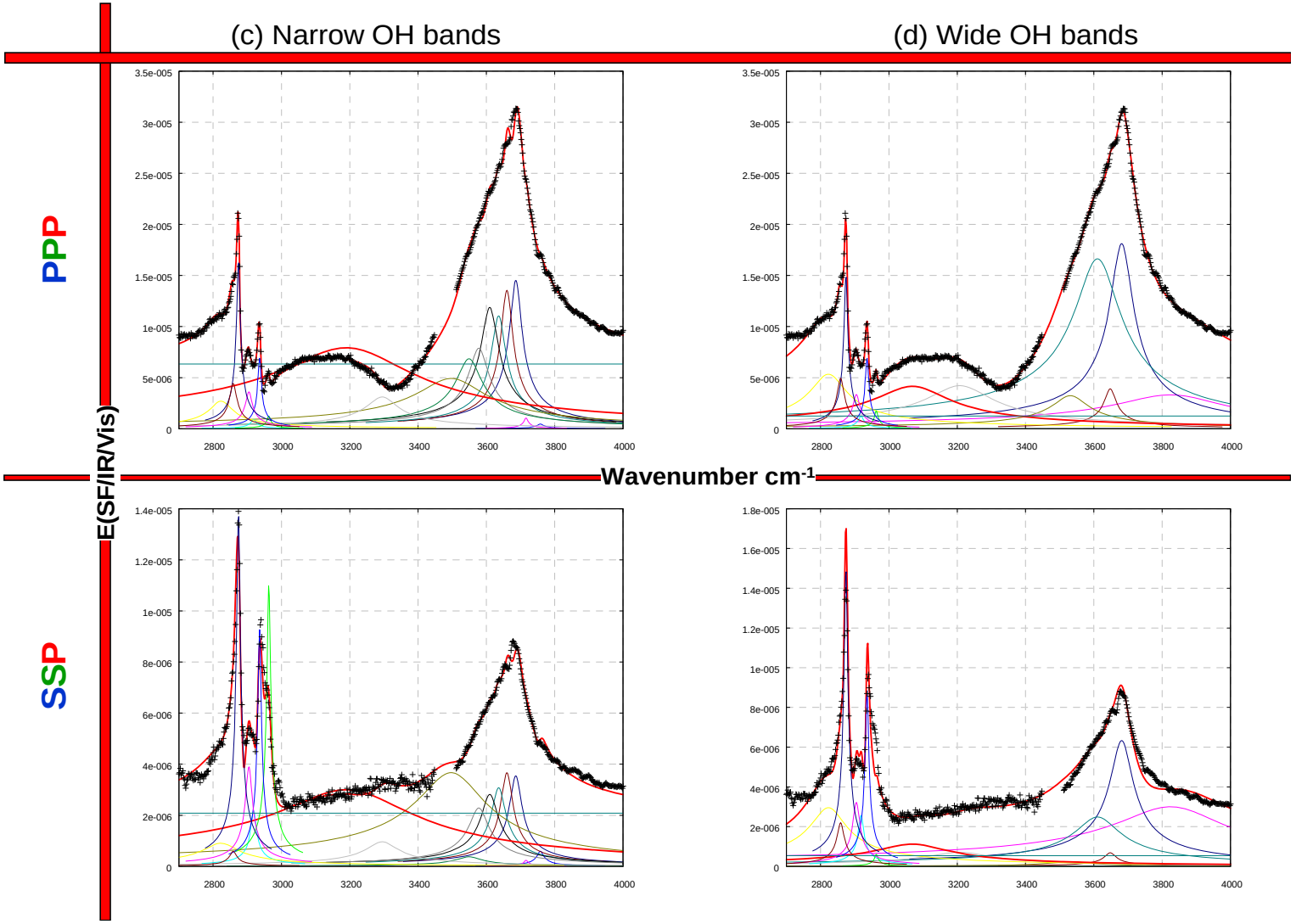

Figure 3-5 Continued

3.2.1.1 CH band assignment of butanol:

Prior to evaluating the SFG spectra of the butanol-water/sapphire interface, the spectra of the neat butanol/sapphire interface were analyzed. The neat butanol/sapphire SSP and PPP spectra, Figure 3-6 a and b, could be fitted with six individual peaks: the CH_2-SS at 2865cm^{-1}, the CH_3-SS at 2875cm^{-1}, CH_2-AS at 2898cm^{-1}, CH_2-FR at 2916cm^{-1}, CH_3-FR at 2938cm^{-1} and CH_3-AS at 2964cm^{-1}. These values are consistent with those found in the literature [45, 62] particularly for butanol-water mixture/air interface [63].

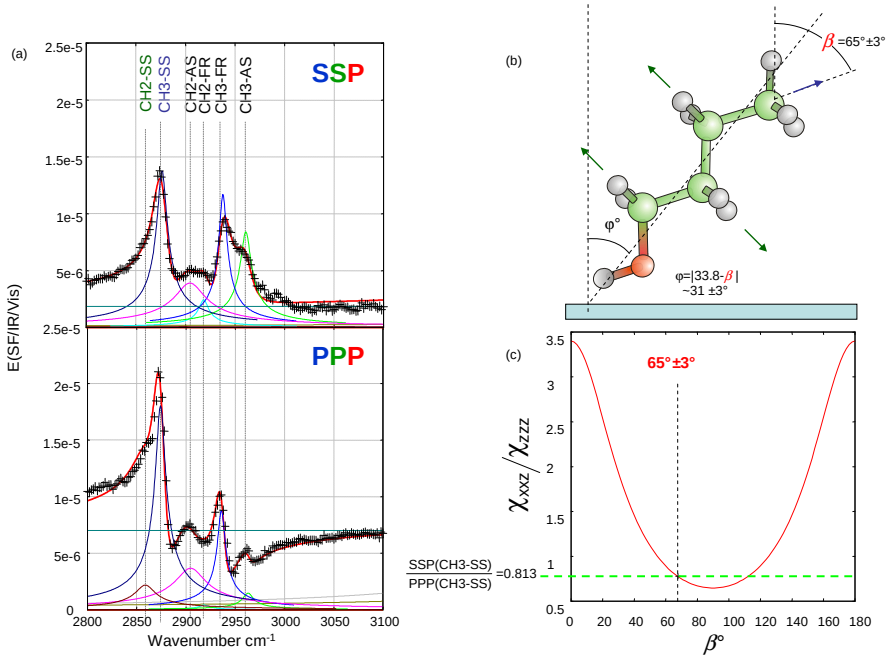

Figure 3-6 (a) SSP and PPP SFG spectra of the CH stretching region of the neat butanol/sapphire interface. (b) Scheme representing the expected orientation of the butanol molecule on the surface. (c) Determination of methyl group orientation angle as described in section (1.5.3)

The polar angle of the methyl group with respect to the surface normal was found to be ~65±3°, which corresponds to a tilt angle of the methylene chain of 31±3° with respect to the surface normal calculated as described in section (1.5.3). Due to the odd number of methylene groups, the net contribution of their stretching vibrations do not vanish and hence appear in the SFG spectrum as a small shoulder to the left of the CH_3-SS peak, which is the most important peak for determining the molecular orientation. The ±3° error contains the influence of the high wavenumbers part of the spectrum. So far so good, what about the rest?

3.2.1.2 The full spectra of the butanol-water mixture/sapphire-001 interface

As seen in the previous section, the parameters of the narrow CH bands are only weakly dependent on the interference with the broad OH bands at high wavenumbers. This advantage will be utilized now for the fitting of the spectra obtained from butanol and butanol-water mixtures at the sapphire interface in the entire spectral range measured including the high wavenumbers region. The fitting procedure will begin by using the results of the six well defined CH bands, including their positions, widths, and amplitudes, as determined in the previous section. Also, the orientation of the CH_3-SS vibration will be used as a reference for the phase of the SFG signal (which determines the polar orientation) to evaluate the orientations of other species. This reasonable starting point allows to state whether the different species contributing to the overall SFG signal are water, butanol and/or surface hydroxyls. It is worth to mention here that; although the influence of assuming different models at the high wavenumber region on the CH band parameters is small, but it is not enough to allow changing the sign of the bands (assuming wrong band signs leads to entirely physically meaningless fitting results, see section 2.6.3 data fitting). The definition will be as follows: +ve sign means a net transition dipole moment pointing away from the surface ($\varphi < 90°$) and –ve sign means a net dipole moment pointing toward the surface ($\varphi > 90°$). This definition relies on the fact that for enthalpic reasons, the non-polar methyl group of the butanol should not be oriented towards the polar sapphire surface. This would even be expected in the case that a water layer (polar) had been already present on the surface prior to the addition of water in the later experiments.

Figure 3-7 shows the full PPP and SSP SFG spectra at the neat butanol/sapphire interface including the deconvoluted individual bands and the orientations of the corresponding transition dipole moments. The number of bands was determined on the following basis: an acceptable band should at least be either consistent with one published in the literature for water/sapphire, air/sapphire or air/water interfaces (see Table 3.1) or it should be a clearly distinguishable band appearing in SSP and/or PPP at a given concentration (e.g., the parameters of the band at 3385cm^{-1} were determined from the SSP spectrum at $X_B \approx 0.798$, while the parameters of the band at 3440cm^{-1} were determined from the SSP spectrum at the highest water concentration in this series of experiments, $X_B \approx 0.522$). The obtained collection of 14 bands, using this procedure, was found to fit the complete set of the 24 spectra collected from this series of experiments and shown in Figure 3-4, i.e. resulted in a

self-consistent analysis of the data. Table 3.1 lists the bands used, their assignments and their origin (i.e. from literature or features in spectra).

Surprisingly the band at 3678cm^{-1} (and also at 3625cm^{-1}) was found to have a –ve sign (i.e. oppositely oriented relative to the butanol chain). The band at 3678cm^{-1} is usually attributed to a dangling (free) OH in water/air interfaces [12, 18, 69, 70, 71] or a free aluminol group in the air/sapphire interfaces [43, 53]. Such a band can not be associated with aluminol groups in this case, since the dipole moment points toward the surface, leaving only two other options: either they come from an OH vibration of non-hydrogen bonded butanol molecules right on the surface or more probably from free OH of unsaturated hydrogen bonding water molecules close to the surface within the penetration depth of the incident light. This issue will be discussed in more details in the next sections.

In a recent study by Daum et al. (2008) [66], on the effect of surface nano-roughness of sapphire 001 on the molecular structure of a water/mineral interface, it was found that no vibrational bands were observed in the free OH region at the water/sapphire-001 interface of atomically smooth surfaces. On the other hand, such vibrations were observed from unannealed disordered surfaces with nanometer roughness. Annealing at high temperatures produces well-defined atomically flat terraces of step height and terrace width defined by the annealing conditions (temperature, time and rate of cooling). The annealing conditions were optimized to obtain flat terraces with uniform atomic steps and less miscut angle [72]). Typical values for the step height and the terrace width range from 0.2 to 2.8nm and from 70 to 350nm, respectively, corresponding to a temperature range of 1000 - 1500°C and annealing time of few minutes to several hours [72, 74]. These findings explain the free OH vibrations observed in the presented work distinctly. The sapphire samples used in the present work were not annealed, but either mechanically or chemically polished by the manufacturer as the last step of preparation, before being cleaned and used in the experiments. Polishing (particularly mechanical polishing) produces a highly disordered surface layer with a substantial amorphization [71]. This means that unannealed samples do not reflect a well defined single crystal surface. However, to proceed with the interpretation, one should understand the effect of this amorphization. A highly amorphous surface is a pored surface that contains isolated aluminol groups captured in nanopores cavities. These isolated non-regularly oriented aluminol groups can produce SFG signal at the free-OH region. Such pores can also capture water molecules with unsaturated H-bonding, which in turn can also produce

signal in the free-OH region. This explains the unexpected –ve sign in the spectra, which indicates a net dipole moment pointing toward the surface ($\varphi > 90°$).

A small band at frequency higher than 3720cm^{-1} was detected (the position is not well defined due to the weak contribution to the SFG signal and the relatively large width). However, this band is most probably arising from ion solvation close to the surface [75], where residual ions are expected at the surface after cleaning with pH12 (see sample cleaning, section 2.5). Anyway, this small band does not play any role in the following discussion.

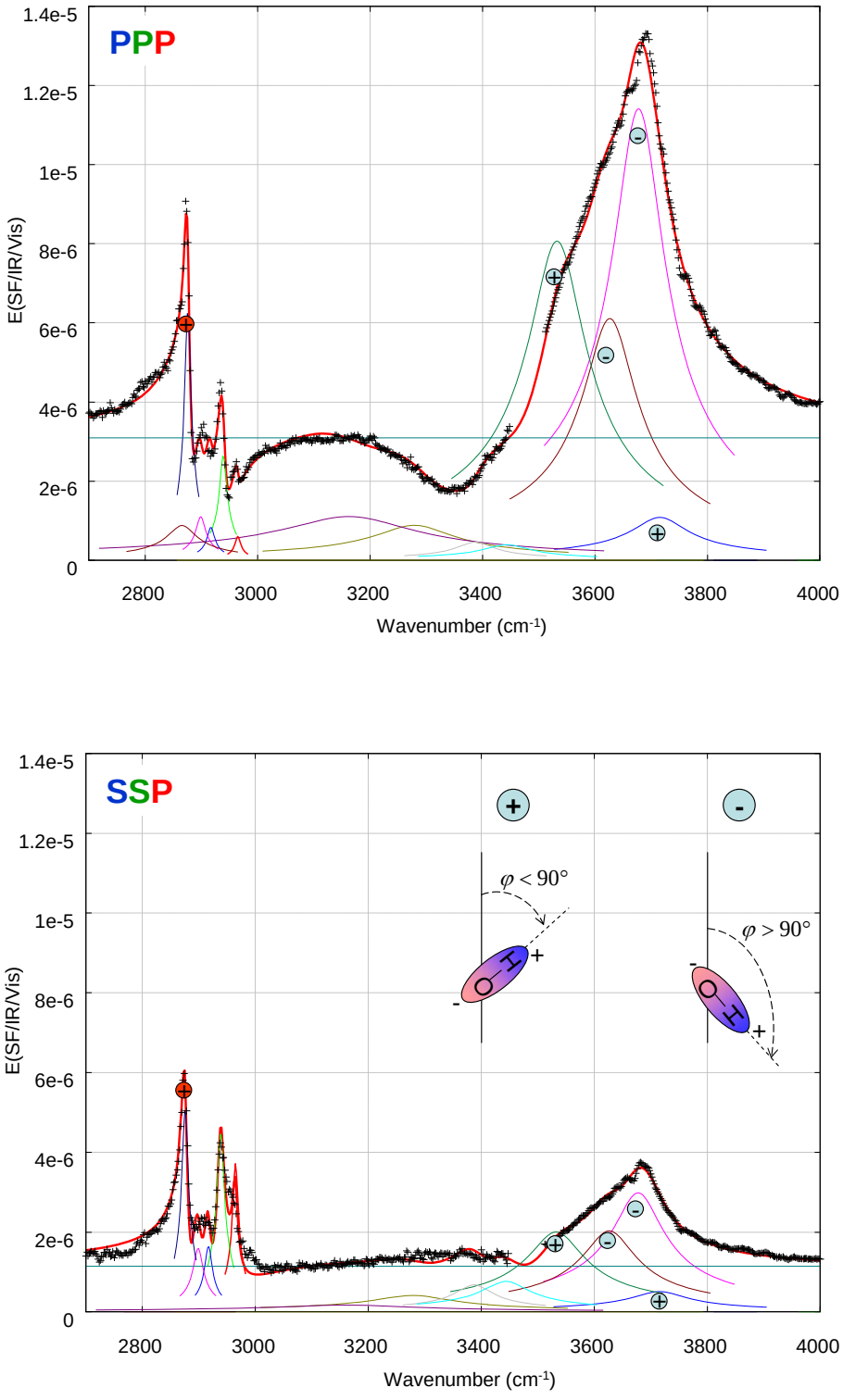

Figure 3-7 The full PPP and SSP SFG spectra at neat butanol/sapphire interface including the deconvoluted individual bands. The phases of the important individual species contribute to the individual bands are displayed as +ve and –ve signs for net dipoles pointing away from ($\varphi < 90°$) or toward ($\varphi > 90°$) the surface respectively.

Band no.	Central peak cm^{-1} (Average Value)	FWHM	Assignment	Origin (Source)
OH Vibrations				
1	3716 ±10	95	Solvation due to residual ions	[75] vapour/water
2	3672 ±30	85	Free OH stretching vib. of dangling O-H from the water to vapour phase	[75, 78] vapour/water
			Free OH stretching vib. of surface hydroxyl groups (aluminol groups)	[66] water/sapphire
			The dangling OH (surface free OH) stretch of water molecules that straddle the interface with one non-hydrogen-bonded OH directed into the air phase32,34,35 and the other OH interacting through hydrogen bonding with the liquid phase	[69] air/water
			Free OH stretching vib. of surface hydroxyl groups (aluminol groups)	[53] air/sapphire
3	3627 ±10	89	Butanol-OH vibrations of non-associated (or monomer) molecules	[60] monomers
4	3538 ±20	95	OH stretching vib. from weakly hydrogen bonded aluminol groups	[66] water/sapphire
			The modes associated with three-coordinate asymmetrically hydrogen-bonded water molecules in which one O-H bond is involved in strong hydrogen bonding and the other is only weakly hydrogen-bonded	[69] air/water
5	3444 ±10	80	Donor OH	[75] vapour/water
			OH-SS of tetrahedrally coordinated water molecules	[66] water/sapphire
			Uncoupled donor OH mode	[78] vapour/water
			Asymmetrically oscillating dipoles from four-coordinate hydrogen-bonded water molecules or arising from four-coordinate water molecules where one hydrogen is a poor hydrogen bond donor.	[69] air/water
			Structurally disordered water	[64] water/sapphire
			This band is clearly distinguished band at $X_B \approx 0.52$ in the SSP spectrum	
6	3388	64	New observed band. This band can be assigned, in this study, to OH vibrations from water molecules H-bonded to the butanol molecules close to the surface.	Clearly distinguished band at $X_B \approx 0.93$ in the SSP spectrum
7	3292 ±30	136	Water-like water band	[75] vapour/water
			Tetrahedrally coordinated H_2O molecules in the interfacial region	[78] vapour/water
			At 3250cm-1, vibrational modes from four oscillating dipoles of four-coordinate hydrogen-bonded water molecules	[69] air/water
			Structurally ordered water	[64] water/sapphire
8	3168 ±30	225	Ice-like water band	[75] vapour/water
			Tetrahedrally coordinated H_2O molecules in the interfacial region	[78] vapour/water
			OH-SS of tetrahedrally coordinated water molecules	[66] water/sapphire
			At 3200 cm-1, three coordinate water molecules at the surface that are single-protondonor-double-proton-acceptor (DAA)	[69] air/water
CH Vibrations (central peak position was chosen at the neat-butanol/sapphire experiment)				
9	2964 ±5	10	CH_3-AS	[45, 62, 63]
10	2938 ±5	12	CH_3-FR	
11	2916 ±5	12	CH_2-FR	
12	2898 ±5	16	CH_2-AS	
13	2875 ±5	10	CH_3-SS	
14	2865 ±15	50	CH_2-SS	

Table 3.1 A list of the individual bands deconvoluted from the Butanol-water mixture/sapphire interface experiments, their assignments and whether they were estimated from the literature and/or found as clearly distinguishable bands at certain concentration and polarization combination.

3.2.1.3 Data fitting and species behaviour

In the following analysis, only the well-resolved bands will be traced. Well resolved bands are the bands which have sufficiently high strength and considerably defined orientation either semi-parallel or semi-perpendicular to the surface. When any band becomes weak at a certain bulk composition for a given polarization combination, it will be excluded from the interpretation. For the peaks with very small contributions the position was held constant during the fitting process. Referring to Figure 1-15 in section (1.5.3), for OH species, the lower the ratio $R(OH) = |SSP_{OH}| / |PPP_{OH}|$ than unity, the more parallel oriented are the species with respect to the surface normal (perpendicular to the surface plane). On the other hand for CH_3-SS bands, the higher the ratio $R(CH_3 - SS) = |SSP_{CH_3-SS}| / |PPP_{CH_3-SS}|$ than unity, the steeper are the butanol molecules. If a fitted band was found to have a peak sign in the SSP spectrum different from that in the PPP spectrum, then the sign of the stronger peak was chosen. To be able to trace the changes in peak strengths and to interpret these changes altogether, the following logic table was constructed.

|Pol. set1|	**|Pol. set2|**	**|SSP|/|PPP|**	**Interpretation**
↑	↑	—	**The amount of species contributing to the signal increases while orientation is fixed**
↑	↑	↑↓	**The amount of species contributing to the signal increases and the orientation changes**
↑	↓	—	**The total amount of species contributing to the signal changes while the orientation is fixed**
↑	↓	↑↓	**Species change orientation and <u>maybe</u> amount**
↑	—	—	**Not possible**
↑	—	↑↓	**The amount of species contributing to the signal increases and the orientation changes.**
↓	↓	—	**The amount of species contributing to the signal decreases while orientation is fixed**
↓	↓	↑↓	**The amount of species contributing to the signal increases and the orientation changes**

Table 3.2 : Logic table used to interpret the changes in the butanol-water mixture/sapphire experiments. |Pol. set| means SSP or PPP polarization set. *↑: Increase, ↓: Decrease, ↑↓: Change, —: Constant*

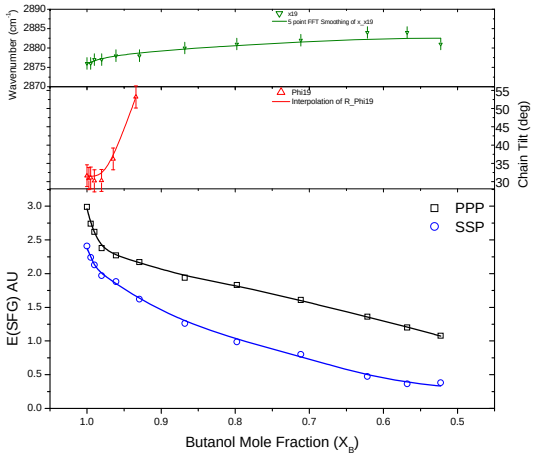

(a) ~2880 cm^{-1} (CH_3-SS)

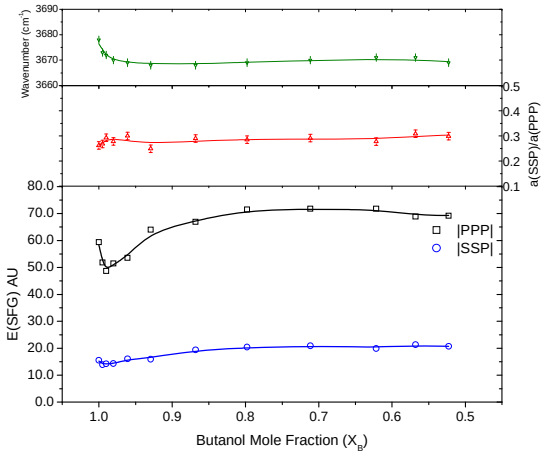

(b) ~3680 cm^{-1}

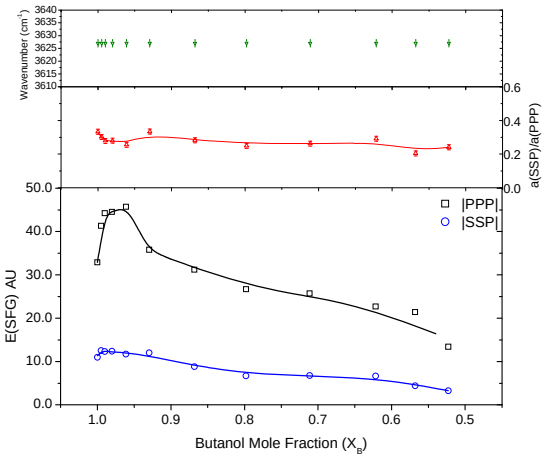

(c) ~3625 cm^{-1}

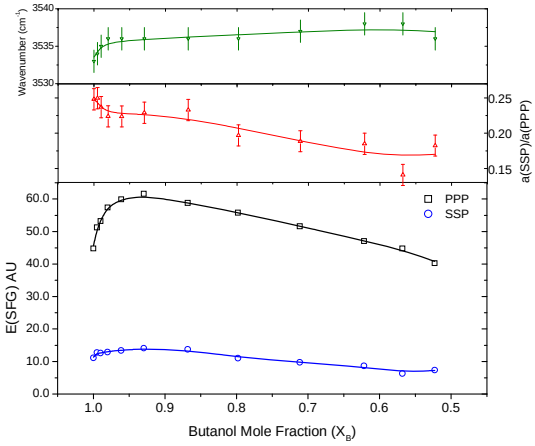

(d) ~3535 cm^{-1}

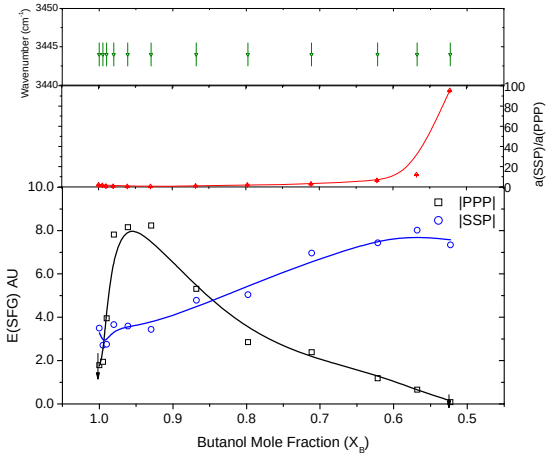

(e) ~3440 cm^{-1}

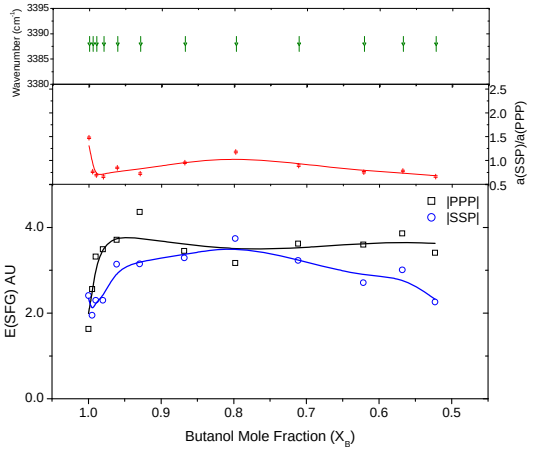

(f) ~3385 cm^{-1}

Figure 3-8 The evolution of the peak positions, amplitudes and SSP/PPP ratios for the most important bands in dependence of the butanol mole fraction of the butanol/water mixture. For the butanol CH_3-SS, the ratio is replaced by the net orientation of the molecule chain.

Figure 3-8 shows the behaviour of the most interesting peaks with clearly discernible features in the SFG spectra. Each plot contains three types of extracted information; the peak amplitude, the peak position and the ratio $|SSP|/|PPP|$ (only for the butanol CH_3-SS, the ratio is replaced by the tilt angle of the methylene chain). In the cases where the amplitudes were negative, absolute values are shown. All relations found confirm the inversion point mentioned in the beginning of this section. Spectral changes occur at the surface as a result of only slight changes in the fractional amount of water. Noticeable changes could be observed already from the first drop of water. At $X_B \approx 0.995$, which corresponds to a tiny amount of water ($X_w \approx 0.005$) in the bulk (~100mL butanol), the SFG field of the butanol CH_3-SS vibration dropped by about 8% in PPP and 7% in SSP. This indicates that the surface affinity to water molecules is much higher than that to butanol molecules. The inversion point is found at a mole fraction of butanol of $X_B \approx 0.96 - 0.93$, which still corresponds to small amounts of water in the bulk. To understand the underlying mechanism of this behaviour, we will study each case separately and then fuse the individual results to obtain a plausible final interpretation;

(a) Figure 3-8a, CH_3-SS (~2880cm^{-1}): +ve

This band is known to be the symmetric stretching vibration of the methyl group [45, 62]. It was observed, recently by Allen et al. [63], in a similar system of a water-butanol-mixture but at the air/liquid interface. As mentioned previously, the CH_3-SS is the reference for the relative orientations of the different molecular transition dipole moments and the probe on the behaviour of interfacial butanol molecules upon addition of water. From $X_B = 1$ to $X_B = 0.96$ the amount of species contributing to the SFG spectra decreased, while the net orientation remained constant. Referring to the logic table, this can be explained in terms of butanol molecules leaving the surface region, for example because interactions with the incoming water. Beyond the inversion point (i.e. $X_B < 0.96$), the amount of species contributing to the SFG signal continues to decrease and the molecules start to disorder. This disorder results from the freely rotating, or moving in general, molecules at low butanol concentrations on the surface. This would be expected since the butanol chains are not densely packed any more and thus have more freedom to change their conformation as well as their orientation, thereby averaging out the SFG signal. Also, the observed blue shift in the

peak position means that the inter-chain interaction decreases because of less dense packing as we observe here. Thus, the blue shift is in line with the decrease of the SFG signal.

(b) Figure 3-8b, (~3680cm^{-1}): -ve

This band is usually attributed to the free-dangling OH from water [12,18,69,70,71] or from hydroxylated surfaces [43,53], depending on the surface under study. In the present case, however, this band has a –ve sign (i.e. opposite net dipole moment relative to that of the methyl group), which can not be explained by surface hydroxyl species. At the moment this sounds a bit strange because there is no water/air interface present in this system to allow OH dangling from the water surface into air. To explain this, a series of complementary experiments were done, which will be discussed in sections 3.2.2 - 3.2.5, and together with some results published on water/sapphire interface [66, 26], it was found that it is possible to obtain such a signal at this interface. The SFG experiment, which was carried out at chloroform/sapphire interface in the presence of small amount of ethanol, showed the same result (i.e. OH vibration at 3690cm^{-1} of a net dipole moment oriented opposite relative to that of the methyl group of the ethanol). The experiment of propionic acid vapour gave the same result, although with some reservations, which will be discussed later. The contact angle measurements showed that the surface is always hydrophilic which means that the surface adsorbs water molecules likely. From *Molecular Dynamics* studies and *Quantum Chemical theory* [67, 68] it is known that the amount of hydroxyl species/cluster on sapphire (15/cluster) is smaller than the amount of water molecules, which can occupy the same area of the surface (20/cluster). This means that, even in the case of the neat water/sapphire interface, there is an excess number of unsaturated water molecules in the vicinity of the surface, which are exposed to the surface electric field within the penetration depth of the incident beams. The orientation of these molecules is influenced by the surface charge.

Inspecting Figure 3-8b and referring to the logic table, the entire process can be divided into three different phases: before the inversion point (first phase), the amount of species contributing to this band decreased with a slight change in the net orientation and the band blue shifted indicating a less dense packing of the surface moieties. This is an indication of species exchange and reduced H-bonding. Then, in the second phase, the trend (of the signal amplitudes change) was inverted after the inversion point without further blue, or red,

shift. In the third phase ($X_B > 0.67$), no significant changes in the trend of the signal amplitudes were observed.

(c) Figure 3-8c, (~3625cm^{-1}): -ve

This band has also three phases of evolution. During the first two phases, it approximately behaves opposite to the one at ~3680cm^{-1}. In the third phase it showed a continuous decrease of the amount of species contributing to the SFG signal with the addition of water until the last concentration ($X_B = 0.522$) used in this series of measurements. The counter behaviour of this band with respect to that of the ~3680cm^{-1} band in the first two phases indicates a possibility of species exchange between two different OH groups. Another possibility is that it corresponds to the OH vibration of the butanol molecules at the surface, since it is negative and vanishes with the addition of water. In fact, the second possibility is more probable as it agrees with the published band positions [60] for butanol-OH vibrations of non-associated (or monomer) molecules, see Table 3.1.

(d) Figure 3-8d, (~3535cm^{-1}): +ve

In the literature, this band is assigned to water molecules of three asymmetric H-bonding coordinations [69]. One O-H of the water molecule is involved in a strong H-bonding and the other is weakly H-bonded. In the present work it was found that the species (weakly H-bonded) contributing to this band are continuously disordering with adding water, decreasing after the inversion point and reducing their number of H-bonds before the inversion point. Probably there was an exchange between those species, which produce this band, and others, which do not. A final conclusion on this behaviour, however, will be given in the discussion later on.

(e) Figure 3-8e, (~3440cm^{-1}):

This band has different assignments in the literature for different systems, see Table 3.1. At air/water interface, this band usually assigned to asymmetrically oscillating dipoles from four-coordinate hydrogen-bonded water molecules or arising from four coordinate water molecules where one hydrogen is a poor hydrogen bond donor, [69]. At the air/hydroxide

interface, the resonances are usually considered as bands arising from in-plane species which lie more or less parallel to the surface, [26]. The corresponding feature of this band in the spectrum becomes very distinguished in the SSP signal at high water concentrations, which outweighs the assumption that they arise from water, which is typically lies in this frequency range. This assumption, i.e. to be a water band, agrees with the assignment of Yegane et al. on the water/sapphire system [64].

(f) Figure 3-8f, (~3385cm^{-1}):

The peak at 3385cm^{-1} is a new feature, not found in the literature, which could be observed only due to the grace of the tiny stepwise addition of water. Otherwise it might have been considered as one broadband covering both the bands at 3385cm^{-1} and 3440cm^{-1}, respectively. A direct comparison of the SSP spectra obtained from $X_B = 0.522$ with those from neat water/sapphire interface in this region shows that this peak is a characteristic feature of the presence of butanol, Figure 3-9. Therefore, this band can be assigned to OH vibrations from water molecules H-bonded to the butanol molecules close to the surface.

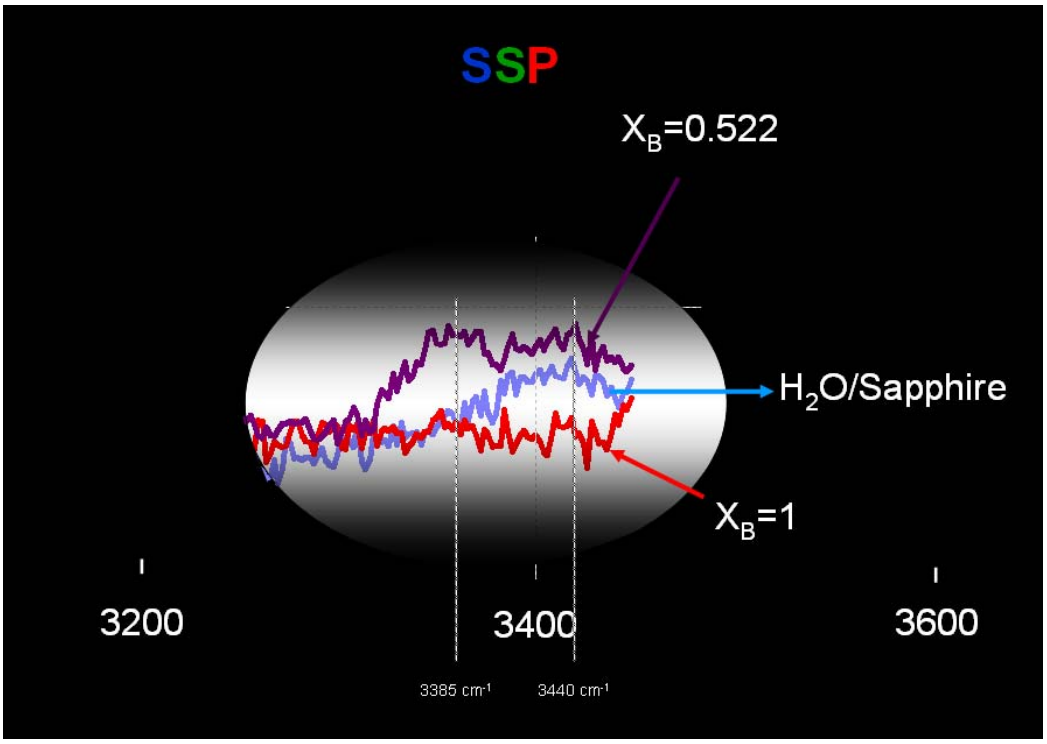

Figure 3-9 A direct comparison between the SSP-SFG spectra at neat butanol, neat water and butanol-water mixture /sapphire interfaces.

3.2.1.4 Final conclusion on butanol data:

The strong response of the spectra to the tiny amount of water ($X_w = 0.005$)added to the bulk butanol at the beginning of the experiment, the 0.05% residual water in the neat butanol used and the fact that the sample was rinsed with water at the end of the cleaning procedure strongly suggests that the experiment was started with a butanol-water mixture/sapphire interface and not the neat butanol/sapphire interface. This agrees with the presence of water bands (at 3281^{-1} and $3167cm^{-1}$, Figure 3-7) in the SFG spectra which correspond to $X_B = 1$ bulk mole fraction. Thus at least a monolayer of water which has preferential orientation should be expected on the hydroxylated sapphire surface.

The adsorption-desorption mechanism of the water-butanol mixture at the sapphire surface during the addition of water to the initially neat butanol can be divided into three phases upon the trend of the signal strength of the OH vibrations, (1-before, 2-after and 3-far after the inversion point). In the first phase of the water addition sequence (before the inversion point), the decrease in the signal from the butanol agrees with the assumption that the additional water molecules compete with the butanol at the interface and contribute to the OH SFG vibrational signal. The fast simultaneous increase in the SSP and PPP signals for any OH species on the addition of water before the inversion point can be understood as an increase in the amount of species (water molecules) contributing to the signal. The question is then what happens in the second phase after adding further water (beyond the inversion point)? If it is not a reorientation of water species, it should be either disordering as a result of interruption by the incoming water molecules or a formation of a new water layer with a net dipole moment that interferes destructively with that of the former water layer, which is more or less the same effect. Thus, it is reasonable to understand how the inversion point can be caused by adding even a small amount of water (0.8mL) to the bulk butanol (100mL), corresponding to water mole fraction of $X_w = 0.034$. In the third phase, the adsorbed water layers extended into the bulk liquid and the butanol molecules became highly disordered.

It is worth to note that adding further water beyond the inversion point lowers the butanol contribution, but it should not necessarily give rise to another frank inversion point. This, however, is what we see in the relations shown in Figure 3-8. One explanation for this a priori unexpected behaviour is that at a certain water mole fraction, the total water layer will be thick enough to form bulk-like water within which the water molecules are saturated with

H-bonds. This replacement of butanol molecules by incoming water molecules increases the spacing between the chains of the still existing butanol molecules, which explains the high butanol disordering observed right beyond the inversion point.

3.2.2 SFG at Ethanol Liquid and Vapour/Sapphire-001 Interface

This experiment was carried out as an independent proof of the existence of a water layer at the liquid/sapphire interface, which produces a signal in the free OH region. The adsorption of ethanol was studied by SFG at the chloroform/sapphire interface by adding trace amounts of ethanol to the liquid phase. This system was chosen because it may be assumed that the ethanol will aggregate at the chloroform/sapphire interface in an ordered fashion driven by two complementary forces. This assumption relies on three facts; first, the ethanol is of dual, i.e. amphiphilic, nature, (it has a hydrophobic part at one end and a hydrophilic at the other), second, chloroform is hydrophobic and third, sapphire is hydrophilic (polar). Under these conditions, the ethanol molecules will preferably assemble such that the methyl group is oriented toward the chloroform bulk solution and the OH is oriented toward the sapphire surface (or the water film at the sapphire surface, if exists), thereby minimizing the free enthalpy of the interface. Figure 3-10 shows the result of this experiment. In fact, CH vibrations of ethanol can be identified, from left to right, at 2845cm^{-1}, 2874cm^{-1}, 2929cm^{-1} and 2977cm^{-1}, which may be assigned to CH_2-SS, CH_3-SS, CH_3-FR and CH_3-AS, respectively [45]. Given the high sensitivity of SFG to the violation of inversion symmetry in a system, this observation indicates that the ethanol is not only present at the interface, but in fact exhibits preferential orientation. The highest vibration, at 3016cm^{-1}, corresponds to the CH vibration of the chloroform [76]. To confirm these assignments, a comparison was made between the ethanol bands given above and those obtained at the ethanol vapour/sapphire interface in the CH region, Figure 3-11. At the vapour/sapphire interface, the ethanol layer was assumed to form a monolayer, because the vapour experiment was carried under an ethanol partial vapour pressure of below 0.5 of the saturated vapour pressure of the ethanol, which is known to be the condition for formation of a monolayer in this system [45].

The comparison shows that the ethanol bands of above liquid phase experiment are 11cm^{-1} red shifted relative to those observed in the vapour phase experiment. This is reasonable since the ethanol molecules in the first case have higher packing density and thus stronger intermolecular interaction which cause red shift. However, 11cm^{-1} shift is a lot which indicates an additional effect from the chloroform. This is also reasonable since the ethanol molecules in the first case are stretched between the two media because they undergo H-bonding from the surface side and hydrophobic interactions with the chloroform from the bulk side. The average tilt angle of the ethanol chain was calculated and found to be ~33°,

which should be oriented such that it points away (+ve) from the sapphire surface due to the hydrophobic effect of the methyl group.

The fitting of the SSP and PPP SFG spectra obtained from ethanol adsorbed to the chloroform/sapphire interface gave results for the deconvoluted bands in a good agreement with the interpretation of the data obtained for the butanol-water/sapphire interface. As seen in Figure 3-10 there are +ve and –ve bands in the high OH region confirming the presence of OH species with dipole moments pointing up and down which can not be generated by sapphire hydroxyl groups alone. In addition, the presence of the ice-like water band at 3166cm^{-1} indicates a pre-existence of a water layer at the surface as concluded also from the butanol/sapphire results, see subsection (3.2.1.4). All these results obtained from the ethanol adsorption experiments are consistent with those found for the butanol-water mixture.

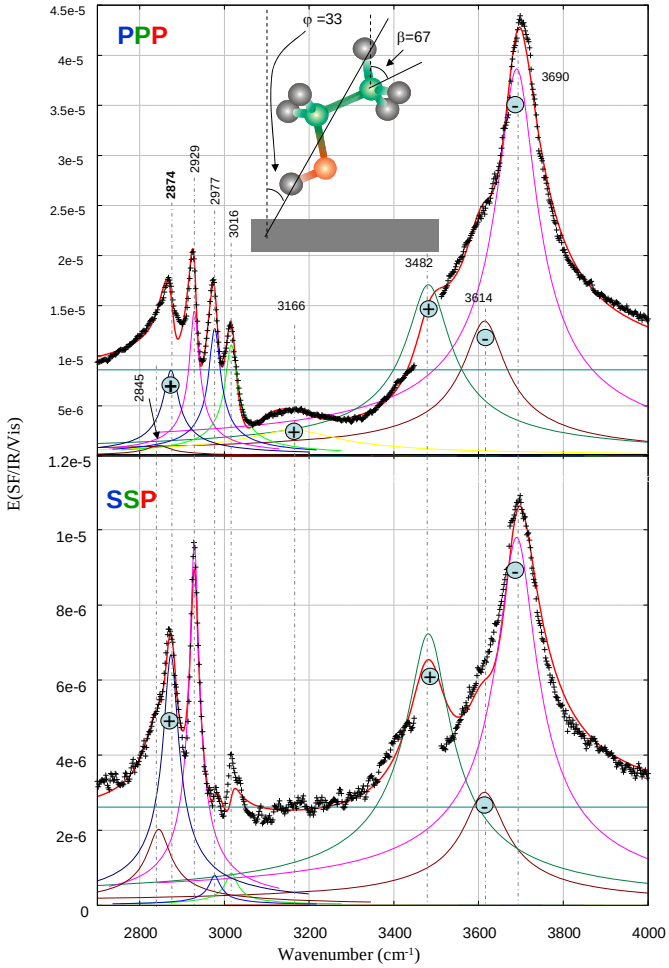

Figure 3-10 SFG at the chloroform (+0.6% ethanol)/ sapphire interface

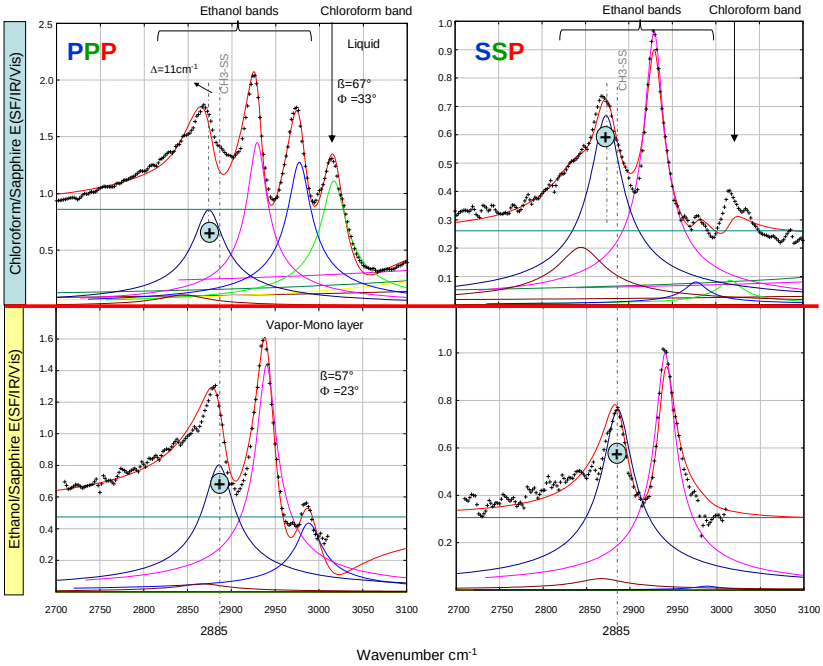

Figure 3-11 Comparison between SFG at (chloroform + 0.6% ethanol)/sapphire and (monolayer-ethanol vapour)/ sapphire interfaces in the CH vibrational region

3.2.3 SFG at Propionic Acid Vapour/Sapphire-001 Interface

Another experiment that was performed to corroborate the findings for the butanol-water/sapphire interface was to study the propionic acid vapour/sapphire-001 interface system. Although this experiment shows both up and down net dipole moments in the OH vibrational region (see Figure 3-12) which is in agreement with the findings on the butanol-water mixture/sapphire and chloroform-ethanol/sapphire interfaces, it cannot be used as strong argument that some of these OH vibrations arise from down pointing species of the water layer at the water/sapphire interface, because this system is a bit complex. It describes two interfaces, (air)/(propionic acid + water layer)/(sapphire) interfaces which makes the judgment on which interface produce contributes to what part of the SFG signal difficult. Despite of these intricacies, this experiment shows how the propionic acid interacts with the sapphire surface under the given conditions on the molecular level. Systems of this kind are a centre of global interest in understanding the interactions between humic substances and carboxylic acids with mineral oxides in the presence of water. Humic substances are frequently considered to contain carboxylic and phenolic functional groups [42]. Although it may be an oversimplification of the problem, it should yield some insight to begin the study with a separate analysis of the interactions of carboxylic and phenolic groups, respectively, and compare the outcome of this with a substance containing both carboxylic and a phenolic groups. Finally, this obtained results could be used for comparison with the behaviour of humic substances. From this point of view, the study of propionic acid was considered a very first step with an aim to demonstrate applicability and usefulness of SFG for this kind of investigation. Figure 3-12 shows the SFG spectra obtained for this system including the deconvoluted individual bands. As mentioned previously, it is difficult to tell which signal originates from which interface. However, the signs of the bands were determined from the fitted peaks of the PPP polarization set, particularly for those having a weak contribution to the SSP signal. The sign which yields a meaningful interpretation is that of the band associated with the tetrahedrally coordinated water (ice-like) molecules, at 3130cm^{-1} [66]. This band has a +ve sign, which is consistent with an uncharged (neutral) or positive surface, for example at low pH value for the electrolyte/sapphire interface [64] , where the surface is positively charged in the presence of an acidic medium. The region of the CH vibrations has three distinct peaks at 2900cm^{-1}, 2960cm^{-1} and 2990cm^{-1}, which can be assigned to CH_2-SS, CH_3-SS and CH_2-AS vibrations, respectively, of the propionic acid [61].

Figure 3-13 shows the effect of pumping water vapour into the measuring cell after adsorption of propionic acid on to the sapphire-001 surface from the vapour phase. Pumping the water vapour was done by reversing the cycling direction of the pumping cycle as described in section (2.3). The measuring cell, R2, was empty of liquids while the large reservoir, R1, was filled with M.Q. water. There is drastic reduction in the CH vibration bands accompanied with changes in the region of the OH vibrations. It seems that after exposing the propionic acid/sapphire interface to water vapour, the system changed into a monolayer of propionic acid adsorbed either directly to the surface OHs or to the water layer. In good agreement with this interpretation is the reduction in the OH vibration of the propionic acid (at ~3654cm-^{1}). As mentioned in the beginning of this section, it is difficult to assign the specific origin of the signal in this multi-interface system, so what information one can extract from it? If the area under the curve for each individual deconvoluted band corresponds to the relative amount of ordered species, then comparing these areas allows identifying concomitant changes and suggests the mechanism of adsorption and de-sorption of propionic acid molecules at the surface assuming that neither the orientation nor the order of the molecules changes. To do this, the differences between the areas under the curves ΔA after and before pumping water vapour was calculated for each individual deconvoluted band as summarized in Table 3.3. Since the responses of all OH groups will be similar from the second order hyperpolarizability tensor point of view and the free (or weakly H-bonded) OH vibration of the propionic acid was identified, ΔA for the OH vibrations will be compared directly. Also, the effect of the vibration strength on the area under the curve will be ignored since the peak positions are close to each other.

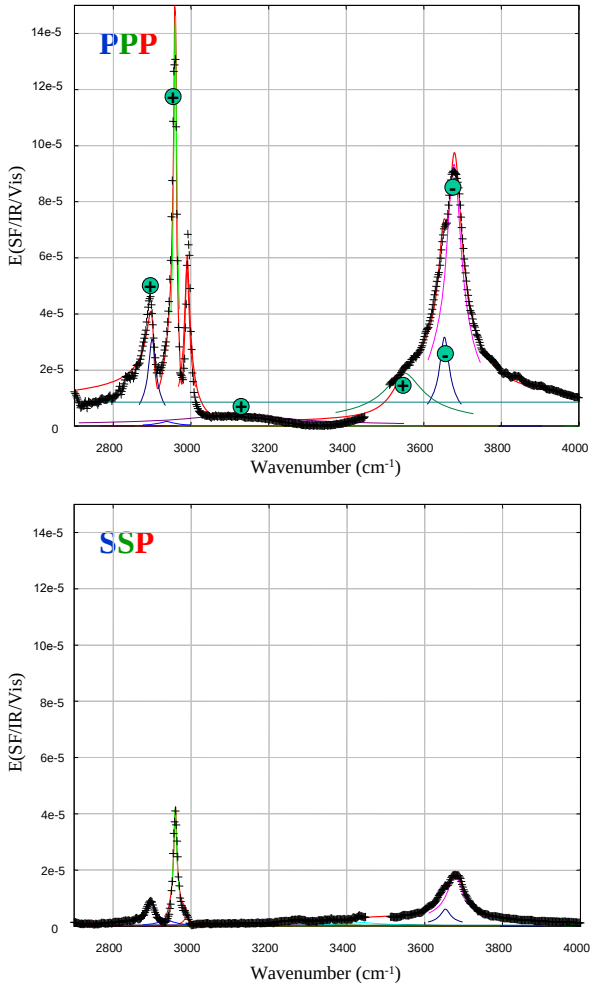

Figure 3-12 SFG at propionic acid vapour/ sapphire interface in the presence of saturated propionic acid vapour in equilibrium with its liquid phase.

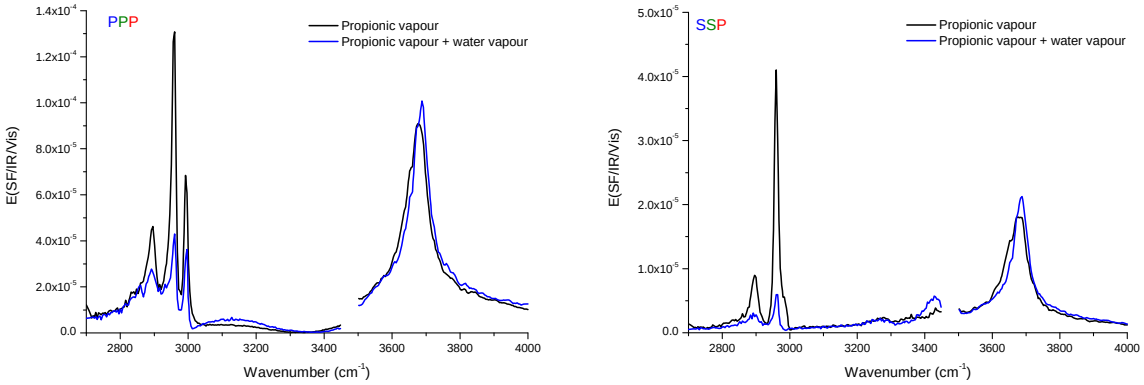

Figure 3-13 The effect of pumping water vapour into the measuring cell after adsorption of propionic acid.

Peak position (cm^{-1})	ΔA_{PPP} **(AU)**	ΔA_{SSP} **(AU)**	ΔA_{Total} **(AU)**
3679	**8.9**	**4.4**	**13.3**
3654	**-6.9**	**-5.8**	**-12.7**
3548	**-2.8**	**2.7**	**0.1**
3264	**(neglected)**	**-2.3**	**-2.3**
3125	**5.5**	**-3.7**	**1.8**
3439	**(neglected)**	**10.7**	**10.7**

Table 3.3 The differences in the areas under the curves for the individual OH vibrations between the SFG data of the systems (propionic vapour)/sapphire and (water + propionic vapour)/sapphire, respectively.

It is obvious from Table 3.3 that the first two bands are correlated. The increased amount of species (corresponding to 3679cm^{-1}) equals roughly the decreased amount of species (corresponding to 3679cm^{-1}). This supports the conclusion that the band at 3654cm^{-1} represents the OH vibration of the propionic acid and hence its decrease is a result of species exchange (incoming water molecules replace the adsorbed propionic acid molecules). The increase of the band at ~3440cm^{-1} simultaneously with that at 3679cm^{-1} is a sign that these two bands have more or less the same origin which is consistent with the interpretation of these two bands given by Richmond et al. [78]. Note that the band at 3440cm^{-1} was neglected in the fitting of the PPP spectra due to its very small contribution. This explains why its corresponding ΔA_{Total} is a bit smaller than that corresponding to 3679cm^{-1}. The band at 3548cm^{-1} shows a similar reduction in the PPP signal as an increase in the SSP signal, which can be interpreted as a reorientation of this type of most probably weakly H-bonded surface species. The water-like and the ice-like broadbands at 3264cm^{-1} and 3125cm^{-1}, respectively, also show a species interchange.

Further support for the interpretations given above concerning the OH vibrations is a comparison between the following four consecutive steps of starting with propionic vapour, pumping water vapour, pumping further water vapour, and finally pumping argon to reduce the adsorbed layers to the minimum possible thickness, Figure 3-14. The peak amplitudes vary as follows: (1) the 3679cm^{-1} and 3440cm^{-1} peaks are always correlated irrespective of whether they are decreasing or increasing; (2) the peaks at 3654cm^{-1} (and 2960^{-1}) are also correlated to each other but show an opposite behaviour with respect to the two former peaks. This confirms that the former two peaks originate from the same species (water) and the latter two peaks originate both from another species (propionic acid).

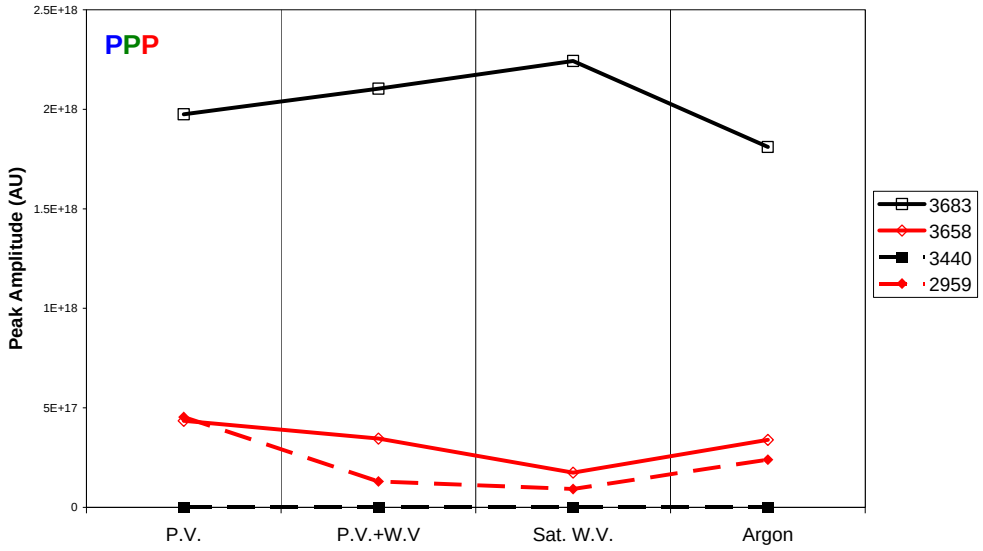

(a)

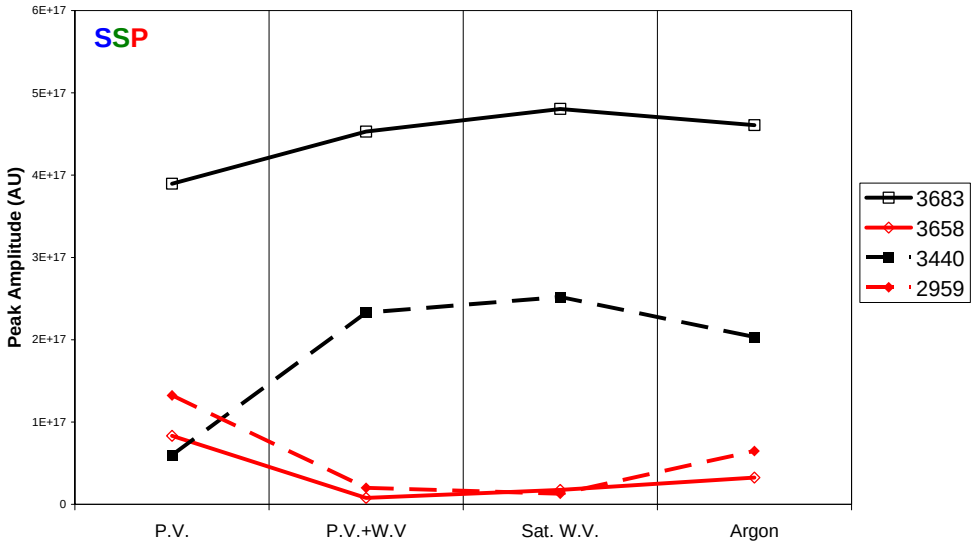

(b)

Figure 3-14 The change in the amplitudes of different bands upon changing the conditions. (P.V.: starting with propionic vapour, P.V.+W.V.: pumping water vapour, Sat. W.V.: pumping further water vapour and Argon: pumping argon). The displayed wavenumbers are the average values of the band position for each band over the four experiments.

3.2.4 Contact Angle measurements

A series of contact angle measurements have been carried out with the home-built CAMI described in section (2.8). All results showed that the sapphire surface is hydrophilic when rinsed with water (i.e. after different surface treatments, the surface appeared hydrophilic when wetted). The results of the contact angle measurements are summarized in the following table in dependence on the pre-treatment of the sample surface:

#	State	Contact Angle ±1	Remarks
1	**Recently polished sample**	**31°**	
2	**After H2SO4 (30min) → rinsed with MQ ware**	**4°**	**XPS measurements showed that the surface is sulfated**
3	**#2 → chloroform (30min) → rinsed with water**	**5°**	
4	**#3 → methanol (30min) → rinsed with water**	**10°**	
5	**#4 → fresh pH12 for 12hr → rinsed with water**	**14°**	**Recovered from the sulfate**
6	**#5 → butanol (30min) → rinsed with water**	**14°**	
7	**#6 → 1day old pH12 for 12hr → rinsed with water**	**25°**	
8	**#7 → UV (20min)**	**4°**	
9	**#8 → propionic acid vapor (60min)**	**17°**	**The adsorption takes place slowly**
10	**#9 → rinsed with water**	**7°**	
11	**#8 → propionic acid vapor (2 days) → rinsed with water**	**44°**	
12	**#11 → UV (20min)**	**4-5°**	

Table 3.4 A series of contact angle measurements showing the wettability of the sapphire surface after different cleaning processes and after exposure to some hydrocarbons.

It is obvious from the table that the surface did not adsorb sufficient amounts of hydrocarbons to become hydrophobic even in cases where it was not subsequently rinsed with water. However, the experiments from #9 to #12 indicate that adsorption of propionic might be a slow process, which was not completed within the time span of the experiment.

3.2.5 SFG at different media/Sapphire-110 Interface

In this section a preliminary SFG results from 110 surface in contact with different media are presented. These experiments appoint a start for a future work. However, they are discussed here qualitatively to collect new argument on some of the interpretations made from the sapphire-001 experiments discussed in this work. The preliminary results from the 110 surface in contact with water (or methanol) showed less signal strength at the free-OH if weighted against the water bands (or CH bands) compared to that from 001 surface of the water/sapphire (or methanol/sapphire) interface. Recalling that the amount of OH groups of the 110 surface (16.5/nm^2) is larger than the amount of those on the 001 surface (15/nm^2) [77,79] rules out the possibility that the signal at free-OH is exclusively from the surface hydroxyl groups. Thus it may come, with high contribution, from the adsorbed molecules which have extra bondless OHs that were reduced in the case of 110-surface. Figure 3-15 shows the SFG at water, methanol and ethanol/sapphire-110 interfaces in the CH and OH regions. The data are presented in intensity units and are not corrected to the Geometry Factors. Thus, a detailed analysis and a comparison of spectra are not feasible although the strong features in the individual spectra will not be considerably affected by these corrections and thus allow for a more qualitative discussion in the following.

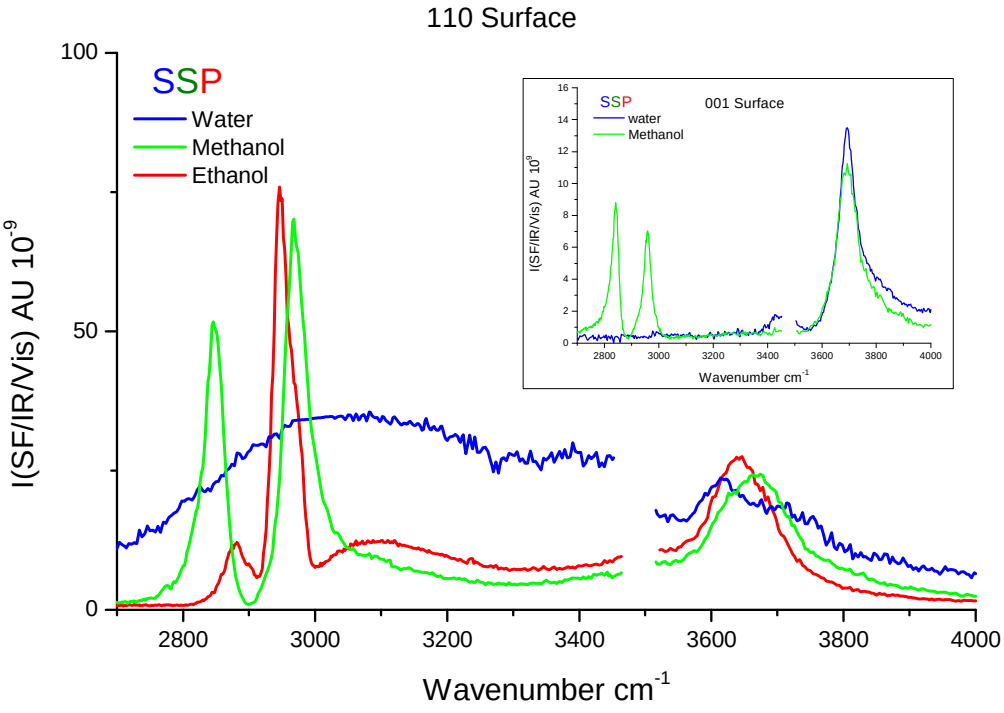

Figure 3-15 SSP-SFG at water, methanol and ethanol/sapphire-110 interfaces in the CH and OH regions, and (inset) the corresponding signals for water and methanol/sapphire-001 interfaces, (the data are corrected to the optical filters, but not to the Fresnel factors).

From a visual comparison of the SSP-SFG spectra at the water and methanol/sapphire-110 interfaces, respectively, with those at the respective water and methanol/sapphire-001 interfaces (inset), it is seen that for methanol the surface with higher density of hydroxyl groups (110) shows a lower OH/CH signal ratio than that obtained from the surface of lower density of hydroxyl groups (001). Similarly, for the water system, the 110 surface gives lower water-like and ice-like / free-OH ratios compared to the 001 surface. This suggests that the SFG generated at these interfaces in the high wavenumber region of the spectra depends on the amount of non H-bonded species from the liquid medium. Comparing the methanol, ethanol and water spectra, one can roughly say that the signal around 3700cm^{-1} appears to be dependent on the contact medium. However, discussing the details of these differences without correcting Geometry Factors is meaningless. This will be discussed in the future work Chapter 4.

Another example for the dependence of the high wavenumber OH signal on the medium is a comparison between the SFG spectra generated at a specific medium/sapphire interface for two different phases (liquid and gas). This is shown in Figure 3-16 where roughly speaking the signal at high wavenumbers (OH region) appears to depend on the phase of the medium, similarly behaves also the signal at low wavenumbers (CH region). This is expected if we consider the effect of mono- and multi-layer as well as the orientation of molecules in the second medium. Again, details will be shifted to the future work. Sometimes, in the multilayer system the secondary layers enhance or depress the generated SFG signal depending on the relative orientations and/or the randomization of the first layer as it perturbed by the next layer(s) [45].

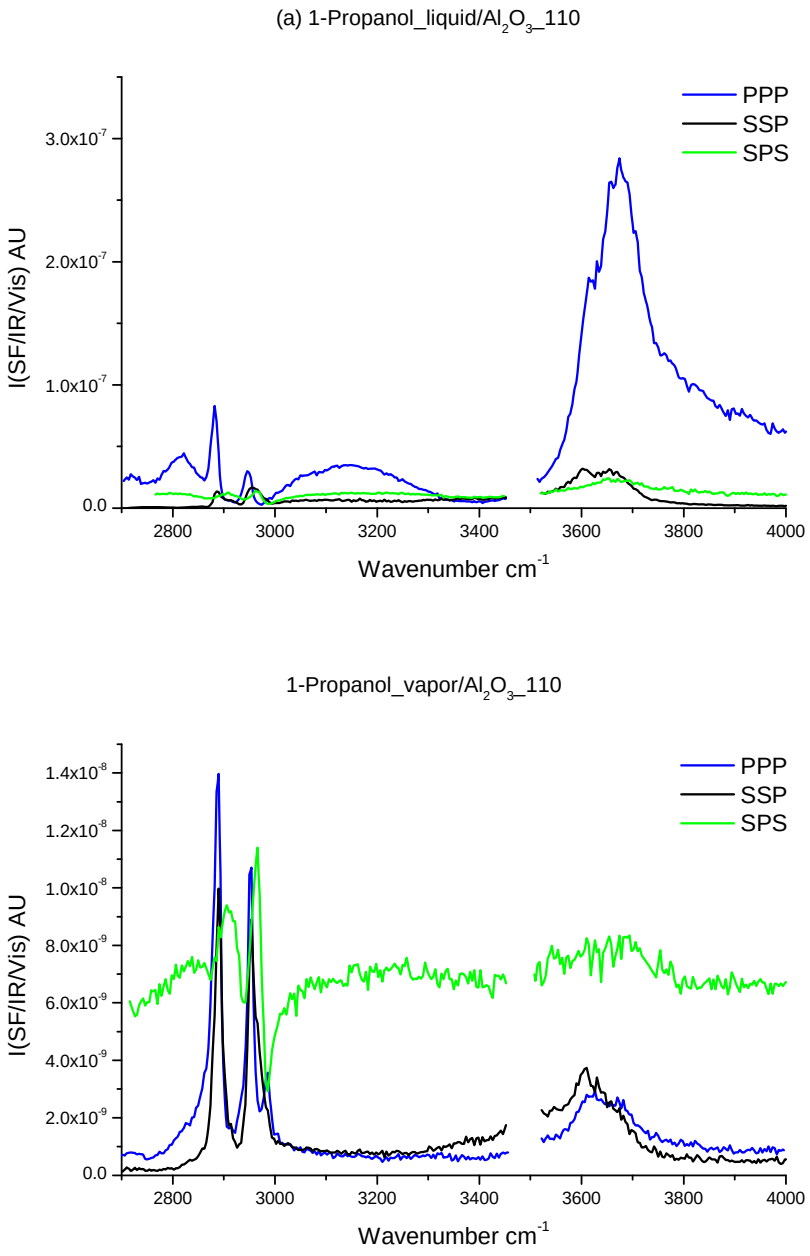

Figure 3-16 SFG in PPP, SSP and SPS polarization combinations at the 1-propanol/sapphire110 interface for (a) the liquid and (b) the vapour phase, respectively.

3.3 Summary

Linear and nonlinear optical techniques were applied in this work. The linear techniques (e.g. reflectivity at TIR, contact angle, XPS) were utilized to serve in the analysis of the results obtained by the nonlinear optical technique (SFG).

The liquid/solid and air/solid interfaces for some alcohols (methanol, ethanol, 1-propanal, 1-butanol and chloroform) and propionic acid vapor, as contact-media to the sapphire (α-Al_2O_3) surface, were investigated systematically using sum frequency generation spectroscopy in the CH and OH vibrational region (2500 – 4000 cm^{-1}). Two different crystal cuts (001 and 110) were analyzed. The focus of the study was on the interaction of 1-butanol with sapphire 001 surface in the presence of water as a step in understanding the mechanism of interaction between organic molecules and sapphire, as a model of natural clay minerals, in aquatic environment. The rest of studies on other contact-media were utilized to confirm and justify the interpretations extracted from butanol-water mixture experiments.

Reflectivity at TIR was conducted to investigate the linear optical properties (optical constants) of the used media. The obtained optical constants from methanol were compared to those published in the literature and found to be in a good agreement. The obtained optical constants of the other studied contact-media could not be found on the literature in the required spectral region (2500 – 4000 cm^{-1}).

Butanol interacts with the sapphire surface through H-bonding between the terminal OH of the butanol molecule and the aluminol groups and/or the strongly adsorbed water molecules on the sapphire surface. The affinity of the surface to the water molecules is much higher than to any of the contact-media presented in this study.

It was found that the sample preparation plays a major role in the results. The unannealed sample (like those used in this study) has an amorphous surface layer instead of a crystalline one. This amorphization gives rise to isolated aluminol groups and/or water molecules inside nanopores of the disordered surface layer. These isolated species were recognized by their vibrational SFG signal found in the free-OH vibrational region of the spectra.

3.4 Conclusions

Sum Frequency Generation (SFG) is a highly sensitive optical probe of surfaces and interfaces. The obtained signal depends strongly on the linear and nonlinear optical properties of the interface under study. Taking the linear optical properties, in the form of Fresnel Factors, into account resulted in a reasonable interpretation of the SFG spectra. It was found that the dependencies of the optical properties at the interface on the parameters of the incident laser beams and temperature are strong enough to influence the measured signal. The spectra were obtained in the spectral regions of the CH and OH stretching vibrations, ranging from 2500 – 4000 cm^{-1}. It could be shown that the interference between the narrow CH bands and the broad OH bands in the collected spectra is weak as long as the relative phases of the individual bands do not change, but, on the other hand, still sufficiently strong to allow the determination of molecular orientations of OH species on basis of the known orientation of molecular groups observable in the CH region of the SFG spectra

On this basis, the adsorption-desorption behavior of butanol onto the sapphire surface in an aquatic environment could be explained in terms of hydrogen bonding competition between the butanol and water molecules. The adsorption-desorption mechanism is controlled by the surface quality which explains the wide variety of results published on liquid/sapphire and air/sapphire interfaces as discussed within this work. It was found that the sapphire surface, prepared and cleaned as described in the experimental setup chapter, is not free of a strongly adsorbed and ordered water layer. The selected alcohol adsorbs directly to free surface hydroxyls and to the strongly adsorbed water molecules, thereby forming a densely packed and ordered structure. When adding water molecules to this configuration, the ordered densely packed butanol chains start to disorder and to be replaced by the incoming water molecules, which were thus found to have stronger affinity to the surface. The added water molecules start to take their place on the surface through hydrogen bonding, forming layer after layer. The interference between the different layers depends on their relative orientations, giving rise to either an increasing or decreasing SFG intensity. On this basis, the existence of an inversion point in the evolution of the spectral features in the SFG signals during the addition of water to the butanol-water mixture/sapphire interface confirms the build-up of such an ordered water structure. The adsorption-desorption mechanism of the water-butanol mixture at the sapphire surface is divided into three phases: 1- In the first phase, before the inversion point at $X_w = 0.034$, added water molecules compete with the

butanol molecules at the interface and contribute to the OH SFG vibrational signal. 2- In the second phase, beyond the inversion point, the formed water layer suffers reorientation of species and/or disordering as a result of interruption by incoming additional water molecules or the formation of a new water layer with a net dipole moment that interferes destructively with that of the former water layer. 3- In the third phase, the adsorbed water layers extended into the bulk liquid and the butanol molecules became highly disordered.

The preliminary data collected independently on other systems, mainly methanol, ethanol, 1-propanol, chloroform and propionic acid in contact with sapphire 001 and/or 110, confirmed the presence of a strongly adsorbed water layer on the sapphire surface with higher affinity to the surface than those selected molecules. Qualitative comparisons between the collected results on the 001 and 110 surface cuts showed that the signal originating from the free-OH vibrational mode is not arising solely from neither the surface hydroxyl groups nor the adsorbed species, but rather contains contributions from both types of species.

A dominant free OH vibration was found in all spectra, which is still under debate. It may either arise from non-hydrogen bonded surface hydroxyl groups captured in nano-pores present in the surface layer as a result of the polishing process, which was performed as a final step in the sample fabrication, or it is originating from non-hydrogen bonded species in the contact medium due to the unequal functional groups provided from both media at the interface. Further work is required to clarify, which of these two options, is the more likely one.

Altogether, the present work demonstrates that nonlinear optical vibrational spectroscopy can achieve new and very detailed insights into adsorption mechanisms and the mutual interactions present at the organic/sapphire interface, in particular in view of the role of surface-bound water. One of the keys to these findings was a proper theoretical treatment as well as experimental determination of the linear optical properties of the interfaces under study. Future work will have to take these effects into account. Further insight may be achieved by increasing the polarization combinations measured and by deuteration of selected species to allow a separation of resonances of different origin contributing to the same spectral region.

CHAPTER 4

FUTURE WORK

4. Future Work

4. Future Work

The future work will be discussed within two frames: 1) the continuation of the present study utilizing the obtained results and experiences as well as its extension to more complex adsorption systems, and 2) the utilization of other spectroscopic techniques, which were developed in the time course of this work.

4.1 Adsorption of organic compound on the solid minerals

The present study demonstrated the potential of combining linear and nonlinear techniques to investigate the interaction of simple organic compounds with a model mineral on the molecular level in an aquatic environment. The study focussed on the Sapphire 001 surface cut while the preliminary results from the 110 cut (section 3.2.5) were used to support some interpretations. Most interestingly, the differences observed in the SFG spectra of the two cuts could be explained by the different OH densities on 110 and 001 surfaces, respectively. Therefore, proposed future work is to study the adsorption mechanism of the used organic compounds on the sapphire 110 surface and possibly other cuts with differing OH density or surface structure systematically. Longer chains and complex compounds with different cuts will be another step. Some other minerals (e.g. silica and titanium oxide) are of same interest as sapphire as model systems for natural minerals. In addition, the comparison of the adsorption mechanisms of the same contact medium from its gas phase and liquid phase, respectively, will provide more information to understand the interaction on the molecular level.

As mentioned in section (3.2.1.2), the surface quality is a crucial parameter among the adsorption process. The effect of samples annealing and polishing can be studied in detail, in particular with respect to the influence of defects introduced by the process of polishing. Also, the dependence of surface quality on the annealing parameters can be studied. Finally, since the sapphire surface is a strongly hydrophilic surface, the desorption mechanism of water molecules from the surface can be analyzed with the same technique during sample heating. The surface coverage and molecular orientation can be investigated as a function of surface temperature and ambient humidity.

4.2 New techniques

Two novel techniques were developed in the time course of this study. The future applications of these two techniques are wide and promising. Preliminary results will be presented here. These techniques were planed to serve in studying the adsorption of the Self Assembled Monolayers (SAMs) on metal surfaces and their potential application to chemically modified micro-fluidic channels [80].

4.2.1 SHG- Ellipsometry

The adsorption of SAMs using SHG and Ellipsometry was extensively investigated in the last few decades. SHG is used to provide information about the surface coverage while Ellipsometry is used to specify the thickness of the SAM layer. In the case of coating micro-fluidic channels with SAMs, the channels are often only accessible with SHG. Therefore a correlation between the surface coverage and the layer thickness was needed. The target was to understand the interactions between homogeneous and heterogeneous fluids and chemically modified micro-fluidic channels. The functionalization of the metal surfaces with alkanethiols was the system of interest.

For this purpose the setup shown in Figure 4-1 was constructed. Linear and nonlinear techniques (Ellipsometry and SHG, respectively) were combined to yield direct simultaneous information about the surface coverage and layer thickness in real time [81]. The performance of the setup was verified using some previously studied adsorption systems. Figure 4-2 shows a sample result of the adsorption of octadecanethiol on gold surface. This result provides two kinds of information; 1) the adsorption rate and 2) the coverage-thickness correlation. An example of the obtained correlation curves is shown in Figure 4-3. Figure 4-3a shows a comparison of the coverage-thickness dependence at different concentrations (0.2, 0.5 and 1.0 μM) of a single chain length (octadecanethiol (C18)) adsorbed from ethanol bulk solution onto gold surface. Figure 4-3b shows a comparison of different chain lengths (C4, C12 and C18) at the same concentration.

The proposed future work on such a system is to construct calibration curves for different molecules on different surfaces under different adsorption conditions. These calibration curves can be used to determine the SAM thickness inside the micro-fluidic channels (MF), in set Figure 4-1, by measuring the SHG remotely.

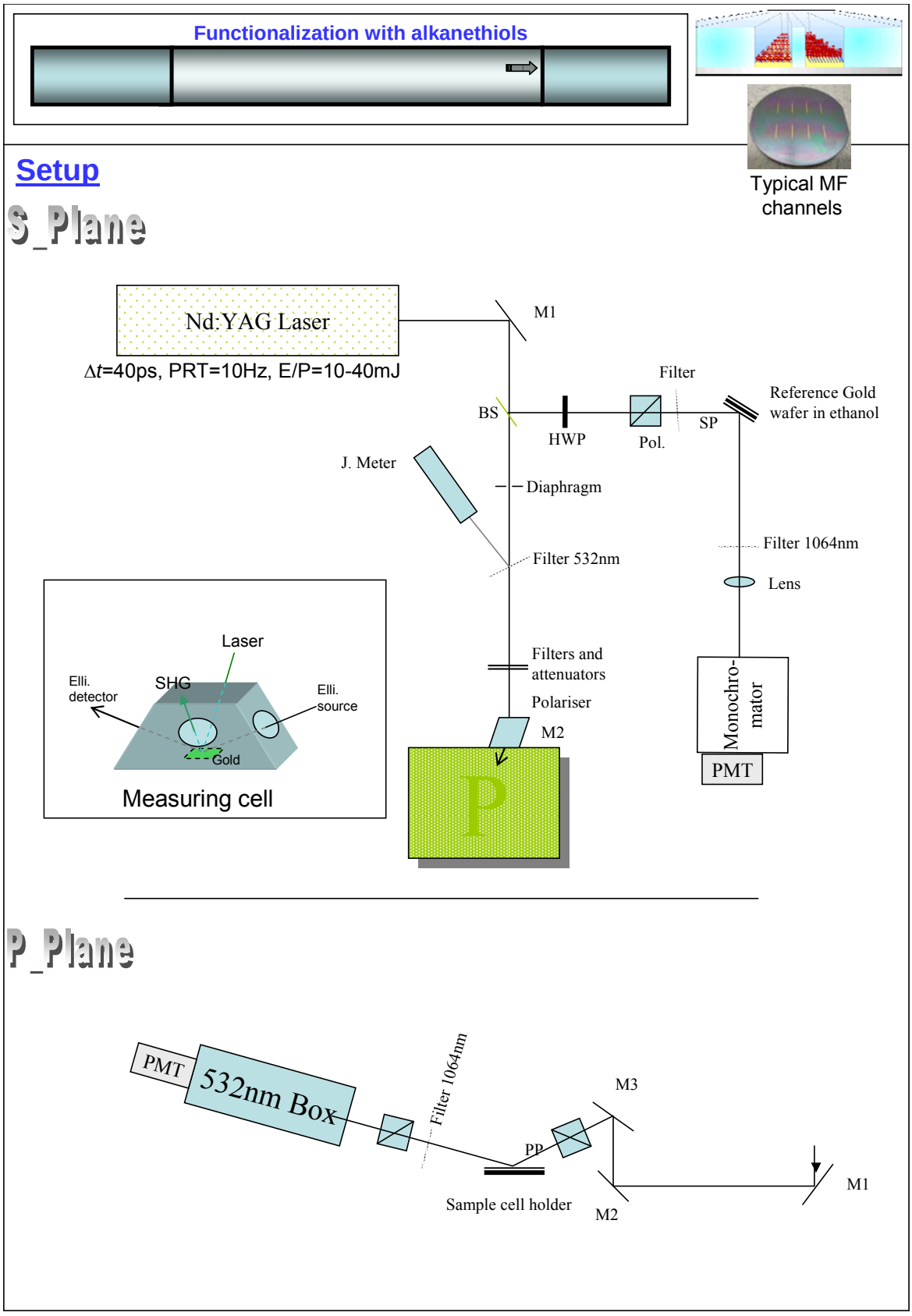

Figure 4-1 SHG-Ellipsometry setup

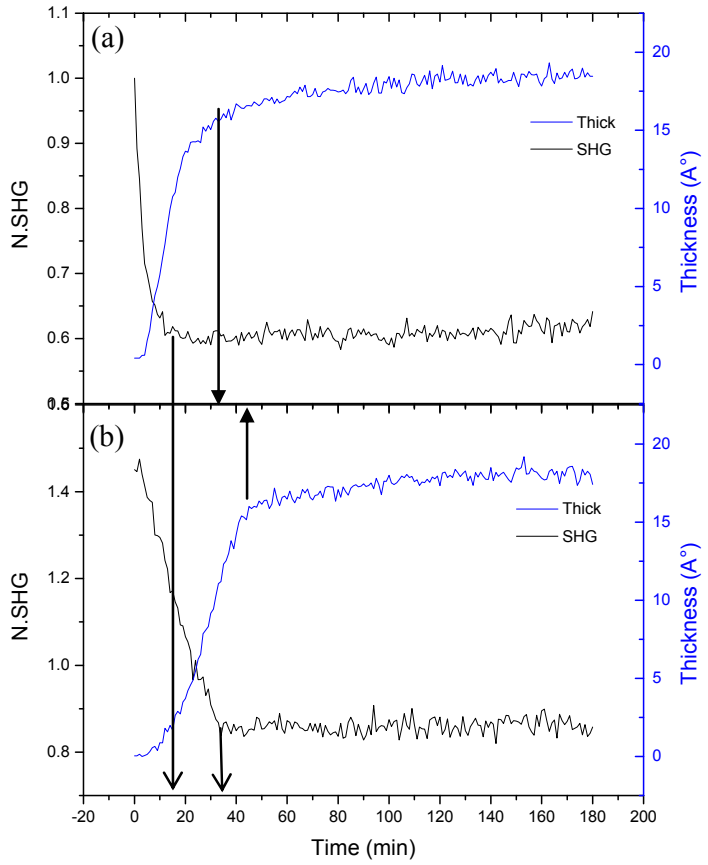

Figure 4-2 A sample result of the adsorption of octadecanethiol on gold surface for two different concentrations (a) c=5µM, (b) c=2µM

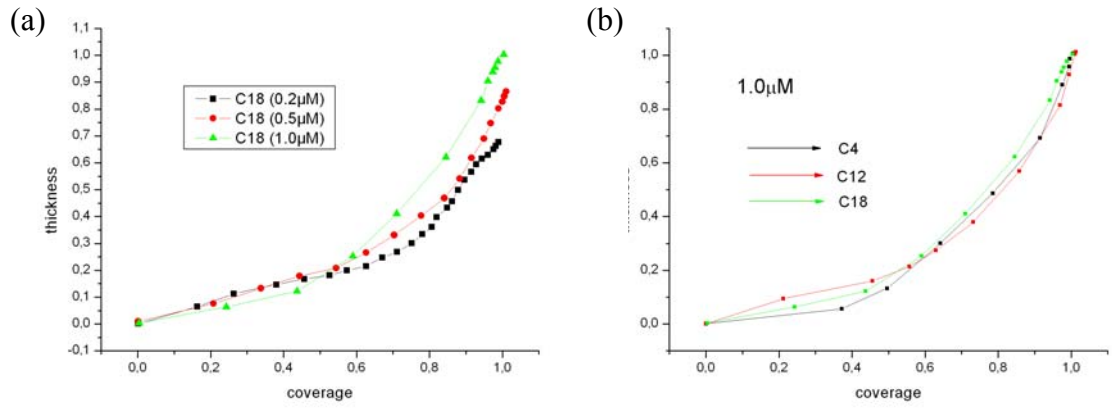

Figure 4-3 A sample of the obtained correlation curves, (a) shows a comparison of coverage-thickness dependence at different concentrations (0.2, 0.5 and 1.0 µM) of single chain length (octadecanthiol (C18)) adsorbed from ethanol bulk solution on gold surface, (b) shows a comparison of different chain lengths (C4, C12 and C18) at the same concentration (1µM).

4.2.2 Real time special and temporally resolved SFG [82]

There are two commonly known principles in SFG measurements; 1) Scan SFG (SSFG) which was used so far in the present work. In SSFG the spectral range is scanned with given steps and the SFG signal is measured at each step, as discussed in the experimental section. 2) Broad-Band SFG (BBSFG) where a snapshot of certain spectral range is taken at once using an incident broad-band IR beam and the SFG signal is measured using a CCD camera which is calibrated to the selected scan range. Typically, there are some differences observable between the results of these two approaches. Obviously, the reason is that the molecular perturbation is different in SSFG from that induced by BBSFG. In SSFG, the resonances are excited one after the other, while in BBSFG all resonances that are located in the selected spectral range are excited altogether. This was the access key to the idea presented in the following, however, understanding the differences in the obtained spectra is not the only advantage of the developed technique. More interesting applications can be achieved using this technique as will be mentioned in the end of this section. The target was to resolve the broadband beam spatially into a number of channels travelling in space with resolved time differences. If the special and temporal dispersion could be separated, then the time delay can be an independent parameter.

The principle of the system is illustrated in Figure 4-4. The spatial dispersion was achieved using the two gratings (G1 and G2). Due to the geometry, a small temporal dispersion accompanied the spatial dispersion. Larger time dispersion could be obtained by introducing a highly dispersive glass into the path of the broadband beam. Figure 4-5 shows the configuration of the beam-overlap in the SFG experiment. The broadband IR was focussed onto the surface using a suitable cylindrical lens and the defocused beam was collimated beyond the sample using another cylindrical lens. The collimated SFG was reflected to the CCD camera and detected as 2D image, which could be analyzed later into 3D information (wavelength, time delay, and intensity). A sample time-resolved-spatial-resolved SFG result is shown in Figure 4-6.

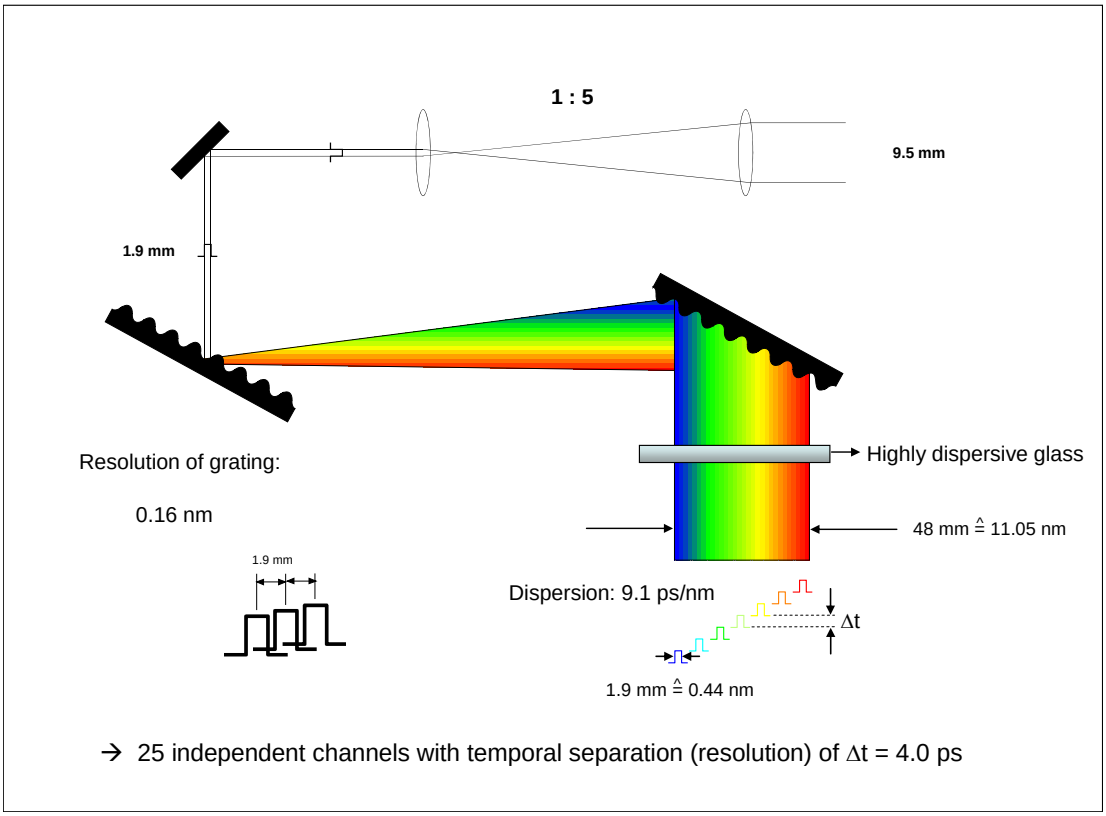

Figure 4-4 Pulse disperser

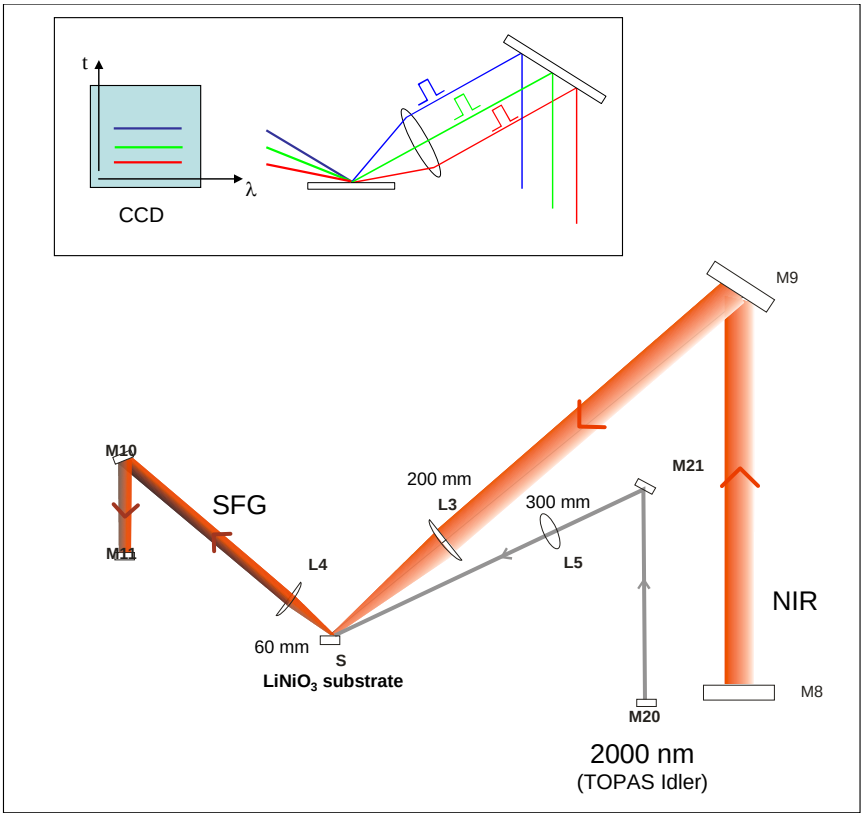

Figure 4-5 The configuration of the beam-overlap in the SFG experiment

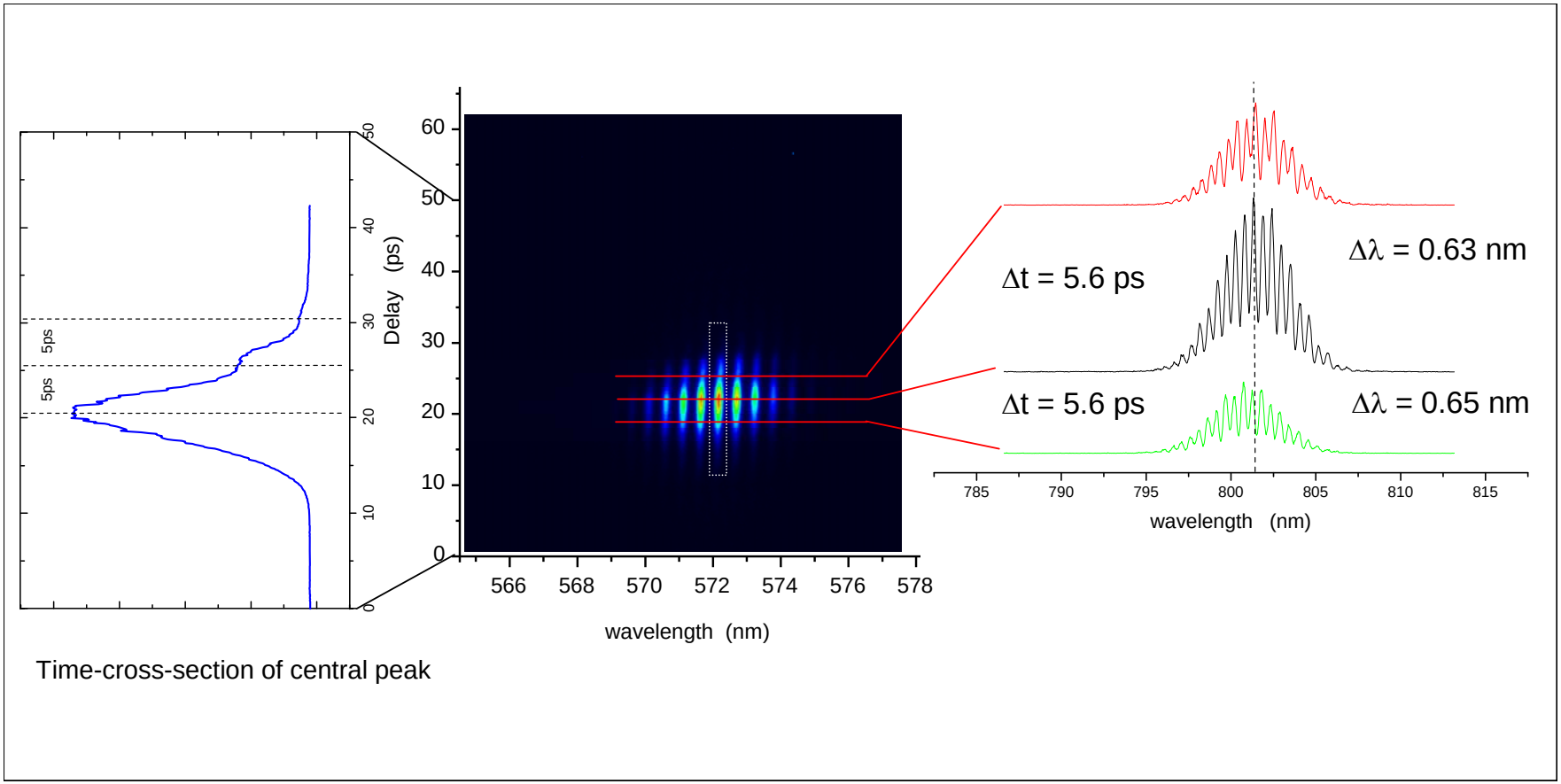

Figure 4-6 A sample of the obtained time- – and spatially-resolved SFG spectra

The features achieved in the preliminary tests can be summarized as follows:

1. Up to 25 temporally independent channels were obtained
2. The obtained spectral width/Pulse duration was ~15 cm^{-1}/ps
3. The obtained temporal dispersion was ~ 9.1 ps/nm
4. The time resolution (i.e. minimum separation between subsequent pulses) was 4ps
5. The spatial and temporal delays were separated processes and therefore changes in the time delay can be easily achieved.

The proposed technical future work on improving this novel detection technique is to optimize the dispersion parameters (grating resolutions, sizes and distances) to increase the number of channels and to further reduce the minimum delay time. On the other hand, the proposed applications utilizing the advantages of this system are the study of the dynamics of surface vibrations, fluids, and surface plasmons. Vibrational energy transfer in SAM systems can be also studied.

REFERENCES

1 *M. Buck and M. Himmelhaus, "Vibrational spectroscopy of interfaces by infrared–visible sum frequency generation", J Vac Sci Technol A 19, pp. 2717–2736 (2001)*

2 *P. A. Franken, A. E. Hill, C. W. Peters, and G. Weinreich, " Generation of Optical Harmonics" Phys. Rev Lett., vol. 7, p. 118, (1961)*

3 *G.T. Boyd, Y.R. Shen and T.W. Hansch, "Continuous-wave second-harmonic generation as a surface microprobe", Opt. Lett. 11 97 (1986)*

4 *Andrew J. Moad and Garth J. Simpson, "A Unified Treatment of Selection Rules and Symmetry Relations for Sum-Frequency and Second Harmonic Spectroscopies", J. Phys. Chem. B , 108, 3548-3562 (2004)*

5 *Y.R. Shen, "Optical Second Harmonic Generation at Interfaces", Annu. ReV. Phys. Chem. 40, 327. (1989)*

6 *K.B. Eisenthal, "Liquid Interfaces Probed by Second-Harmonic and Sum-Frequency Spectroscopy", Chem. ReV. 96, 1343.(1996)*

7 *M. Mucha, T. Frigato, L.M. Levering, H.C. Allen, D.J. Tobias, L.X. Dang and P.J. Jungwirth, "Unified Molecular Picture of the Surfaces of Aqueous Acid, Base, and Salt Solutions", Phys Chem. 109, 7617. (2005)*

8 *C.D. Cappa, J.D. Smith, K.R. Wilson, B.M. Messer, M.K. Gilles, R.C. Cohen and R.J. Saykally, "Effects of Alkali Metal Halide Salts on the Hydrogen Bond Network of Liquid Water", J. Phys. Chem. B , 109, 7046. (2005)*

9 *T.F. Heinz, H.W.K. Tom and Y.R. Shen," Determination of molecular orientation of monolayer adsorbates by optical second-harmonic generation", Phys. ReV. A , 28,1883 (1983)*

10 *M.J. Shultz, C. Schnitzer, D. Simonelli and S. Baldelli," Sum frequency generation spectroscopy of the aqueous interface: ionic and soluble molecular solutions", Int. ReV. Phys. Chem. 19, 123 (2000)*

11 *D.E. Gragson and G.L. Richmond, "Investigations of the structure and intermolecular hydrogen bonding of interfacial water molecules as probed by vibrational sum frequency spectroscopy", J. Phys. Chem. B, 102, 3847 (1998).*

12 *P.B. Miranda and Y.R. Shen, "Liquid Interfaces A Study by Sum-Frequency Vibrational Spectroscopy" J. Phys. Chem. B, 103, 3292. (1999)*

13 *P.B. Petersen and R.J. Saykally, "Evidence for an Enhanced Hydronium Concentration at the Liquid Water Surface" J. Phys. Chem. B , 109, 7976 (2005)*

14 *J.H. Hunt, P. Guyot-Sionnest and Y.R. Shen," Observation of C-H stretch vibrations of monolayers of molecules optical sum-frequency generation", Chem. Phys. Lett. 133, 189 (1987)*

15 *P. Guyot-Sionnest, R. Superfine, J.H Hunt, and Y.R. Shen, "Vibrational spectroscopy of a silane monolayer at air/solid and liquid/solid interfaces using sum-frequency generation", Chem. Phys. Lett. 144, 1 (1988)*

16 *A.L. Harris, C.E.D. Chidsey, N.J. Levinos and D.N. Loiacono, "Monolayer vibrational spectroscopy by infrared-visible sum generation at metal and semiconductor surfaces", Chem. Phys. Lett. 141, 350 (1987)*

17 *R. Superfine, J.Y. Huang and Y.R. Shen," Nonlinear optical studies of the pure liquid/vapor interface: Vibrational spectra and polar ordering", Phys. ReV. Lett. 66, 1066.(1991)*

18 *Q. Du, R. Superfine, E. Freysz and Y.R. Shen, "Vibrational spectroscopy of water at the vapor/water interface", Phys. ReV. Lett. 1993, 70, 2313.*

19 *N. Bloembergen and P.S. Pershan, "Light Waves at the Boundary of Nonlinear Media", Phys. ReV. 128, 606 (1962)*

20 *Sandhya Gopalakrishnan, Dingfang Liu and H.C. Allen, " Vibrational Spectroscopic Studies of Aqueous Interfaces Salts, Acids, Bases, and Nanodrops", Chem. Rev. 2006, 106, 1155̃1175 ()*

21 *B. Dick, A. Gierulski, G. Marowsky, G.A. Reider, "Determination of the nonlinear optical susceptibility $\chi(2)$ of surface layers by sum and difference frequency generation in reflection and transmission", Appl. Phys. B. 1985, 38, 107 (1985)*

22 *G. Wagniere," Theoretical investigation of Kleinman symmetry in molecules" Appl. Phys. B 41,169-172 (1986)*

23 *V. Mizrah and, J.E Sipe, "Phenomenological treatment of surface second-harmonic generation" J. Opt. Soc. Am. B, 5 , 660 (1988)*

24 *J.E. Sipe, "New Green-function formalism for surface optics" J. Opt. Soc. Am. B, 4, 481 (1987)*

25 *Michael Ware, "Physics of Light and Optics", Brigham Young University, August 1,(2006)*

26 *K. Kruse, Diploma work im Fachbereich Physik der Mathematisch-Naturwissenschaftlichen Fakult¨at Der Westf¨alischen Wilhelms-Universität Munster Nov. (2003)*

27 *Marvin R. Querry, Ph.D. "Optical constants", University of Missouri Kansas City, Missouri 64110 , June (1985)*

References

28 *J. Bertie, L.Z. Shuliang, H.E. Eysel, S. Baluja, and M.K Ahmed, "Infrared Intensities of Liquids XI: Infrared Refractive Indices from 8000 to 2 cm^{-1}, Absolute Integrated Intensities, and Dipole Moment Derivatives of Methanol at 25°C" Soc. For App. Spec. 1993, 47 8.*

29 *John E. Bertie, C. Dale Keefe et R. Norman Jones. Can. "Infrared Intensities of liquids VIII", J. Chem. 69, 1609 (1991)*

30 *John E. Bertie and Shuliang L. Zhang, "Infrared Intensities of liquids XXI" J. of Molecular Structure 413-414, 333-363 (1997)*

31 *T.S. Robinsin, "Optical Constants by Reflection", Proc. Phys. Soc. B, 1952, 65, 910 (.)*

32 *T.S. Robinsin, and W.C. Price, "The Determination of Infra-Red Absorption Spectra from Reflection Measurements" Proc. Phys. Soc. B, 1953, 66, 969 (1953)*

33 *Fahrenfort, "Attenuated total refIection" J. Spectrochimica Acta, 17, 698 (1961)*

34 *36 S. Ikawa, T. Ohba, S. Tanaka, Y. Morimoto, K. Fukushi and M. Kimura, "Measurement Of Far-Infrared Optical Constants By Atr", Int. J. Inf. Mil. Wav. 6, 287(1985)*

35 *X. Zhuang , P. B. Miranda, D. Kim , and Y. R. Shen, "Mapping molecular orientation and conformation at interfaces by surface nonlinear optics", Phys. Rev. B 59, 12632 (1999)*

36 *Chiaki Hirose, Naotoshi Akamatsu, and Kazunari Domen. "Formulas for the analysis of surface sum-frequency generation spectrum", J. Chem. Phys. 96, Issue 2, pp. 997 (1992)*

37 *Chiaki Hirose, Hiroyoshi Yamamoto, Naotoshi Akamatsu and Kazunari Domen, "Orientation analysis by simulation of vibrational sum frequency generation spectrum: CH stretching bands of the methyl group" J. Phys. Chem. 97, 10064 (1993)*

38 *J.A. Giordmaine, "Nonlinear Optical Properties of Liquids", Phys. Rev. 138, A1599 (1965)*

39 *Xing Wei, Seok-Cheol Hong, Xiaowei Zhuang, Tomohisa Goto , and Y. R. Shen, "Nonlinear optical studies of liquid crystal alignment on a rubbed polyvinyl alcohol surface", Phys. Rev. E 62, 5160 - 5172 (2000)*

40 *P. Fischer and A.D. Buckingham, "Surface second-order nonlinear optical activity" J. Opt. Soc. of America B, V15, Issue 12, pp. 2951-2957 (1998)*

41 *Colin D. Bain, Paul B. Davies, T. Hui Ong, Robert N. Ward and Murray A. Brown, "Quantitative analysis of monolayer composition by sum-frequency vibrational spectroscopy", Langmuir, 7(8), 1563 (1991)*

42 *Pascal Reiller1, Val´erie Moulin, Florence Casanova and Christian Dautel, " On the study of Th(IV)-humic acid interactions by competition sorption studies with silica and determination of global interaction constants", Radiochim. Acta 91, 513–524 (2003)*

43 *Gang Ma, Dingfang Liu, and Heather C. Allen, "Piperidine adsorption on hydrated α-alumina (0001) surface studied by vibrational sum frequency generation spectroscopy ", Langmuir, 20 (26), 11620 -11629, (2004)*

44 *X.D Zhu, H. Suhr and Y.R. Shen," Surface vibrational spectroscopy by infrared-visible sum frequency generation", Phys. ReV. B 35, 3047(1987)*

45 *Weitao Liu, Luning Zhang and Y.R. Shen "Interfacial layer structure at alcohol/silica interfaces probed by sum-frequency vibrational spectroscopy", Chemical Physics Letters 412, 206–209 (2005)*

46 *Andrea B. Voges, Hind A. Al-Abadleh, Michael J. Musorrafiti, Paul A. Bertin,SonBinh T. Nguyen, and Franz M. Geiger, "Carboxylic Acid- and Ester-Functionalized Siloxane Scaffolds on Glass Studied by Broadband Sum Frequency Generation" J. Phys. Chem. B, 108 (48), 18675 -18682 (2004)*

47 *K. Wolfrum, J. Löbau and A, Laubereau, "Sum-frequency spectroscopy of physisorbed and chemisorbed molecules at liquid and solid surfaces using band-width-limited picosecond pulses", App. Phys. A, Applied Physics A: Materials Science & Processing, Volume 59, Number 6 / December, (1994)*

48 *Man Xu, Dingfang Liu and Heather C. Allen, "Ethylenediamine at Air/Liquid and Air/Silica Interfaces" Environ. Sci. Technol., 40 (5), 1566 -1572, (2006)*

49 *Ye Shen , Satoshi Nihonyanagi and Kohei Uosaki,"Sum frequency generation (SFG) study of the pH-dependent water structure on a fused quartz surface modiÐed by an octadecyltrichlorosilane (OTS) monolayer", Phys. Chem. Chem. Phys. 3, 3463-3469 (2001)*

50 *S. Carlos-Cuellar, P. Li, A. P. Christensen, B. J. Krueger, C. Burrichter, and V. H. Grassian , "Heterogeneous Uptake Kinetics of Volatile Organic Compounds on Oxide Surfaces Using a Knudsen Cell Reactor: Adsorption of Acetic Acid, Formaldehyde, and Methanol on r-Fe2O3, r-Al2O3, and SiO2" J. Phys. Chem. A 2003, 107, 4250-4261 (2003)*

51 *Jörgen Rosenqvist, Kristina Axe, Staffan Sjöberg and Per Persson, "Adsorption of dicarboxylates on nano-sized gibbsite particles: effects of ligand structure on bonding mechanisms", Colloids and Surfaces A: Physicochem. Eng. Aspects 220 , 91_/104 (2003)*

52 *Cyrille Alliot, Lionel Bion, Florence Mercier and Pierre Toulhoat, "Sorption of aqueous carbonic, acetic, and oxalic acids onto α-alumina", Journal of Colloid and Interface Science 287, 444–451 ,(2005)*

53 *Dingfang Liu, Gang Ma, Man Xu, and Heather C. Allen, "Adsorption of Ethylene Glycol Vapor on α-Al2O3 (0001) and Amorphous SiO2", Environ. Sci. Technol., 39 (1), 206 -212, (2005)*

54 *Luning Zhang, Weitao Liu, and Y. Ron Shen, "Competitive Molecular Adsorption at Liquid/Solid Interfaces: A Study by Sum-Frequency Vibrational Spectroscopy", J. Phys. Chem. C , 111, 2069-2076 , (2007)*

55 *D.L. Sparks, "Environmental Soil Chemistry", 2nd ed.; Academic Press: San Diego,(2003).*

56 *P.H. Hsu, "Aluminium hydroxides and oxyhydroxides. In Minerals in Soil Environments; 2nd ed.; Dixon, J. B., Weed, S. B., Eds.; The Soil Science Society of America, Inc.: Madison, Wisconsin, p 1244 (1989)*

57 *[A. A. Mani, L. Dreesen, Ph. Hollander, C. Humbert, Y. Caudano, P. A. Thiry and A. Peremans, "Pumping picosecond optical parametric oscillators by a pulsed Nd : YAG laser mode locked using a nonlinear mirror" Applied Physics Letters Volume: 79 Issue: 13 Pages: 1945-1947 (2001)] and [A. A. Mani, Ph. Hollander, P. A. Thiry and A. Peremans , "All-solid-state 12 ps actively passively mode-locked pulsed Nd:YAG laser using a nonlinear mirror", App. Phys. Lett., 75, 20 (1999)]*

58 *Dr. D. Sheild (Institute of Nuclear Waste Disposal, Forschungszentrum Karlsruhe - Deutschland (FZK)), personal contact.*

59 *Dr. J. Luetzenkircher (Institute of Nuclear Waste Disposal, Forschungszentrum Karlsruhe - Deutschland (FZK)), personal contact.*

60 *P. K. Srivastava, D. K. Rai and S. B. Rai, "Frequency of OH in solutions of n-butanol in carbon tetrachloride: effect of dilution", Spectrochimica Acta Part A: Molecular and Biomolecular Spectroscopy Volume 56, Issue 7, Pages 1283-1289 (2000)*

61 *Tetsuo Yuzawa, Jun Kubota, Ken Onda, Akihide Wada, Kazunari Domen and Chiaki Hirose, "A TPD and SFG study of propionic acid adsorbed on Ni(110) surface", Journal of Molecular Structure, Vol 413-414, Pages 307-312 (1997)*

62 *Rong Lu, Wei Can, Bao-hua Wiv Zhen Zhang, Yuan Guo, and Hong-fei Wang, "C—H Stretching Vibrations of Methyl, Methylene and Methine Groups at the Vapor/ Alcohol (n = 1—8) Interfaces", J. Phys. Chem. B, 109, 14118-14129 (2005)*

63 *Lisa L. Van Loon, Rena N. Minor and Heather C. Allen , "Structure of Butanol and Hexanol at Aqueous, Ammonium Bisulfate, and Sulfuric Acid Solution Surfaces Investigated by Vibrational Sum Frequency Generation Spectroscopy", J. Phys. Chem. A , 111, 7338-7346 (2007)*

64 *M. S. Yeganeh, S. M. Dougal, and H. S. Pink, "Vibrational Spectroscopy of Water at Liquid_Solid Interfaces: Crossing the Isoelectric Point of a Solid Surface", Physical Review Letters, Volume 83, Number 6, (1999)*

65 *Quan Du, Eric Freysz, and Y. Ron Shen, "Vibrational spectra of water molecules at quartz/water interfaces", Phys. Rev. Lett. 72, 238 (1994)*

66 *Björn Braunschweig, Stephan Eissner, and Winfried Daum, "Molecular Structure of a Mineral-Water Interface- Effects of Surface NanoRoughness of a-Al2O3", J. Phys. Chem. C, Vol. 112, No. 6, (2008)*

67 *Dr. Robert Polly (Institute of Nuclear Waste Disposal, Forschungszentrum Karlsruhe - Deutschland (FZK)), personal contact*

68 *Jiri Janecek, and Roland R. Netz, "Interfacial Water at Hydrophobic and Hydrophilic Surfaces: Depletion versus Adsorption", Langmuir, 23, 8417-8429 (2007)*

69 *Sandhya Gopalakrishnan, Pavel Jungwirth, Douglas J. Tobias, and Heather C. Allen, "Air-Liquid Interfaces of Aqueous Solutions Containing Ammonium and Sulfate: Spectroscopic and Molecular Dynamics Studies", J. Phys. Chem. B, 109, 8861-8872, (2005)*

70 *Franck Vidal and Abderrahmane Tadjeddine, "Sum-frequency generation spectroscopy of interfaces", Rep. Prog. Phys. 68, 1095–1127 (2005)*

71 *Yuen Ron Shen and Victor Ostroverkhov, "Sum-Frequency Vibrational Spectroscopy on Water Interfaces: Polar Orientation of Water Molecules at Interfaces", Chem. Rev. 106, 1140-1154, (2006)*

72 *M. Yoshimoto, T. Maeda, T. Ohnishi, H. Koinuma, O. Ishiyama, M. Shinohara, M. Kubo, R. Miura and A. Miyamoto, "Atomic-scale formation of ultrasmooth surfaces on sapphire substrates for high-quality thin-film fabrication", Appl. Phys. Lett. 67, p. 2615.,(1995)*

73 *Primoz̆ Rebernik Ribic̆, Gvido Bratina, "Fabrication of rubrene nanowires on vicinal (0001) sapphire surfaces", Surface Science 601, L25–L28, (2007)*

74 *Primoz̆ Rebernik Ribic̆, Gvido Bratina, "Behavior of the (0001) surface of sapphire uponhigh-temperature annealing", Surface Science 601, 44–49, (2007)*

75 *Elizabeth A. Raymond and Geraldine L. Richmond, "Probing the Molecular Structure and Bonding of the Surface of Aqueous Salt Solutions", J. Phys. Chem. B , 108, 5051-5059 ,(2004)*

76 *Douglas C. Daniel and Jeanne L. McHale, "Hydrogen Bonding in CHCl3/DMSO-d6 and CDCl3/DMSO-h6 Mixtures", J. Phys. Chem. A , 101, 3070-3077, (1997)*

77 *K. C. Hass and W. F. Schneider, "First-Principles Molecular Dynamics Simulations of H2O on r-Al2O3 (0001)", J. Phys. Chem. B, 104, 5527-5540 (2000)*

78 *Elizabeth A. Raymond, Teresa L. Tarbuck, Mac G. Brown,§ and Geraldine L. Richmond, "Hydrogen-Bonding Interactions at the Vapor/Water Interface Investigated by Vibrational Sum-Frequency*

Spectroscopy of HOD/H2O/D2O Mixtures and Molecular Dynamics Simulations", J. Phys. Chem. B, 107, 546-556, (2003)

79 *Vidal Barrón and José Torrent "Surface Hydroxyl Configuration of Various Crystal Faces of Hematite and Goethite", Journal Of Colloid And Interface Science 177, 407–410 (1996)*

80 *Tilmann Rogge, Kristin Mandisloh, Timo Mappes, Martina Sch¨urmann, Axel Rosenhahn2, Ahmed Abdelmonem, and Michael Himmelhaus, DPG Spring Meeting of the Divison Condensed Matter, 21st General Conf.of the Condensed Matter Division of the European Physical Society, Dresden, March 26-31, 2006 Verhandlungen der Deutschen Physikalischen Gesellschaft, R.6, B.41(2006) CPP 24.12., Nanoscale Flow-Cells and their Application*

81 *Ahmed Abd el Monem, Jana Wehrmeister, Mark Helm, and Michael Himmelhaus, DPG Spring Meeting of the Divison Condensed Matter, 21st General Conf.of the Condensed Matter Division of the European Physical Society, Dresden, March 26-31, 2006 Verhandlungen der Deutschen Physikalischen Gesellschaft, R.6, B.41(2006) CPP 17.6., Experimental determination of the coverage-height dependence of self-assembled monolayers during film formation*

82 *Ahmed Abd el Monem, Michael Himmelhaus, IMS symposium "Frontier of Molecular Science Explored by Sum-Frequency Spectroscopy", Okazaki Conference Center, Japan, Dec. 5-6th 2006, An Approach to Real-Time Time-Resolved Sum Frequency Generation Using A Broadband Femtosecond Laser Source*

LIST OF FIGURES

LIST OF TABLES

APPENDIX

Appendix 1

A conversion table for some important formulas between the cgs- and SI-unit systems.

Quantity	*The relation*
Speed of light in vacuum	$c_{cgs} = \sqrt{\mu_o \varepsilon_o}_{SI}$
Electric Field, potential and Voltage	$\{E, \Phi, V\}_{cgs} = \sqrt{4\pi\varepsilon_o}.\{E, \Phi, V\}_{SI}$
Electric Susceptibility	$\chi_{cgs} = \frac{1}{4\pi}\chi_{SI}$
Electric second order nonlinear Susceptibility	$\chi_{cgs} = \frac{1}{4\pi\sqrt{4\pi\varepsilon_o}}\chi_{SI}$
Polarization, charge, current and current density	$\{P, q, I, j\}_{cgs} = \frac{1}{\sqrt{4\pi\varepsilon_o}}.\{P, q, I, j\}_{SI}$
Electric Flux density	$D_{cgs} = \sqrt{\frac{4\pi}{\varepsilon_o}}D_{SI}$
Dielectric constant	$\varepsilon_{cgs} = \frac{\varepsilon_{SI}}{\varepsilon_o}$
Magnetic Permeability	$\varepsilon_{cgs} = \frac{\mu_{SI}}{\mu_o}$
Magnetic induction (Flux Density)	$B_{cgs} = \sqrt{\frac{4\pi}{\mu_o}}B_{SI}$
Magnetic Field	$H_{cgs} = \sqrt{4\pi\mu_o}.H_{SI}$
Magnetization	$M_{cgs} = \sqrt{\frac{\mu_o}{4\pi}}M_{SI}$
Resistance, Impendence and inductivity	$\{R, Z, L\}_{cgs} = 4\pi\varepsilon_o.\{R, Z, L\}_{SI}$
Conductivity and Capacity	$\{\sigma, C\}_{cgs} = \frac{1}{4\pi\varepsilon_o}\{\sigma, C\}_{SI}$

Appendix 2

The Fresnel Coefficients [28]

Augustin Fresnel (1788-1829) thought of light as transverse mechanical waves propagating within materials. Instead of relating the parallel components of the electric and magnetic fields across the boundary between the materials, Fresnel used the principle that, as a transverse mechanical wave propagates from one material to the other, the two materials should not slip past each other at the interface. This "gluing" of the materials at the interface also forbids the possibility of the materials detaching from one another (creating gaps) or passing through one another as they experience the wave vibration. This mechanical approach to light worked splendidly and explained polarization effects along with the variations in reflectance and transmission as a function of the incident angle of the light. Fresnel wrote the relationships between the various plane waves in terms of coefficients that compare the reflected and transmitted field amplitudes to those of the incident field. This is done separately for each polarization.

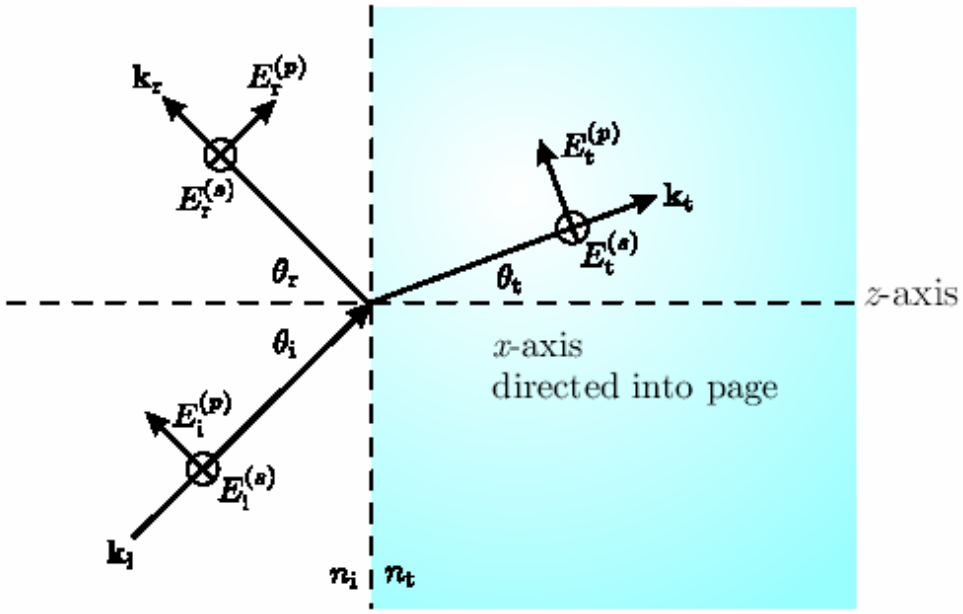

The ratio of the reflected and transmitted field components to the incident field components are specified by the following coefficients (called Fresnel coefficients):

$$r_s \equiv \frac{E_{\mathrm{r}}^{(s)}}{E_{\mathrm{i}}^{(s)}} = \frac{\sin\theta_{\mathrm{t}}\cos\theta_{\mathrm{i}} - \sin\theta_{\mathrm{i}}\cos\theta_{\mathrm{t}}}{\sin\theta_{\mathrm{t}}\cos\theta_{\mathrm{i}} + \sin\theta_{\mathrm{i}}\cos\theta_{\mathrm{t}}} = -\frac{\sin(\theta_{\mathrm{i}} - \theta_{\mathrm{t}})}{\sin(\theta_{\mathrm{i}} + \theta_{\mathrm{t}})} = \frac{n_{\mathrm{i}}\cos\theta_{\mathrm{i}} - n_{\mathrm{t}}\cos\theta_{\mathrm{t}}}{n_{\mathrm{i}}\cos\theta_{\mathrm{i}} + n_{\mathrm{t}}\cos\theta_{\mathrm{t}}}$$

$$t_s \equiv \frac{E_{\mathrm{t}}^{(s)}}{E_{\mathrm{i}}^{(s)}} = \frac{2\sin\theta_{\mathrm{t}}\cos\theta_{\mathrm{i}}}{\sin\theta_{\mathrm{t}}\cos\theta_{\mathrm{i}} + \sin\theta_{\mathrm{i}}\cos\theta_{\mathrm{t}}} = \frac{2\sin\theta_{\mathrm{t}}\cos\theta_{\mathrm{i}}}{\sin(\theta_{\mathrm{i}} + \theta_{\mathrm{t}})} = \frac{2n_{\mathrm{i}}\cos\theta_{\mathrm{i}}}{n_{\mathrm{i}}\cos\theta_{\mathrm{i}} + n_{\mathrm{t}}\cos\theta_{\mathrm{t}}}$$

$$r_p \equiv \frac{E_{\mathrm{r}}^{(p)}}{E_{\mathrm{i}}^{(p)}} = \frac{\cos\theta_{\mathrm{t}}\sin\theta_{\mathrm{t}} - \cos\theta_{\mathrm{i}}\sin\theta_{\mathrm{i}}}{\cos\theta_{\mathrm{t}}\sin\theta_{\mathrm{t}} + \cos\theta_{\mathrm{i}}\sin\theta_{\mathrm{i}}} = -\frac{\tan(\theta_{\mathrm{i}} - \theta_{\mathrm{t}})}{\tan(\theta_{\mathrm{i}} + \theta_{\mathrm{t}})} = \frac{n_{\mathrm{i}}\cos\theta_{\mathrm{t}} - n_{\mathrm{t}}\cos\theta_{\mathrm{i}}}{n_{\mathrm{i}}\cos\theta_{\mathrm{t}} + n_{\mathrm{t}}\cos\theta_{\mathrm{i}}}$$

$$t_p \equiv \frac{E_{\mathrm{t}}^{(p)}}{E_{\mathrm{i}}^{(p)}} = \frac{2\cos\theta_{\mathrm{i}}\sin\theta_{\mathrm{t}}}{\cos\theta_{\mathrm{t}}\sin\theta_{\mathrm{t}} + \cos\theta_{\mathrm{i}}\sin\theta_{\mathrm{i}}} = \frac{2\cos\theta_{\mathrm{i}}\sin\theta_{\mathrm{t}}}{\sin(\theta_{\mathrm{i}} + \theta_{\mathrm{t}})\cos(\theta_{\mathrm{i}} - \theta_{\mathrm{t}})} = \frac{2n_{\mathrm{i}}\cos\theta_{\mathrm{i}}}{n_{\mathrm{i}}\cos\theta_{\mathrm{t}} + n_{\mathrm{t}}\cos\theta_{\mathrm{i}}}$$

Appendix 3

Euler angles

The **Euler angles** were developed by ***Leonhard Euler*** to describe the orientation of a rigid body in 3-dimensional Euclidean space. In this work, the Euler angles will be defined as follows, starting with the x,y,z-frame;

1. Rotation with an angle α around the z-axis => The new unit vectors in the a and b directions can be expressed in terms of the old unit vectors in the x and y directions through the rotation angle α

$$\hat{a} = \cos\alpha\hat{x} + \sin\alpha\hat{y}$$
$$\hat{b} = -\sin\alpha\hat{x} + \cos\alpha\hat{y}$$

which can be presented in matrix notation as follow:

$$\begin{pmatrix} \cos\alpha & \sin\alpha & 0 \\ -\sin\alpha & \cos\alpha & 0 \\ 0 & 0 & 1 \end{pmatrix}$$

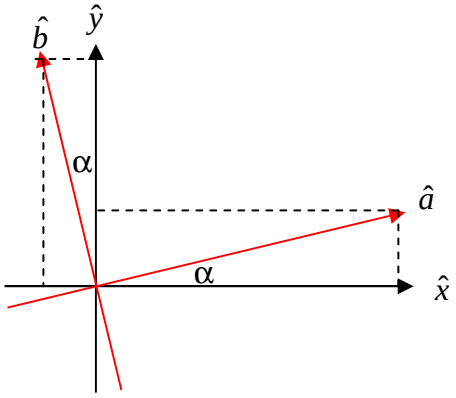

2. Rotation with an angle β around the new x-axis =>

$$\begin{pmatrix} 1 & 0 & 0 \\ 0 & \cos\beta & \sin\beta \\ 0 & -\sin\beta & \cos\beta \end{pmatrix}$$

3. Finally, Rotation with an angle γ around the new z-axis (c) =>

$$\begin{pmatrix} \cos\gamma & \sin\gamma & 0 \\ -\sin\gamma & \cos\gamma & 0 \\ 0 & 0 & 1 \end{pmatrix}$$

The over all effect can be represented as:

$$U = \begin{pmatrix} \cos\alpha & \sin\alpha & 0 \\ -\sin\alpha & \cos\alpha & 0 \\ 0 & 0 & 1 \end{pmatrix}\begin{pmatrix} 1 & 0 & 0 \\ 0 & \cos\beta & \sin\beta \\ 0 & -\sin\beta & \cos\beta \end{pmatrix}\begin{pmatrix} \cos\gamma & \sin\gamma & 0 \\ -\sin\gamma & \cos\gamma & 0 \\ 0 & 0 & 1 \end{pmatrix}$$

$$= \begin{pmatrix} \cos(\gamma)\cos(\alpha) - \sin(\gamma)\sin(\alpha)\cos(\beta) & -\cos(\gamma)\sin(\alpha)\cos(\beta) - \sin(\gamma)\cos(\alpha) & \sin(\gamma)\sin(\beta) \\ -\cos(\gamma)\sin(\alpha)\cos(\beta) - \sin(\gamma)\cos(\alpha) & \cos(\gamma)\cos(\alpha)\cos(\beta) - \sin(\gamma)\sin(\alpha) & \cos(\gamma)\sin(\beta) \\ \sin(\alpha)\sin(\beta) & -\cos(\alpha)\sin(q) & \cos(\beta) \end{pmatrix}$$

Appendix 4

The generating matrices of the 32 point groups (Crystal classes)[*]

$M_I = \begin{pmatrix} 1 & 0 & 0 \\ 0 & 1 & 0 \\ 0 & 0 & 1 \end{pmatrix}$ Identity	
$M_1 = \begin{pmatrix} -1 & 0 & 0 \\ 0 & -1 & 0 \\ 0 & 0 & 1 \end{pmatrix}$ Inversion	$M_2 = \begin{pmatrix} 1 & 0 & 0 \\ 0 & 1 & 0 \\ 0 & 0 & -1 \end{pmatrix}$ Two fold rotation about x_3 axis
$M_3 = \begin{pmatrix} 1 & 0 & 0 \\ 0 & 1 & 0 \\ 0 & 0 & -1 \end{pmatrix}$ Reflection in x_1 x_2 plane	$M_4 = \begin{pmatrix} 1 & 0 & 0 \\ 0 & -1 & 0 \\ 0 & 0 & -1 \end{pmatrix}$ Two fold rotation about x_1 axis
$M_5 = \begin{pmatrix} -1 & 0 & 0 \\ 0 & 1 & 0 \\ 0 & 0 & 1 \end{pmatrix}$ Reflection in x_2 x_3 plane	$M_6 = \begin{pmatrix} 1 & 0 & 0 \\ 0 & -1 & 0 \\ 0 & 0 & 1 \end{pmatrix}$ Reflection in x_1 x_3 plane
$M_7 = \begin{pmatrix} 0 & -1 & 0 \\ 1 & 0 & 0 \\ 0 & 0 & 1 \end{pmatrix}$ Four fold rotation about x_3 axis	$M_8 = \begin{pmatrix} 0 & -1 & 0 \\ 1 & 0 & 0 \\ 0 & 0 & -1 \end{pmatrix}$ Four fold inversion-rotation about x_3 axis
$M_9 = \begin{pmatrix} -1/2 & -\sqrt{3}/2 & 0 \\ \sqrt{3}/2 & -1/2 & 0 \\ 0 & 0 & 1 \end{pmatrix}$ Three fold rotation about x_3 axis	$M_{10} = \begin{pmatrix} -1/2 & -\sqrt{3}/2 & 0 \\ \sqrt{3}/2 & 1/2 & 0 \\ 0 & 0 & -1 \end{pmatrix}$ Three fold inversion-rotation about x_3 axis
$M_{11} = \begin{pmatrix} 1/2 & -\sqrt{3}/2 & 0 \\ \sqrt{3}/2 & 1/2 & 0 \\ 0 & 0 & 1 \end{pmatrix}$ six fold rotation about x_3 axis	$M_{12} = \begin{pmatrix} -1/2 & -\sqrt{3}/2 & 0 \\ \sqrt{3}/2 & -1/2 & 0 \\ 0 & 0 & -1 \end{pmatrix}$ Six fold inversion-rotation about x_3 axis
$M_{13} = \begin{pmatrix} 0 & 0 & 1 \\ 1 & 0 & 0 \\ 0 & 1 & 0 \end{pmatrix}$ Three fold rotation [111] direction	$M_{14} = \begin{pmatrix} 0 & -1 & 0 \\ 0 & 0 & -1 \\ -1 & 0 & 0 \end{pmatrix}$ Three fold inversion-rotation [111] direction

[*] *Ervin Hartmann, An Introduction to Crystal Physics, International Union of Crystallography by University College Cardiff Press Cardiff, Wales*

Appendix 5

Anharmonic Oscillator and resonance enhancement

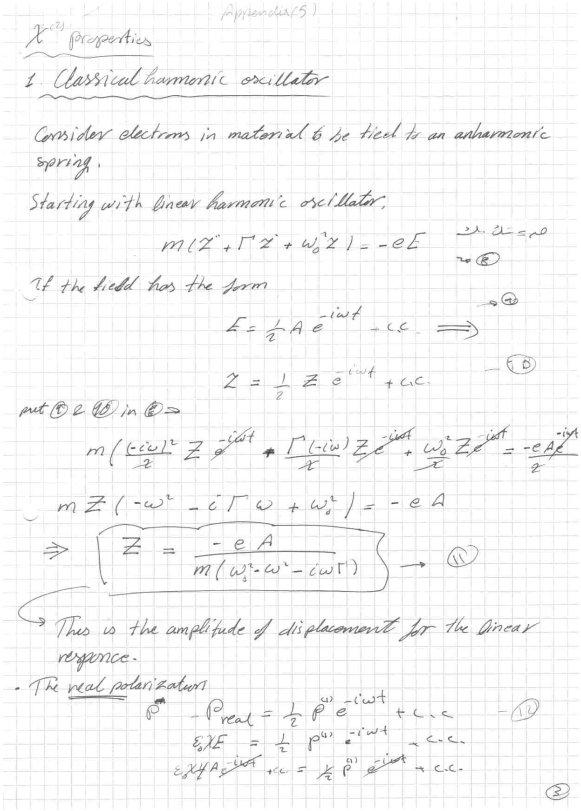

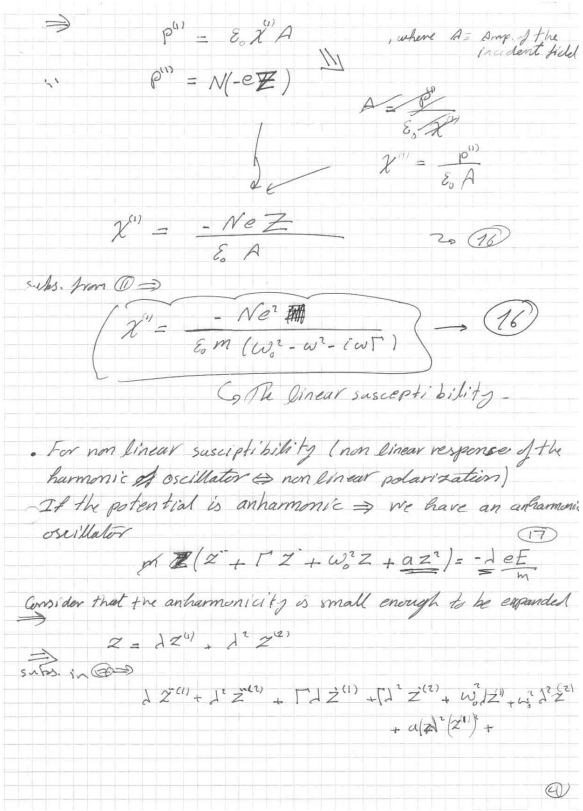

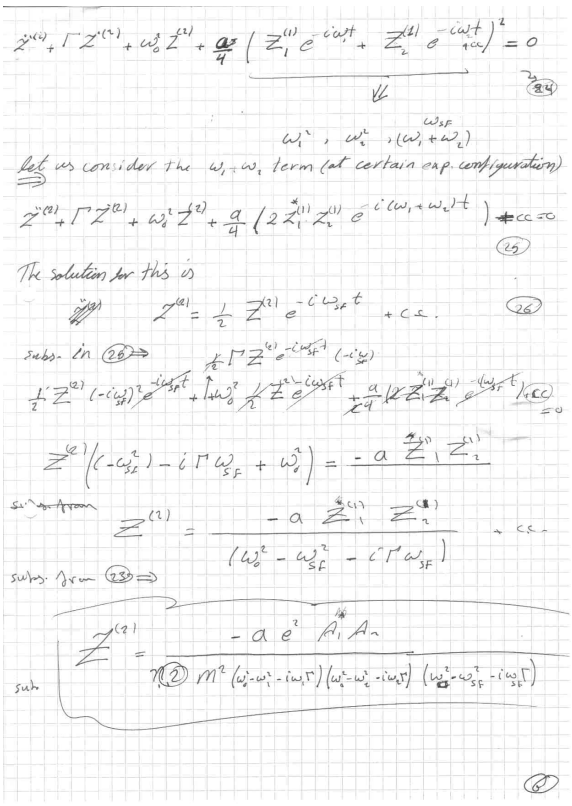

Appendix

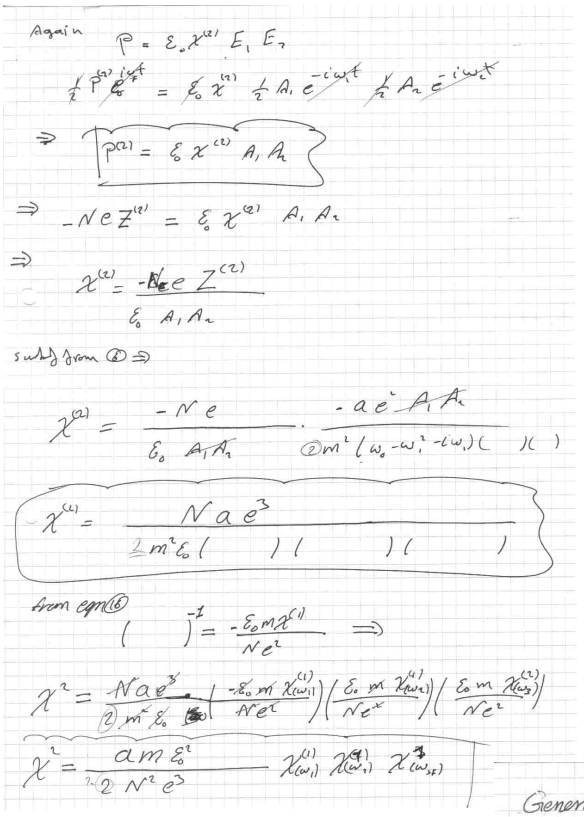

Generalizing eqn 1 to account for tensor nature of the material:

$$\chi^{(2)}_{ijk}(\omega_1, \omega_2, \omega_3) = \chi^{(1)}_{ii} \chi^{(1)}_{jj} \chi^{(1)}_{kk} D_{ijk}$$

① Miller's rule

Miller's delta = const. for non-organic materials

$\Rightarrow$ The higher the χ the higher the nonlinearity

$\Leftrightarrow$ ~ ~ ~ Refr. index ~ ~ ~ ~ .

Appendix 6

Abbreviations

Abb.	*Explanation*
SHG	*Second Harmonic Generation*
SFG	*Sum Frequency Generation*
DFG	*Difference Frequency Generation*
XPS	*X-ray Photoelectron Spectroscopy*
cc or c.c.	*Complex conjugate*
TIR	*Total Internal Reflection*
ATR	*Attenuated Total internal Reflection*
Vis.	*Visible*
IR	*Infrared*
//	*Parallel*
⊥	*Perpendicular*
n	*Refractive index*
$\hat{n}$	*Complex refractive index*
3D	*Three Dimension*
FF	*Fresnel Factors*
GF	*Geometry Factors*
P-pol.	*P-polarized light: A Light which has it's Electric filed oscillating parallel (Parallel in German) to the plane of incident*
S-pol.	*S-polarized light: A Light which has it's Electric filed oscillating Perpendicular (Senkrecht in German) to the plane of incident*
PPP	*A spectrum of polarization combination with P-SFG, P-Incident visible beam and P-incident IR beam. The same for SSP, SPP, PSP …etc*
I(SF/IR/Vis)	*The detected signal normalized to the incident beams in terms of Intensity units*
E(SF/IR/Vis)	*The detected signal normalized to the incident beams in terms of Field units*
SS	*Symmetric Stretch vibration*
AS	*Asymmetric Stretch vibration*
+ve peak	*This peak has a net dipole moment pointing out from the surface*
-ve peak	*This peak has a net dipole moment pointing into the surface*
AU	*Arbitrary Unit*
CAMI	*Contact Angle Measurement Instrument*
SCC	*Standard Calibration Cross*
INE	*Institut für Nukleare Entsorgung (INE)* *Institute of Nuclear wastes Disposal*
FZK	*Forschungszentrum Karlsruhe Deutschland (FZK)* *Karlsruhe research Center- Germany*

Appendix 7

Related links

	Link	Description
a	www.amamonem.de , www.amamonem.com	Ahmed Abdelmonem website
b	http://www.amamonem.com/aboutme.htm	Ahmed Abdelmonem CV .pdf Visual CV .PPS List of Publications
c	http://www.fzk.de/fzk/idcplg?IdcService=FZK&node=0048	Institut für Nukleare Entsorgung (INE) Institute of Nuclear wastes Disposal
d	http://www.fzk.de	Forschungszentrum Karlsruhe Deutschland (FZK) Karlsruhe research Center- Germany
e	http://www.amamonem.com/research.htm	SFG in TIR Geometry Inversion point in Butanol-water/sapphire spectra
f	http://hyperphysics.phy-astr.gsu.edu/hbase/hframe.html	HyperPhysics HyperPhysics is an exploration environment for concepts in physics which employs concept maps and other linking strategies to facilitate smooth navigation.
g	http://digitaldutch.com/unitconverter/	Unit Converter The WWW Unit Converter - Online conversion of area, density, energy, force, length, mass, power, pressure, speed, temperature, volume and bytes.
h	http://www.cem.msu.edu/~reusch/VirtualText/Spectrpy/InfraRed/infrared.htm	Infrared Spectroscopy Bases for Infrared Spectroscopy
i	http://www.chemguide.co.uk/index.html#top	chemguide Helping you to understand Chemistry
j	http://www.gnuplot.info/	Gnuplot homepage Gnuplot is a portable command-line driven interactive data and function plotting utility for UNIX, IBM OS/2, MS Windows, DOS, Macintosh, VMS, Atari and many other platforms.

Appendix 8 †

Symmetry constraints on optical properties of minerals			
System	***Classification***	***Defining R.I.'s***	***Shape and Orientation***
Cubic	Isotropic	n	Sphere
Tetragonal	Uniaxial	ω and ε	Ellipsoid of Revolution ε parallel to z
Hexagonal	Uniaxial	ω and ε	Ellipsoid of Revolution ε parallel to z
Trigonal	Uniaxial	ω and ε	Ellipsoid of Revolution ε parallel to z
Orthorhombic	Biaxial	α, β, and γ	General Ellipsoid α, β, and γ parallel to x, y, and z (in any order!)
Monoclinic	Biaxial	α, β, and γ	General Ellipsoid Either α, β, or γ parallel to y
Triclinic	Biaxial	α, β, and γ	General Ellipsoid No orientation constraints

† *Richard Harrison: Optics Theory Handou*

Appendix 9

(a) Principles of Contact Angle

Geometrically, contact angle is defined as the angle formed by a liquid at the three phase boundary where a liquid (L), vapor (V) and solid (S) intersect. It is a quantitative measure of the wetting of a solid by a liquid (hydrophilicity / hydrophobicity), surface tension, adhesion, cleanliness, and biocompatibility. The shape of a liquid droplet on a flat horizontal sold surface is determined by the *Young-Laplace equation*:

$$\begin{aligned}\Delta p &= \gamma \nabla . \hat{n} \\ &= 2\gamma H \\ &= \gamma\left(\frac{1}{R_1}+\frac{1}{R_2}\right)\end{aligned}$$

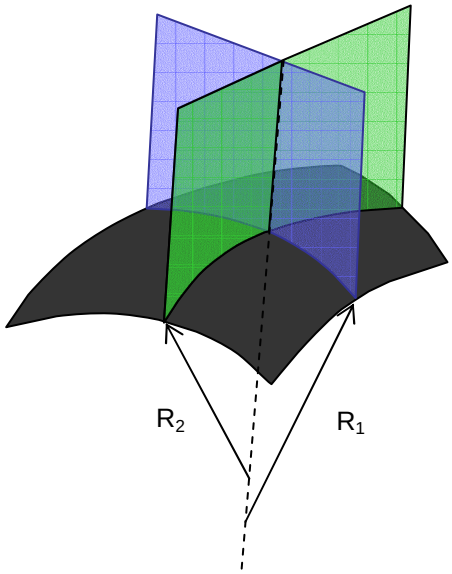

where

Δp : The pressure difference across the interface

γ : The surface tension.

$\hat{n}$: The unit vector normal to the surface.

H : The mean curvature.

R_1, R_2 : The radii of curvature of the two principle curvatures.

N.B.

In our case, we consider the drop as a part of a sphere, hence $R_1 = R_2$.

At thermodynamic equilibrium between the three phases (L, V and S), the chemical potential in the three phases should be equal. The interfacial energies can be related to the contact angle through either,

1. *Young Equation*:

$$\gamma_{SV} - \gamma_{SL} - \gamma_{LV}\cos\theta_c = 0$$

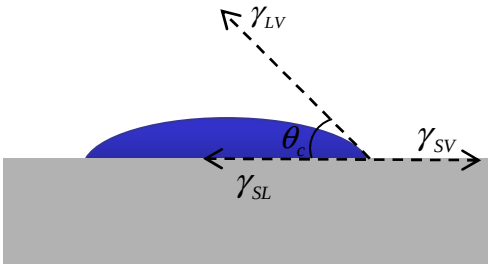

where;

γ_{SV} : The solid-vapor interfacial energy.

γ_{SL} : The solid-liquid interfacial energy.

γ_{LV} : The liquid-vapor energy (the surface tension)

θ_c : The experimentally measured contact angle.

or

2. *Young-Dupré equation*:

$$\gamma_{LV}(1+\cos\theta_c) = \Delta W_{SLV}$$

where,

ΔW_{SLV} is the adhesion energy per unit area between the solid and liquid surfaces when in the vapor medium.

(b) Information to be extracted from contact angle [‡]

Contact angle is rich of information depending on the given parameters of the sample under study.

Useful Formulas

Young's Equation
Contact angle of liquid on surface
Also, the force balance on a spherical sessile drop

$\gamma_{SV} - \gamma_{SL} = \gamma_{LV} \cos\theta$

γ_{SV} = solid vapor IFT (aka *surface energy* of solid)
γ_{SL} = solid liquid IFT (IFT = interfacial tension)
γ_{LV} = liquid vapor IFT (aka *surface tension* of liquid)
θ = contact angle of drop (angle in liquid at three-phase line)

Laplace Pressure across Curved Surface

$\Delta P = \gamma_{LV} (1/R_1 + 1/R_2)$

$\Delta P = \perp$ pressure differential across interface
R_1, R_2 = principal radii of curvature of interface at $\perp$ point
for sphere, $R_1 = R_2$ = radius of sphere

Spherical Drop Geometry

$\theta = 2 \arctan (2h / d)$

h = height of drop
d = diameter of drop's wetted surface on solid
θ = contact angle of drop

Laplace-Young Equation
IFT of liquid-vapor (γ_{LV}) or liquid-liquid (γ_{LL}) interface

$mgh = \Delta P = \gamma_{LV} (1/R_1 + 1/R_2)$

m = density differential across interface
g = acceleration of gravity
h = vertical position with drop, measured from apex

Force on Wilhelmy Plate

$F = L \gamma_{LV} \cos\theta$

F = force on plate
L = wetted perimeter length

Force - Mass (Weight) Relationship

$F = mg$

F = force (in Newtons) measured by balance
m = mass (in kilograms)
g = acceleration of gravity, nominally 9.8m/s^2
e.g. 1 gram mass → 9.8 milli Newton force

Basic Statistics

$\mu = \Sigma x_i / n$
$\sigma = \sqrt{\{ 1/(n-1) \Sigma(x_i - \mu)^2 \}}$
$COV = \sigma / \mu$

n = number of items
i = index of item (for summations)
x_i = value of i^{th} item
μ = mean value (aka *average*) of set
σ = standard deviation of set
COV = coefficient of variance

Hook's Law and Dilational Stress

$\tau = G \gamma$
$\tau(t) = G(t) \gamma(t)$
$G' = \tau_0 \cos(\phi) / \gamma_0$
$G'' = \tau_0 \sin(\phi) / \gamma_0$
$\eta' = G'' / \omega$
$\eta'' = G' / \omega$

τ = stress, or force per unit area
$\tau(t)$ = time varying stress, typically $\tau_0 \sin(\omega t)$
G, G(t) = elastic modulus
γ = strain, relative change in length (or shape)
$\gamma(t)$ = time varying strain, typically $\gamma_0 \sin(\omega t + \phi)$
G' = in-phase *elastic* modulus
G'' = out-of-phase *viscous* modulus
η' = dynamic viscosity
η'' = dynamic elasticity

Wetting Tension
Characterizes solid surface by RHS of Young's equation:

$WT = \gamma_{LV} \cos\theta$

Note this varies from $-\gamma_{LV}$ (at 180°) to $+\gamma_{LV}$ (at 0°)

Zisman's Critical Wetting Tension

Critical Wetting Tension (CWT) is defined as intersection of IFT-cos θ plot line with cos 0° (IFT on X axis, cos θ on Y). IFT at this point is CWT. Experimentally it is found CWT ≈ γ_{SV}.

Girifalco-Good-Fowkes-Young Rule
Uses the combining rule $\gamma_{SL} = (\sqrt{\gamma_{SV}} - \sqrt{\gamma_{LV}})^2$
$1 + \cos\theta = 2 \sqrt{(\gamma_{SV} / \gamma_{LV})} - \pi / \gamma_{LV}$
π = spreading pressure (often ≈ 0)

Owens-Wendt Geometric Mean Mean

$(1 + \cos\theta) \gamma_{LV} = 2 \sqrt{(\gamma^D_{SV} \gamma^D_{LV})} + 2 \sqrt{(\gamma^P_{SV} \gamma^P_{LV})}$

D superscript indicates dispersive and P polar component

Wu's Harmonic Mean Rule

$(1 + \cos\theta) \gamma_{LV} = 4\{\gamma^D_{SV}\gamma^D_{LV} / (\gamma^D_{SV}+\gamma^D_{LV}) + \gamma^P_{SV}\gamma^P_{LV} / (\gamma^P_{SV}+\gamma^P_{LV})\}$

Lewis Acid / Base Rule

$(1 + \cos\theta) \gamma_{LV} = 2\sqrt{(\gamma^D_{SV} \gamma^D_{LV})} + 2\sqrt{(\gamma^A_{SV} \gamma^B_{LV})} + 2\sqrt{(\gamma^B_{SV} \gamma^A_{LV})}$

A superscript indicates acid and B base component

[‡] www.firsttenangstroms.com

ACKNOWLEDGMENTS

First of all, I would like to thank the German scientific community for providing those bountiful opportunities and the wide range facilities to young researchers.

My full thanks to the members of the institutes, where I did my Ph.D. work:

Scientific and official supervision

Dr. M. Himmelhaus[*], Dr. H. Geckeis[†], Dr. H. Volpp[*]

Dr. J Lützenkirchen[†] and Dr. R. Klenze[†]

Scientific, official, technical and equipment support

Dr. Klaus Kruse[†], Dr. R. Dahint[*], Dr. Mohamed E. Ibrahim[‡], Dr. Muriel Bouby[†], Mrs. Jana Wehrmeister[*], Dr. Klaus Gompper[†], Dr. Dieter Schild[†], Dr. Wolfgang Hauser[†], Dr. Robert Polly[†], Mr Sebastian Büchner[†], Machinery-shop members[†]

A special thank for my wife (**Inas Ibrahim**, B.Sc., Laser-Dip.[§]) for the continuous scientific and morale support.

[*] University of Heidelberg - Germany
[†] Institute of Nuclear wastes Disposal (INE)- KFZ - Germany
[‡] Higher Technological Institute, (HTI)- Egypt
[§] National Institute of Laser Enhanced Since – University of Cairo Egypt

Ich erkläre hiermit, dass ich die vorgelegte Dissertation selbst verfasst und mich keiner anderen als der von mir ausdrücklich bezeichneten Quellen und Hilfen bedient habe. Ich erkläre hiermit, dass ich an keiner anderen Stelle ein Prüfungsverfahren beantragt bzw. die Dissertation in dieser oder anderer Form bereits anderweitig als Prüfungsarbeit verwendet oder einer anderen Fakultät als Dissertation vorgelegt habe.

I herewith declare that the presented Ph.D. thesis was written by me and that I have used no other sources and aids except those mentioned in the text. I herewith declare that I have neither requested an examination nor submitted the manuscript in this or other form as a document for obtaining a Ph.D. at another faculty.

Ahmed Abdelmonem, May 2008